University of Huddersfield Repository

Nair, Greeshma

Atomistic Simulation Studies of WO3 stabilized tetragonal Zirconia

Original Citation

Nair, Greeshma (2013) Atomistic Simulation Studies of WO3 stabilized tetragonal Zirconia. Doctoral thesis, University of Huddersfield.

This version is available at http://eprints.hud.ac.uk/id/eprint/18125/

The University Repository is a digital collection of the research output of the University, available on Open Access. Copyright and Moral Rights for the items on this site are retained by the individual author and/or other copyright owners. Users may access full items free of charge; copies of full text items generally can be reproduced, displayed or performed and given to third parties in any format or medium for personal research or study, educational or not-for-profit purposes without prior permission or charge, provided:

- The authors, title and full bibliographic details is credited in any copy;
- A hyperlink and/or URL is included for the original metadata page; and
- The content is not changed in any way.

For more information, including our policy and submission procedure, please contact the Repository Team at: E.mailbox@hud.ac.uk.

http://eprints.hud.ac.uk/

Atomistic Simulation Studies of WO_3 stabilized tetragonal Zirconia

by

Greeshma Nair

A thesis submitted to the University of Huddersfield in partial fulfillment of the requirements for the degree of Doctor of Philosophy.

University of Huddersfield

May 2013

Dedicated in loving memory of my Father

Abstract

Tungstated Zirconia (WO_3-ZrO_2) is a technologically important catalyst; however, there is still a considerable lack of understanding for the presence of different WO_3 surface species found in this catalyst which are responsible for its high activity. We report here the application of atomistic simulation techniques based on interatomic potentials to explore the nature of WO_3 species on WO_3-ZrO_2 systems. At first modelling of the pure structure of t-ZrO_2 was investigated and the reliability of computed structures was found to agree with earlier theoretical and experimental studies. An investigation of all low miller index pure surfaces of t-ZrO_2 revealed the highest stability in the following order {101} > {001} > {111} > {110} > {100}. The adsorption of WO_3 at partial monolayer coverages of 20 % and 50 % were then investigated onto the surfaces of t-ZrO_2.

Conclusions that can be drawn from this work are that the preference WO_3 species for a particular surface depended on the type of the surface and temperature considered. The highest favourability to WO_3 addition was detected on the {111} surface, where a 50 % monolayer coverage was found to be stable. The {100} and {110} surfaces were favourable to WO_3 addition, although this favourability depended on the temperature and amounts of WO_3 added. The surfaces {001} and {101} were not favourable to WO_3 addition at low temperatures. The addition of WO_3 resulted in stabilizing of surfaces which were otherwise unstable in t-ZrO_2 such as the {111}, {110} and {100}. The study also confirms the formation of polymerized WO_3 layers, dimers, monomers and Zr-WO_3 linkages which were detected in earlier experiments. The nature of WO_3 species were found to be surface specific, which also depended on the surface area and temperature. The knowledge obtained from this study could be used to design and optimize an efficient catalyst.

List of Abbreviations

METADISE: Minimum Energy Technique Applied to dislocation Interface and Surface Energies**.**

GULP: General Utility Lattice Program

MD: Molecular dynamics

BFGS: Broyden, Fletcher, Golfarb and Shannon algorithm

CG: Conjugate Gradients

NN: Nearest Neighbour

NNN: Next Nearest Neighbour

CN: Coordination Number

DOS: Density of States

HRTEM: High Resolution Transition Electron Microscopy

XRD: X-ray Diffraction

RDF: Radial Distribution Function

Acknowledgements

First and foremost, I humbly thank the Almighty God for giving me the strength and wisdom to reach this important milestone in my academic life. I owe countless thanks to my supervisor Dr. David Cooke, who introduced me to the world of Computational Chemistry. Without his support and extremely good guidance, I would not be able to achieve this. I deeply appreciate his great patience in clarifying my doubts. I am also extremely grateful to Prof. Rob Brown for the great support that he provided at every stage for the continuation of my fellowship. I am thankful to Dr. Pooja Panchmatia for giving me valuable comments on my work, which improved my thesis. I also thank Prof. Steve Parker (University of Bath) for his scientific support in my research work. I would like to record my gratitude to the University of Huddersfield for the special fee-waiver fellowship provided to me. I am thankful to Prof. Rob Jackson from the University of Keele and Dr. Pooja Panchmatia to positively evaluate my thesis during the viva. Acknowledgements to the computer power provided by the University of Huddersfield and also to the people who work efficiently for its maintenance. Great thanks go to all the forerunners in this area of research.

I would like to sincerely thank my husband Dr. N. R. Shiju from the bottom of my heart for providing me support at every stage of this work. He is my best friend and my gratitude to him is beyond words. My special thanks go to my lovely mother, who is a constant source of inspiration for me. I am indebted to her for her constant prayers which enabled me to reach till present. I must also mention my little girl Neha, who depicted a great level of understanding during my thesis writing. I also sincerely thank my brother, who is the one to have kindled the spirit of research into my mind at the very early ages of my life. The greatest inspiration in my life is my Father and I dedicate all my accomplishments to him. He was a man of impeccable character and honesty and provided me with unconditional love and support and stood by me through the good and bad times of life. I am forever indebted to him. I also thank all my well-wishers and friends.

List of Figures and Tables

Figures

Tables

List of Contents

Chapter 6 Defect chemistry of t-ZrO_2 on Bulk and Surfaces……… 130

Chapter 7 Tungstated Zirconia……………..…………..………………….. 156

Chapter 1 Introduction

"To myself I am only a child playing on the beach, while vast oceans of truth lie undiscovered before me."

— Sir Isaac Newton

1.1 Introduction

Over the last decades computational modelling techniques have extensively benefited our understanding of the chemistry of materials. Such techniques are well established in virtually all areas of mainstream material science, including polymers, ceramics, semiconductors and metals. [1-5] They are also a major driving force in relatively new avenues of research, such as pharmaceutical materials science, nanotechnology, engineering bio-mimetic materials and solid-state ionics. [6-9] Computer simulation can be used as a powerful predictive tool to guide novel experimental programmes in a fraction of the time and cost of trial-and-error approaches. [10, 11] Furthermore, with the increasing use of three-dimensional imaging techniques such as X-ray micro- or nanotomography (and similar electron or ion beam based methods), it is now possible to undertake microstructural materials modelling in which multiscale structural information can be used directly for property prediction. [12-17] These techniques treat a system at three levels of physical description Quantum mechanics (QM), Molecular mechanics (MM) and Mesoscopic Soft Matter, where the level of detail considered successively decreases while allowing the system length and time-scales to be increased. Figure 1.1 shows the hierarchy of multiscale modelling techniques and the areas of overlap permit 'mapping'

rom one scale to the next, which is often required for parameterisation of higher scale methods to obtaining a finer scale resolution. [18]

Computer modelling techniques are now well established tools in the field of solid state materials and have been applied successfully to the study of crystal structures and dynamics in solids at the atomic level. [19] The present study addresses the application of these modelling techniques to metal oxide materials. Metal oxides in general are important materials with wide application in several areas of chemistry and chemical engineering, some of the major applications include catalysis (as a catalyst support, promoter), in solid oxide fuel cells and oxygen sensors. [20-24] The defects in their structures play an important role in their properties. Zirconia is the material under investigation in this thesis. Zirconia exhibits three different types of crystal structures with the increase in temperatures. Each of this material varies greatly in terms of their properties. Hence, a great deal of structural investigation is required to explore its potential for various applications. [25-28] Recently WO_3 doped zirconia has been a topic of investigation for several catalytic reactions such as isomerisation, esterification etc., but any information of its structural variations on doping with tungsten is rarely discussed. It is therefore very important to understand these variations in order to explore the application in several areas of chemical sciences.

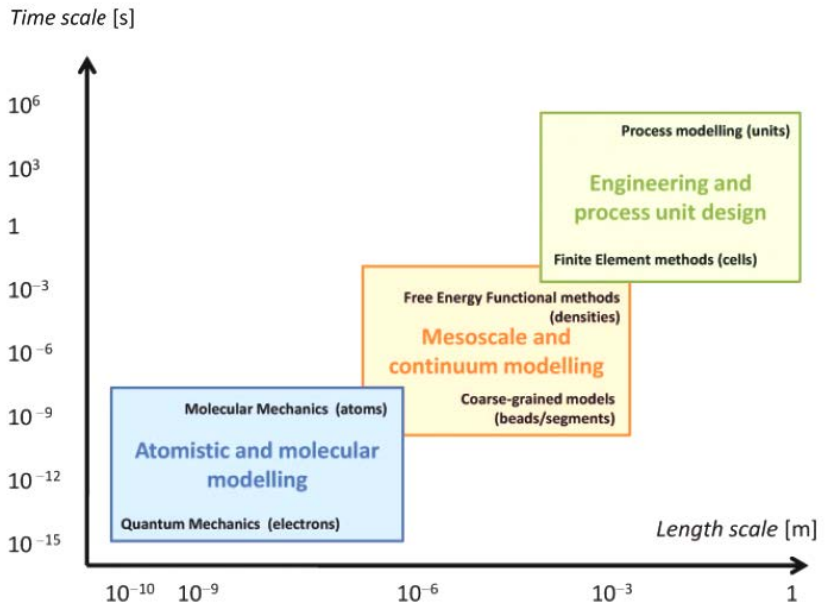

Figure-1.1 The hierarchy of multiscale modelling techniques, showing approximate range of temporal and spatial scales covered by different categories of methods. (taken from Reference [18])

1.2 The Big Mystery and why the need of Simulation?

Gasoline is considered to be one of the most vital fluids in the economy of the world. From the early 1920s lead has been blended with gasoline to boost its octane levels. Leaded gasoline causes severe harmful effects on human health and the only way to avoid this was introducing aromatic compounds into the fuel in place of lead. The aromatic compounds used however are carcinogenic in nature. The requirement for gasolines without harmful lead and aromatic compounds resulted in a search for new

catalysts. [29] Any new catalyst should be capable of producing high octane number compounds by isomerisation of widely available straight chain alkanes in an environmentally friendly way. The isomerisation of alkanes gives branched high octane number isopentanes, isohexanes and isobutanes, which are good gasoline components. In the early 1990s, the capacities of these isomerisations were estimated to be more than 1 million barrels per day. The kinetics and mechanism of the isomerisation depends on the type of catalyst used and the reaction conditions.

The research carried out so far shows that the isomerisation occurring under heterogeneous catalysis conditions takes place via a thermodynamically –controlled mechanism.[30] The efficiency of their catalytic action to isomerise alkanes is usually evaluated by the rate of their transformation into the corresponding isomer or mixture of isomers. Studying the various steps of the process as well as the intermediate products, which are inevitably formed, can assess the mechanism of isomerisation of various hydrocarbons. It has been established that the mechanism of isomerisation in the presence of bifunctional catalysts depends on the degree of acidity of the catalyst support. In the case of strongly acidic supports, the process is concentrated on the catalyst acid centres. In this case, the metal of the catalyst limits the coke formation and prevents the deactivation of the corresponding acid centres. [31] For catalysts, which have a very low acidity, the isomerisation takes place predominantly on the metal centres and the mechanism of the reaction depends on the size of the metal crystallites.[32] In the case of using a catalyst support of moderate acidity, the isomerisation proceeds via the so-called bi-functional mechanism, which involves both an acid and a base site.

The most widely applied alkane isomerisation catalysts are platinum-promoted solid acids, chlorinated alumina, zeolites and mordenite. [33-35] The chlorinated catalyst are highly active and operate at low temperatures (400–450 K), so formation of the desired branched alkanes is favored thermodynamically. These catalysts, however, require the constant addition of chlorine-containing compounds and are sensitive to moisture and sulfur impurities. [36] They are also highly corrosive and subject to stringent environmental regulations. The use of zeolite catalysts do not suffer from these disadvantages, but they are significantly less active, operating at higher temperatures (500–550 K) and characterized by low yields of branched alkanes as a consequence of the thermodynamic limitations.

This has led to the demand for more environment friendly active catalyst that can operate at low temperatures. The extensive work by Holm and Bailey resulted in the development of sulphated zirconia (SZ) catalyst. SZ is a potential solid acid catalyst that can catalyse the isomerisation of alkanes at 300 – 420 K. [37-40] The properties of this catalyst were further improved by the addition of modifiers like iron and manganese, which imparted more stability and selectivity to the catalyst.[41, 42] Although the SZ catalyst found a lot of commercial applications, these catalysts were known to suffer from the loss of sulfate groups during the calcination, regeneration or reduction processes.[43] To solve this problem Hino and Arata [38, 48] in 1988 proposed tungstated zirconia (WO_3-ZrO_2) as an alternative to SZ catalyst. Although the activity of WO_3-ZrO_2 catalyst was less than the

SZ catalyst, this catalyst possessed superior stability under both oxidizing and reducing condition, making them more suitable for industrial applications. The catalytic activity of the WO_3-ZrO_2 catalyst was later improved by the addition of platinum. The Pt/WO_3-ZrO_2 catalyst was found to be more selective than Pt/SZ catalysts for the formation of branched alkanes in the conversion of n-heptane and n-octane. [44-47]

It was suggested by Hino and Arata [48] that the formation of so-called "superacid" sites makes these materials active catalysts for isomerization of butane and pentane. [49, 50] Since the discovery of the ability of tungstated zirconia to catalyze alkane isomerization at low temperatures, there were several reports of the use of these materials for other reactions such as isomerization, esterification, transesterification, cyclohexane ring-opening, benzene hydrogenation, alkene oligomerization, aromatic alkylation with alkenes or methanol, aromatic transalkylation, and heteroatom removal. [51-68] The identification of catalytically active sites in several chemical reactions can provide an insight into the mechanism but at times can be like a murder mystery. [69] As there could be many suspects, but many of the probable suspects could be mere spectators while the actual culprit is hidden and hard to detect. It is very important to use characterisation tools like high resolution SEM/TEM or Molecular modelling techniques to identify the role of various species which could expose the naked truth of this science. These toolboxes will enable us to catch these species and expose their behaviours under various stressful events.

As a part of their investigation earlier Christopher Kiely and colleagues [69] used high resolution STEM images which revealed the presence of monotungstate and polytungstate species of WO_x as well as some distorted Z-WO_x clusters within the zirconia frame work see Figure 1.2. So far no detailed study using computational techniques has been employed to look at the behaviour of such complex systems. The aim of this study is to explore the presence of such species and compare the effects of temperature and their influence under various circumstances.

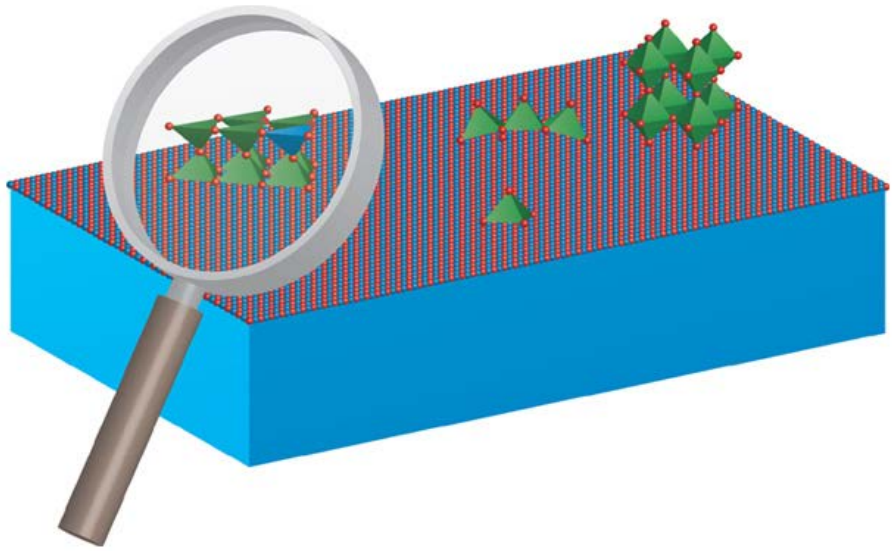

Figure 1.2 The four different suspected surface species in supported WO_x/ZrO_2 catalyst active in light alkane isomerization: monotungstate, polytungstate, well-ordered WO_3 nanocrystals and WO_3 distorted clusters.(taken from Reference [68]).

1.3 Opportunities for Computational Modelling

Tungstated Zirconia (WO_3-ZrO_2) is one of the most important industrial catalysts used for several important reactions. There are still several areas of incomplete understanding which cannot be easily investigated by experiment so presenting a considerable opportunity for computational modelling, in particular. Modelling would be capable to provide a more precise picture of the bulk structures and the factors affecting stability across the temperature range, which are complex owing to the polymorphic nature of ZrO_2 and the complicated phase transition processes. Catalysis is a surface process, and hence modelling can help us better to understand the topography and chemistry of the surface and the preference of adsorbents to any particular surface. In relation to the isomerization of alkanes, modelling can also identify the nature of the active sites and in particular, study the adsorption mechanism of WO_3 on to the various surfaces of tetragonal zirconia. The studies presented in this thesis are dedicated to provide further understanding of these issues.

1.4 References

[1] C. R. A. Catlow, *Annu. Rev. Mater. Sci*, 16 (1986) 517.
[2] Y. M. Liu, R. B. Pandey, *Phys. Rev. E.*,54 (1996) 6609.
[3] J. Hefter, R. W. Zuehlke, *J. Chem. Educ*., 54 (1977) 63.
[4] P. E. J. Flewitt, *Mater. Sci. Eng. A*, 365 (2004) 257.
[5] R. S. Hoy, N. C. Karayiannis, *Phys. Rev. E.,* 88 (2013) 12601.
[6] J. A. Elliott, B. C. Hancock, *Mater. Res. Soc. Bull*., 31 (2006) 869.
[7] W. K. Liu, E. G. Karpov, S. Zhang, H. S. Park, *Comput. Methods Appl. Mech. Eng*., 193 (2004) 1529.
[8] A. M. Stoneham, *Mater. Sci. Eng. C*, C23 (2003) 235.
[9] S. Kim, S. Yamaguchi, J. A. Elliott, *Mater. Res. Soc. Bull*., 34 (2009) 900.
[10] W. F. van Gunsteren, H. J. C. Berendsen, *Angew. Chem. Int. Ed*. 29 (1990) 992.
[11] A. M. Stoneham, *Phil. Trans. R. Soc*. Lond. Math. Phys. Sci., 360 (2002) 1107.
[12] B. C. Larson, W. Yang, G. E. Ice, J. D. Budai, J. Z. Tischler, *Nature*, 415 (2002) 887.
[13] X. W. Fu, M. Dutt, A. C. Bentham, B. C. Hancock, R. E. Cameron, J. A. Elliott, *Powder Technol*., 167 (2006) 134.
[14] J. Y. Buffiere, P. Cloetens, W. Ludwig, E. Maire and L. Salvo, *Mater. Res. Soc. Bull*., 33 (2008) 611.
[15] G. Tabor, O. Yeo, P. Young, P. Laity, *Int. J. Mod. Phys. C*, 19 C (2008) 703.
[16] S. A. McDonald, G. Dedreuil-Monet, Y. T. Yao, A. Alderson, P. J. Withers, *Phys. Status Solidi (b)*, 248 (2011) 45.
[17] A. Lyubartsev, Y. Tu, A. Laaksonen, *J. Comput. Theor. Nanos*, 6 (2009) 1.
[18] J. A. Elliott, *Int. Mat. Rev*, 56 (2011) 207.
[19] M. S. Islam, P. R. Slater, *MRS Bull*., 34 (2009) 935.
[20] C. Noguera, *Physics and Chemistry at Oxide Surfaces*; Cambridge University Press: Cambridge, UK, (1996).
[21] H. H. Kung, *Transition Metal Oxides: Surface Chemistry and Catalysis*; Elsevier: Amsterdam, (1989).
[22] V. E. Henrich, P. A. Cox, *The Surface Chemistry of Metal Oxides*; Cambridge University Press: Cambridge, UK, (1994).
[23] A. F. Wells, *Structural Inorganic Chemistry*, 6th ed.; Oxford University Press: New York, (1987).
[24] W. A. Harrison, *Electronic Structure and the Properties of Solids*; Dover: New York, (1989).
[25] R. Nielsen, *Encyclopedia of Industrial Chemistry*, 2005, Wiley-VCH, Weinheim.
[26] N. N. Greenwood, A. Earnshaw, Chemistry of the Elements (2nd Edn.), Oxford: Butterworth-Heinemann, (1997).
[27] A. G. Evans, R. M. Cannon, *Acta Mat*. 34 (1986) 761

[28] A. H. Heuer, L. W. Hobbs, *Science and Technology of Zirconia, Adv. Ceram*., 3 (1981) 475.
[29] S. Kuba, P. Lukinskas, R. K. Grasselli, B. C. Gates, H. Knözinger, *J. Catal*., 216 (2003) 353.
[30] A. Petrov, *Alkane Chemistry, Science*, Moscow (1994) 256.
[31] H. R. Bursian, VNII Neftekhim, (1996) 27.
[32] J. Ketzer, B. Gates, *Chemistry of Catalytic Processes*, Mir Moscow, (2001) 374.
[33] D. H. Belden, *Petrol. Refiner*., 35 (1956) 149.
[34] H. W. Kouwenhoven, W.C. van Zijll Langhout, *Chem. Eng. Progr*. 67 (1971) 65
[35] J. G. Santiesteban, D. C. Calabro, C. D. Chang, J. C. Vartuli, T. J. Fiebig, R. D. Bastian, *J. Catal*., 202 (2001) 25.
[36] S. T. Sie, G. Ertl, H. Knözinger, J. Weitkamp (Eds.), *Handbook of Heterogeneous Catalysis*, Vol. 4, Wiley–VCH, Weinheim, (1997).
[37] V. C. F. Holm, G. C. Bailey, US Patent 3,032,599, (1962).
[38] M. Hino, K. Arata, *J. Chem. Soc. Chem. Commun*. (1980) 851.
[39] T. Yamaguchi, K. Tanabe, *J. Phys. Chem*. 90, (1986) 4794.
[40] C. Y. Hsu, C. R. Heimbuch, C. T. Armes, B. C. Gates, *J. Chem. Soc. Chem. Commun*. (1992) 1645.
[41] V. Adeeva, J. W. de Haan, J. Jänchen, G. D. Lei, V. Schünemann, L. J. M. van de Yen, W. M. H. Sachtler, R. A. van Santen, *J. Catal*. 151, (1995) 364.
[42] C. Gosling, R. Rosin, P. Bullen, *Petrol. Technol. Q*. 55 (1997).
[43] J. C. Yori, C. R. Vera, J. M. Parera, *Appl. Catal*. A, 163 (1997) 165.
[44] J. M. Grau, J. C. Yori, J. M. Parera, *Appl. Catal*., A 213 (2001) 247.
[45] S. L. Soled, W. E. Gates, E. Iglesia, US Patent 5,422, (1995) 327.
[46] E. Iglesia, D. G. Barton, S. L. Soled, S. Miseo, J. E. Baumgartner, W. E. Gates, G. A. Fuentes, G. D. Meitzner, *Stud. Surf. Sci. Catal*. 101 (1996) 533.
[47] C. D. Chang, S. Han, R. A. Morrison, J. G. Santiesteban, US Patent 5,992,643, (1993)
[48] M. Hino, K. Arata, *J. Chem. Soc., Chem. Commun*. (1988) 1259.
[49] D. G. Barton, M. Shtein, R. D. Wilson, S. L. Soled, E. Iglesia, *J. Phys. Chem. B*. 103 (1999) 630.
[50] N. Soultanidis, W. Zhou, A. C. Psarras, A. J. Gonzalez, E. F. Iliopoulou, C. J. Kiely, I. E. Wachs, M. S. Wong, *J. Am. Chem*., 132 (2010) 13462.
[51] D. G. Barton, S. L. Soled, G. D. Meitzner, G. A. Fuentes, E. Iglesia, *J. Catal.* 181 (1999) 57.
[52] E. I. Ross-Medgaarden, W. V. Knowles, T. Kim, M. S. Wong, W. Zhou, C. J. Kiely, I. E. Wachs, *J. Catal*., 256 (2008) 108.
[53] D. E. Lo´pez, J. G. Goodwin, D. A. Bruce, S. Furuta, *Appl. Catal., A*, 339 (2008) 76.
[54] A. Martı´nez, G. Prieto, M. A. Arribas, P. Concepcio´n, J. F. Sa´nchez-Royo, *J. Catal*., 248 (2007) 288.
[55] D. E. Lo´pez, K. Suwannakarn, D. A. Bruce, D. J. G. Goodwin, *J. Catal*., 247 (2007) 43.
[56] M. A. Corte´s-Ja´come, C. Angeles-Chavez, E. Lo´pez-Salinas, J. Navarrete, P. Toribio, J. A. Toledo, *Appl. Catal*., 318 (2007) 178.
[57] R. L. Martins, M. Schmal, *Appl. Catal., A*, 308 (2006) 143.

[58] A. Martı´nez, G. Prieto, M. A. Arribas, P. Concepcio´n, *Appl. Catal., A*, 309 (2006) 224.
[59] S. T. Wong, T. Li, S. Cheng, J. F. Lee, C. Y. Mou, *Appl. Catal., A*, 296 (2005) 90.
[60] R. Sakthivel, H. Prescott, E. Kemnitz, *J. Mol. Catal. A*., 223 (2004) 137.
[61] S. Kuba, P. Lukinskas, R. K. Grasselli, B. C. Gates, H. Kno¨zinger, *J. Catal*. , 216 (2003) 353.
[62] K. Shimizu, T. N. Venkatraman, W. Song, *Appl. Catal*., A, 225 (2002) 33.
[63] S. V. Filimonova, A. V. Nosov, M. Scheithauer, H. Kno¨zinger, *J. Catal*., 198 (2001) 89.
[64] Y. –H. Chin, W. E. Alvarez, D. E. Resasco, *Catal. Today*, 62 (2000) 159.
[65] M. Scheithauer, R. K. Grasselli, H. Knözinger, *Langmuir*, 14 (1998) 3019.
[66] L. M. Petkovic, J. R. Bielenberg, J. R. G. Larsen, *J. Catal*., 178 (1998) 533.
[67] N. R. Shiju, M. M. Anil. Kumar, W. F. Hoelderich, D. R. Brown, *J. Phys. Chem. C*, 113 (2009) 7735.
[68] Bert, W. M., *Nat. Mater*., 9 (2009) 690.
[69] W. Zhou, E. I. Ross-Medgaarden, W. V. Knowles, M. S. Wong, I. E. Wachs, C. J. Kiely, *Nat. Mater*., 1 (2009) 723.

Chapter 2 Theoretical Methods and Computational Techniques

"The door to every new comprehensible scientific theory takes me one step closer to the marvellous beauty of that intelligent design".

— *Greeshma Nair*

2.1 Introduction

This chapter will look into the detail at the theoretical and computer modelling techniques applied in this work. The objectives of these techniques are to predict the crystal properties of pure t-ZrO_2 and then describe the effects of WO_3 additions to it. The chapter begins with a general introduction to the methods of computer modelling which are employed to generate the results in the rest of the thesis. To obtain a better understanding of the catalyst systems the results from the modelling techniques discussed here, were compared with the observation from the experimental techniques. We investigated the most technologically important phase of zirconia and looked at its bulk, surfaces and defect properties. In order to study these properties GULP [1, 2] (General Utility Lattice Program) and METADISE [3] (Minimum Energy Techniques Applied to Dislocation, Interface and Surface Energies) codes were chosen. These codes are used at first to investigate the bulk defect and surface properties of pure t-ZrO_2 and WO_3 doped zirconia. After levels of good agreement with the previously reported studies were

achieved, an attempt was made to make these results comparable with the experimental conditions. One way to do this was to utilise molecular dynamics. The molecular

dynamics technique incorporates the effect of temperature and pressure thus enabling a better comparison with experimental findings. In these methods the trajectories of atoms and molecules are determined by numerically solving Newton's equations of motion for a system of interacting particles. All the methods described above involve the evaluation of an expression for the energy of a given geometric arrangement of atoms. An equilibrium structure is then obtained by variation of the atomic position to minimize the energy expression i.e. energy minimization. [4]

Modelling techniques of these types are collectively known as atomistic methods and in this work are based on interatomic potentials (force-fields). The interatomic potentials used in these methods are discussed in detail in Chapter 3. This chapter explains the various optimisation techniques with relevance to the strength and weakness of each technique. It also discusses how they are applied to bulk systems, surfaces and point defects as well as gives some basic concepts of the molecular dynamic package used in this work.

2.2 Basic Crystal Concepts

A crystal is a solid material with a regular periodic arrangement of atoms in three dimensional space. This arrangement of atoms could consist either of a single type of atom such as in a metal or different types of atoms forming a complex structure. [5] The symmetries of these repeated patterns in space determine the structure of the unit cell. The vertices of all unit cells in space constitute a lattice, while the arrangement of atoms particular to the specified material, which on repeating gives the entire crystal structure is known as the basis. Both lattice and basis are thus very important parameters to define the crystal structure. The entire symmetry of the crystal from a microscopical perspective is defined by the space group. [6] Space groups in three dimensions are made from combinations of the 32 crystallographic point groups with the 14 Bravais lattices, [7] each of the latter belonging to one of 7 lattice systems. The space group of zirconia studied in this thesis is $P4_2$ /nmc. The different types of crystal system existing in nature are Monoclinic, Tetragonal, Hexagonal, Orthorhombic and Cubic see Figure 2.1. The crystal structure of the zirconia polymorph used in this thesis is of the body centered tetragonal form. [8] The next phase is to find the most stable structure an energy minimum by carrying out energy minimisation using the computational codes which are discussed in the next section.

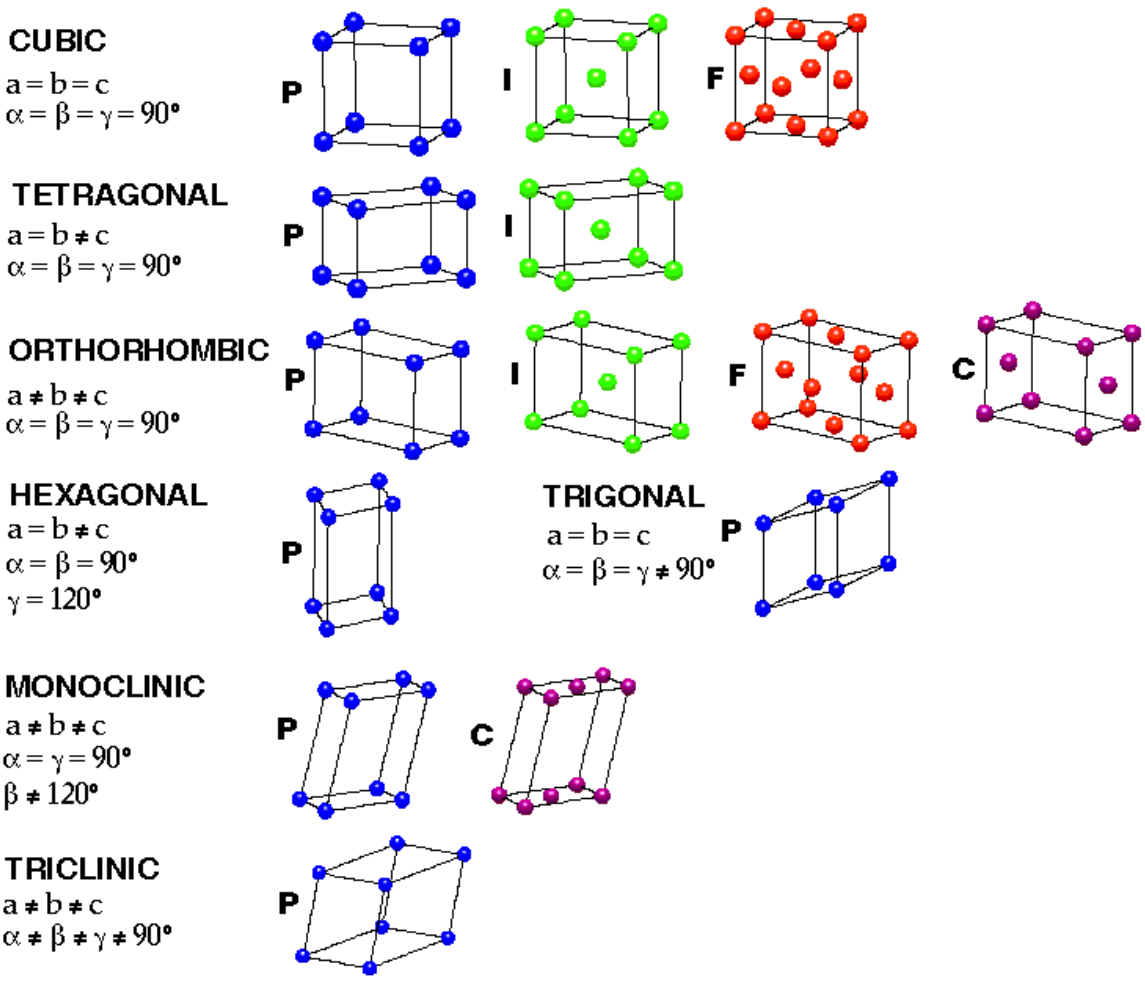

Figure 2.1 Different types of three dimensional lattice structures; ***P*** *= Primitive,* ***I*** *= Body Centred,* ***F****=Face centred,* ***C****= Side Centred. (Internet resources)*

2.3 Static – Lattice Energy Minimisation

2.3.1 Simulation Codes

The static minimization techniques applied in this work are implemented in two computational codes: METADISE [3] (Minimum Energy Technique Applied to Dislocation Interface and Surface Energies) and GULP, [1, 2] (General Utility Lattice Program).

METADISE: Most of the static simulations for this work have been carried out using this code. Using the interatomic potentials incorporated within the code, the energy of the bulk and surfaces of t-ZrO_2 with and without the addition of dopants were calculated. For calculating the surface energies, a two dimensional periodicity implemented in the METADISE was employed. Using this code, slabs of t-ZrO_2 and WO_3 doped zirconia were prepared with various configurations, which served as the input files for the molecular dynamic calculations. In this study the Viewerlite software has been used to visualise the geometric configurations.

GULP: The energetics of defective surfaces was determined using this code. It enabled us to calculate the point defects using the Mott-Littleton [43] approach. This code has also been employed in this thesis to calculate the phonon density of states in pure t-ZrO_2. To calculate this, GULP uses a standard scheme developed by Monkhorst and Pack [24] for

choosing the grid points and then frequencies are integrated over the entire Brillouin zone.

The calculation of lattice energy serves as the fundamental objective for all solid state simulation techniques. In order to describe a perfect crystal, the calculated lattice energy achieved should be a minimum. [9] This can be achieved in two ways:

Constant Pressure minimisation (conp): Using periodic boundary conditions (PBC) [10] here (see Figure 2.5), the total energy in a unit cell is minimised keeping the pressure constant in a system but allowing the cell dimensions to change. In this thesis the static simulation of bulk t-ZrO_2 begin with a constant pressure minimisation using the METADISE code.

Constant volume minimisation (conv): In this approach, the volume is kept constant and hence the cell dimensions are maintained at a constant value.

When used in conjuncton with a potential model; these techniques can be readily applied to systems containing 10,00,000's of atoms. Although their efficiency when working with large system is dependent on the minimization algorithm chosen. Also they can give good agreement with experiments and *ab-initio* [11] calculations, however, the static methods are unable to predict the vibrational properties of a system due to the effects of temperature. In spite of this drawback, the static methods are widely applied to study many bulk, surface and defect properties of crystal lattice. For example the defect structures and migration pathways were accurately predicted for cubic zirconia using the

static techniques. [12] Similarly static simulation techniques have been successfully applied to study the oxygen vacancy and dopant segregation at the grain boundaries boundaries of ceria. [13-15] In order for these methods to function properly, the optimisation techniques chosen to find the minimum energy should be highly efficient and accurate. The next section describes the various optimisation techniques used for the minimisation methods.

2.3.2 Optimisation Techniques

In order to calculate the energy of the system reliably and efficiently it is important that the energy minimisation techniques, chosen will detect the minimum corresponding to the most stable configuration. [16-18] In their simplest form all such approaches essentially consider an initial configuration and adjust it to give a lower total energy, which can then be further reduced to a minimum value by an iterative method. This iterative method makes small changes in the geometry of the structure and checks if the energy has decreased. The number of iterations required depends on four important factors which are: 1) the nature of the minimization algorithm, 2) the form of the energy function, 3) the number of atoms and 4) the curvature of the potential energy surface. Some of the efficient algorithms commonly used are the *Line search*, *Steepest descent*, *Conjugate gradient* and *the Newton Raphson variable matrix method*. [19-21]

Throughout this thesis the Newton Raphson matrix variable method has been used for energy minimisation calculations. This is a very effective method and employs at first the gradient method to identify the direction of the search and then calculates the second derivative in order to determine the minimum values. However, the required inversion of the 2nd derivative matrix is time consuming and can be overcome to some extent by using approximations such as Broyden-Fletcher-Goldfarb-Shanno (BFGS) algorithms or the Davidon-Fletcher-Powell (DFP). [22, 23] In a purely Newton-Raphson approach the atom positions, after n iterations, r_n, the forces acting on the system $dU/dr_n = g_n$ and the second derivative matrix $d^2U/dr_n = dg_n/ dr_n = W_n$ are calculated and used to determine the new coordinates, $r_{n+1,}$ via the Equation below,

$$r_{n+1} = r_n - g_n . H \qquad (2.1)$$

where H is the Hessian Matrix and is equivalent to $W^{-1}{}_n$

A perfectly harmonic system would need only a single step to locate the minimum energy position. However, for complex systems, several iterations must be performed until there is not net force acting on the system, g = 0. The major drawbacks of this method are the second derivative matrix is computationally expensive to calculate for large systems and in case if the Hessian is not positive, Newton-Raphson procedure will converge towards the maximum along any imaginary mode instead of the minimum. Hence, for very large systems an alternative to the Newton Raphson mehod is used, which is the Conjugate

gradient minimisation method. In this method the requirement of a Hessian not needed. Although this method is less time consuming, it also possesses less accuracy.

There are many improvements to the energy minimisation techniques. One of these is Broyden Fletcher Goldfarb and Shanno (BFGS) method. The advantage of using this method is that it can save a lot of computer time as well as gives good accuracy in cases where the system is a long way from minimum. In these kinds of quasi-Newton methods instead of a true inverse matrix, an initial matrix is chosen which is updated using a formula. In the BFGS method it calculates the optimum structure by minimising the forces *(g)* acting on the atoms located at coordinates *(r)*. During the course of successive iterations, an inverse second derivative matrix H_i is created such that $\lim_{i\to\infty} H_i = W^{-1}$, where W^{-1} is the true inverse matrix of second derivatives. BFGS is a powerful technique and most of the simulation codes utilises these methods for energy minimisation.

2.3.3 Optimisation of Unit Cell Dimensions (Constant Pressure Minimisation)

As mentioned previously one important extension to lattice energy minimisation is the ability to adjust the size of the unit cell dimensions during the minimization as this ensures there is no external pressure acting on the system and allows for reconstruction to occur. This is achieved by performing a *conv* minimization then adjusting the lattice vectors according to the bulk strain ($\Box$) as shown below:

$$\Box = C^{-1}\sigma \qquad (2.2)$$

where the stress σ is the sum of the applied and static pressures ($\mathbf{P_{static}}+\mathbf{P_{applied}}$) and the static pressure is defined as $\mathbf{P_{static}} = (1/V)(\partial U_L / \partial \in)$ and C is the compliance matrix (the second order derivatives of lattice energy with respect to strain). This process is itself performed iteratively until the required static pressure is achieved within the appropriate tolerance.

2.3.4 Periodic boundary condition

Periodic boundary conditions (PBC) are employed to limit the computer time required to model a system of realistic size. This enables mimicking of an infinite system by a box of finite size in such a way that when a particle leaves the simulation box an image rejoins the box on the opposite side as shown in Figure 2.2, so that the box remains constant. The box containing the particles are surrounded by images of itself and thus producing an infinite repeat of the simulation cell in either one, two or three dimensions. Periodic boundary conditions are therefore very effective in modelling crystalline materials and it is also adequate for liquids or amorphous materials provided that any long-range properties are not considered or the simulation cell is sufficiently large that the properties converge within the periodic boundary.

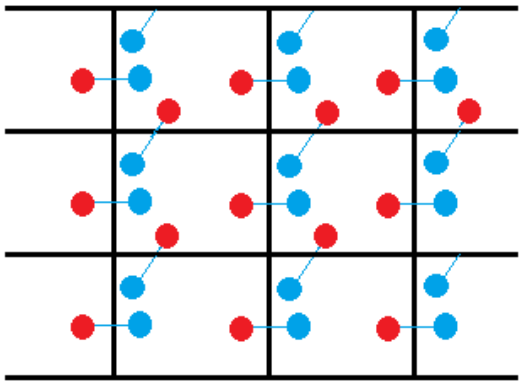

Figure 2.2 An illustration of Periodic Boundary Conditions

2.3.5 Application to Surfaces

Computer modelling of solid surfaces employs a simulation cell periodic in either two-dimensions for static simulation or three-dimensions for molecular dynamic simulations.

2.3.5.1 Generating Surfaces and Types of Surfaces

In order to create a surface, the bulk cell is cleaved in a particular direction specified by a notation system called Miller indices. These are written as ($hk\ell$), and each index denotes a plane orthogonal to a direction (h, k, ℓ) in the basis of the reciprocal lattice vectors. [26] In this thesis the planes {101}, {001}, {100}, {110} and {111} planes were chosen to be cleaved in the body centered t-ZrO_2 bulk structure. To clearly understand the location of these planes they are represented within the unit cell of t-ZrO_2 see Figure 2.3. The important factor to consider while cleaving a surface is that, there should be no dipole perpendicular to the repeat unit of the crystal. If dipole is present, then the convergence of surface energies becomes difficult and may diverge leading to errors in calculations. This can be overcome by adequate reconstruction of the surface during the minimisation, which will enable the removal of the dipole.

According to Tasker, [26] a crystal is considered to consist of a stack of charged planes. The configurations of atoms in these planes give rise to different types of surface arrangements. In general three types of surface arrangements exist, Type 1, Type 2 and

Type 3. Type 1 surfaces maintain a stoichiometric ratio of ions in each layer. Since there are equal number anions and cations the total charge is zero and the net dipole is also zero for each repeat unit. In the case of t-ZrO_2, this type of surface was noted for the surface {100}. In Type 2 surfaces, although each layer consists of charged planes, a symmetrical configuration exists resulting in the cancellation of the total charge as well as the dipole in each repeat unit. This type of surfaces were found for {101}, {111} and {001} surfaces in t-ZrO_2. In Type 3 surfaces alternately charged planes are stacked together which produces a dipole moment perpendicular to the surface. This is not as stable configuration as the other two types and hence a reconstruction is essential to bring stability in this type of surface. The reconstruction is done by removing half of the ions in the surface layer at the top of the repeat unit and transferring them to the bottom which produces a highly defective surface. Normally in nature, Type 3 surfaces are found to exist in doped conditions. In the case of t-ZrO_2 it was found that the surface {110} was a Type 3 surface. The Figure 2.4 shows all the three types of surface arrangements.

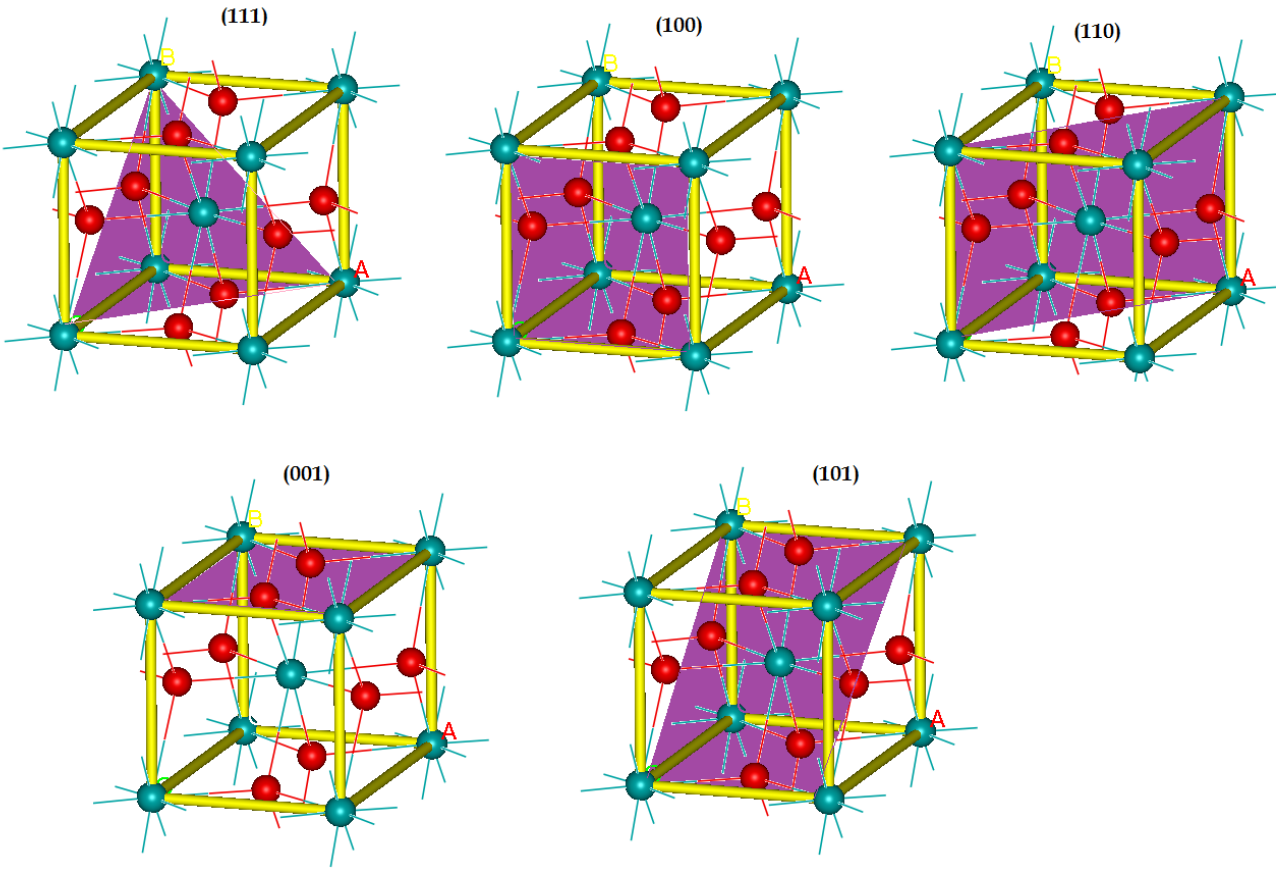

Figure 2.3 Planes with different Miller indices in body centered t-ZrO_2.

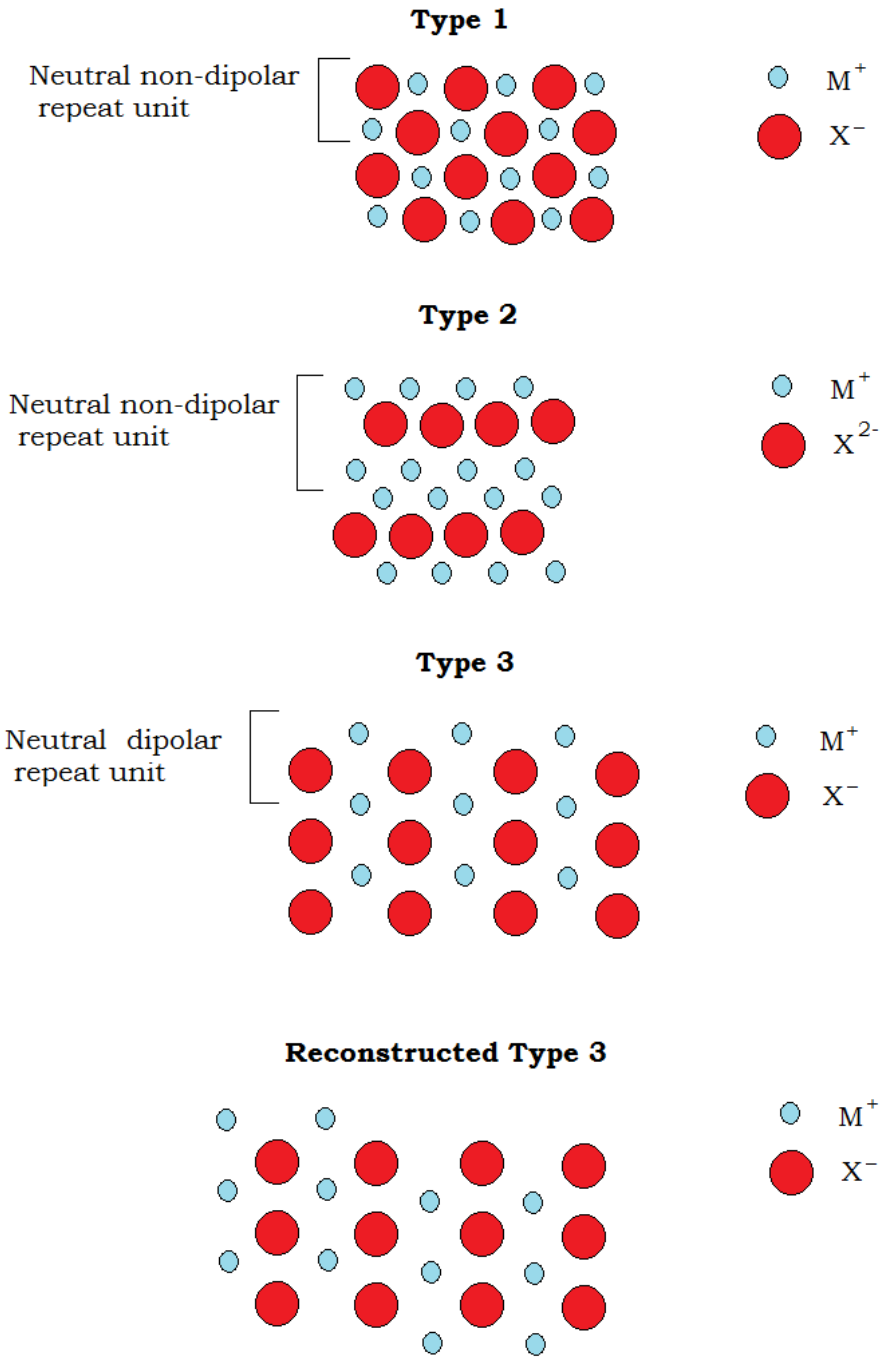

Figure 2.4 The three types of stacking sequence described by Tasker and reconstructed Type 3 surface.

2.3.5.2 Two-dimensional Periodicity

One method for describing a surface is to consider the crystal as a series of (charged) planes parallel to the surface and periodic in two dimensions. Such an approach was first described by Tasker (1978) and implemented in the MIDAS code. [50] A bulk crystal is made up of two blocks, each of which is divided into two regions, region I and region II. The ions in region II are held fixed at their equilibrium position, while ions in region I are allowed to relax relative to region II. A surface is created when the two blocks are separated. This is illustrated in the Figure 2.5. Chapter 5 in this thesis deals with the creation of surfaces.

The total energy of the surface if therefore made up of two parts,

$$E_{total} = E_1 + E_2 \qquad (2.3)$$

Where E_1 and E_2 are the energies of the ions in region I and region II respectively. The energy of region I is given as shown below:

$$E_1 = \sum_{\substack{i\in I \\ j\in I}} \sum_{l} \Psi_{ij}\left(\left| r_{ij} - r_l \right|\right) + \frac{1}{2}\sum_{\substack{i\in I \\ j\in II}} \sum_{l} \Psi_{ij}\left(\left| r_{ij} - r_l \right|\right) \qquad (2.4)$$

where the first term includes interactions between the ions in region I and the second term the interactions between the ions in region I and region II. The energy of region II consists of only the second term as the ions are kept fixed and hence the interactions between the ions in region II is unchanged. The energy contribution is therefore given by Eq (2.5).

$$E_2 = \frac{1}{2}\sum_{\substack{i\in I \\ j\in II}} \Psi_{ij}\left(\left| r_{ij} - r_l \right|\right) \qquad (2.5)$$

To calculate the surface energy of a crystal face, two calculations are carried out, one using a surface block and the other one using a bulk block. The surface energy is then derived as shown in Eq. (2.8). If the energy of the surface block is E_S and the bulk block is E_B then these energies can be broken down into the following components:

$$E_S = E'_{I\text{-}II} + E'_{I\text{-}I} + E'_{II\text{-}I} + E'_{II\text{-}II} \qquad (2.6)$$

$$E_B = E''_{I\text{-}II} + E''_{I\text{-}I} + E''_{II\text{-}I} + E''_{II\text{-}II} \qquad (2.7)$$

Where $E_{I\text{-}I}$ is the interaction energy of ions in region I with others in region I, $E_{I\text{-}II}$ is the interaction energy of all ions in region I with all the ions in region II. Since the ions in Region II do not relax, the total interaction energy, $E_{II\text{-}II}$, of all the ions in Region II with all the other ions in Region II does not change, and will therefore cancel in the surface

energy calculation. The surface energy (γ) of a crystal face is defined as the excess in energy of a surface simulation over the energy of a bulk system containing the same number of atoms per unit area and is therefore described by the equation given below. The surface energies of pure and doped surfaces were calculated for t-ZrO_2 and are discussed in Chapters 5 and 7.

$$\gamma = (E_s - E_B)/Area \qquad (2.8)$$

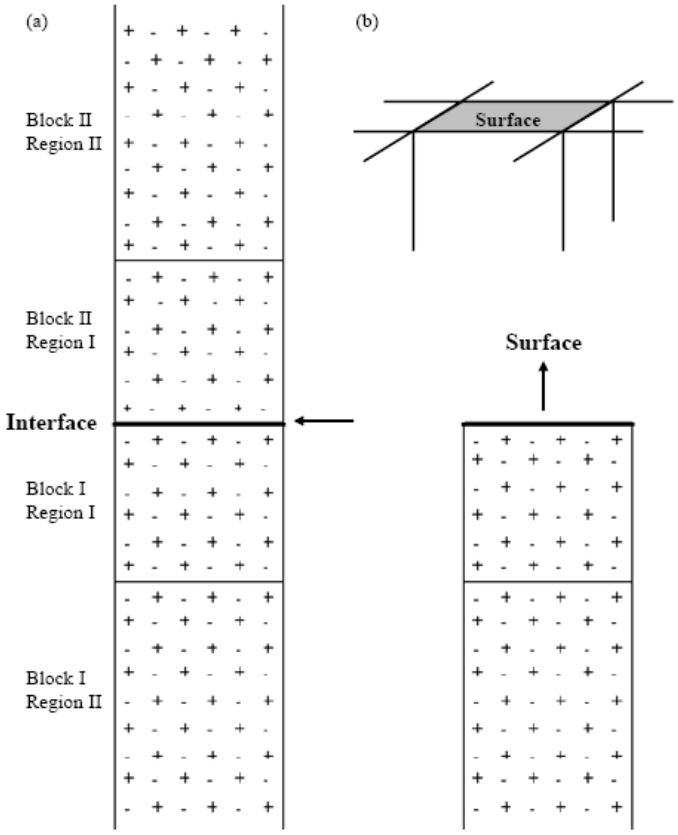

Figure 2.5 The two region approach used in METADISE. (a) the complete crystal and (b) half a crystal, exposing a surface, periodic in two dimensions.

2.3.5.3 Three-Dimensional Periodicity

Apart from the two dimensional PBC applied for the study of surfaces by static simulations, this thesis also makes use of the three dimensional PBC to describe surfaces as slabs. In this case the system is first relaxed to the bulk structure and oriented so that two of the three lattice vectors are parallel to the surface. The third vector, which is now perpendicular to the surface, is then increased in size, producing repeating crystal slabs. The chosen surfaces are on opposite sides of this crystal slabs (see Figure 2.6). This void must be large enough that there are no interactions between atoms on opposite surfaces. In this thesis a void gap of 60 Å was used to overcome the effects of these interactions (see Figure 2.6) The crystal slab must also be thick enough so that the two surfaces on opposite sides do not interact. This approach is used because the summation of the Coulombic energy for a three dimensional simulation cell is very efficient. Only methods which keep the cell volume constant should be used when optimizing slabs, to avoid the bulk structure from being reformed, as this will always be thermodynamically more favourable than the surface.

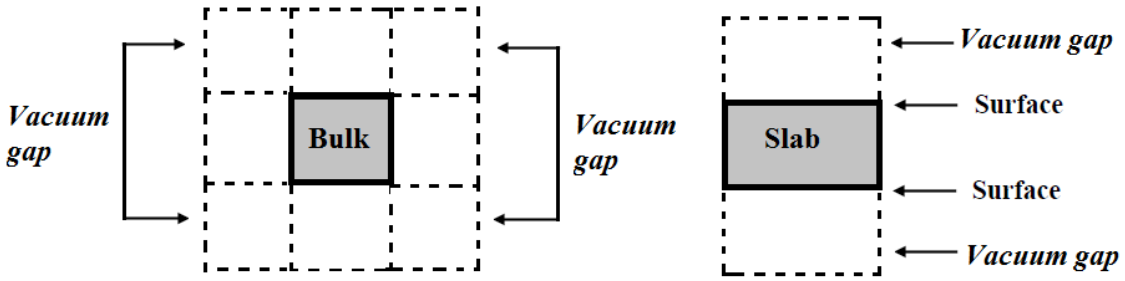

Figure 2.6 Schematic representation of introducing vacuum gaps in bulk and surfaces of a simulation cell.

2.3.5.4 Surface Area Calculations

This thesis tries to understand the mechanism of stabilisation of tetragonal zirconia in the presence of WO_3 species. In case of catalytic materials it is generally known that the larger the surface area the higher the catalyst activity. [28-30] Since WO_3-ZrO_2 catalysts are widely used in many reactions, [31-33] the knowledge of its surface area is an important criterion for its application as an active catalyst. The surface areas of the slabs for different surface structures are discussed in Chapter 8.

There are five different ways of describing the types of surface area [34-36] that can be attained:

1) *Van der Waals surface*: This surface is constructed by the overlapping of Van der Waals spheres of the atom.

2) *Molecular surface*: This is traced out by the inward-facing part of the probe sphere as it rolls on the Van der Waals surface of the molecule.

3) *Contact surface*: consists of the regions where the probe is in contact with the van der Waals surface.

4) *Re-entrant surface*: regions occur where there are crevices too narrow for the probe molecule to penetrate.

5) *The solvent accessible surface*: the surface traced by the centre of the probe molecule.

In this thesis we estimated the molecular surface areas for both pure t-ZrO_2 as well as WO_3 doped zirconia on the top surface of slabs using the GDIS software package. [35] GDIS evaluates the molecular surface areas using its *Iso-surface* in the Visualisation options. These are obtained using the Gaussian description of molecular shape. [36] The idea is to use rolling a probe atom which has a certain diameter and rolled over the surface of the system being studied see Figure 2.7.

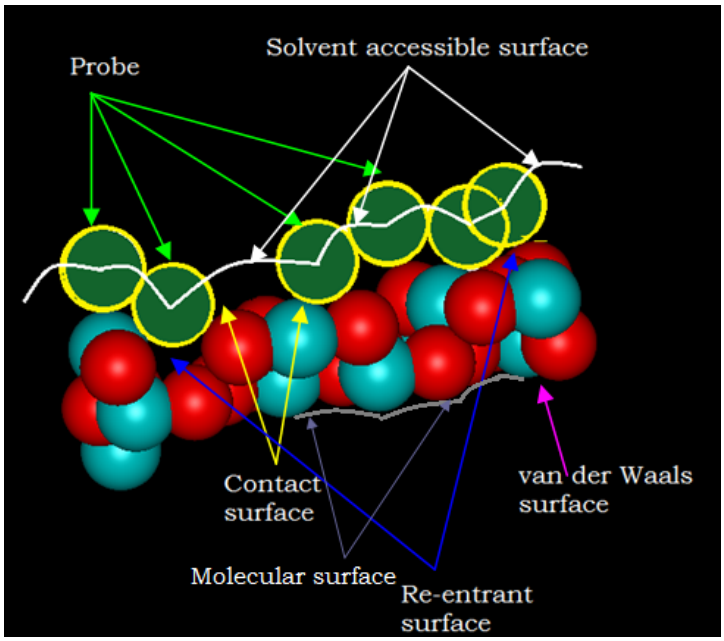

Figure 2.7 The image created for depicting the various types of surface areas and its measurement techniques on the surface of t-ZrO_2.

2.3.6 Crystal Morphology

One of the key issues for designing an active catalyst in heterogeneous catalysis is the proper identification of the exposed facets. The Chapter 8 of this thesis deals with the identification of crystal morphology for both pure t-ZrO_2 and WO_3 doped zirconia. This will give us an idea about the relative growth of the catalytically favourable surfaces. Generally the growth rate of a crystal is directly related to its surface free energies. To compute this, the Wulff construction is plotted. [37] According to Wulff, the equilibrium

shape of the crystal could be determined by minimising the total free energy of the system. It is considered that in its equilibrium shape, the height of each face is directly proportional to the specific free energy and this ratio is constant. If γ_i is the specific free energy of the i^{th} plane, and h_i is the distance from the centre of the crystal to the i^{th} plane this can be expressed as

$$\frac{\gamma_1}{h_1} = \frac{\gamma_2}{h_2} = \frac{\gamma_3}{h_3} = \frac{\gamma_4}{h_4} = \frac{\gamma_n}{h_n} \qquad (2.9)$$

However, as discussed previously, surface energies are computed rather than free energies. It is however reasonable to assume that the surface energy is proportional to the surface free energy and thus this can be used in determining the Wulff constructions.

In 1878, Gibbs [38] proposed that for the equilibrium shape of a crystal, the total surface energy should be a minimum for a constant volume of crystal. It was proposed that the faces that have high surface energies will grow faster than those with low surface energy. However, the low surface energy faces will occupy more surface areas resulting in becoming the dominant plane in the morphology.

2.3.7 Point Defects

In 1926 Frenkel introduced the notion of point defects in crystalline solids to elucidate the phenomenon of diffusion. [39] Now it is understood that not only diffusion but almost all properties of crystalline solids are affected by defects and, in particular, by point defects. Point defects are defects in the crystal which include vacancies, interstitials or substitutional impurities arising due to the presence of foreign atoms within the crystal structure. The missing of an atom results in a vacancy, while an extra atom that has crowded into an interstitial void result in a self-interstitial and an impurity on an interstitial site results in a dopant interstitial. The presence of a foreign atom that has replaced the bulk atom causes a substitutional impurity. All these defects have a great influence on the properties of the material, such as diffusion, chemical reactions, phase transformations etc. Hence, it is important to understand the types of point defects that may dominate in a crystal.

These point defects are usually represented using Kröger-Vink notation, [40] which describes the charge and position of the point defect in crystals. This form defines the defect in three parts, a main symbol, a subscript and a superscript. The vacancy or chemical name of the atom is used as the symbol. The subscript denotes site at which the defect is placed. A superscript gives information of the charge with respect to the normal charge of the species. For example, $V_O^{\bullet\bullet}$ denotes an oxygen vacancy, whereas an oxygen interstitial is represented as $O_i^{//}$.

2.3.7.1 Types of point defects

Depending on the stoichiometric compositions these point defects are generally classified as intrinsic and extrinsic defects. An intrinsic defect does not involve any foreign atoms, these include vacancies, self interstitials and Anti-site defects in a crystal. Extrinsic defects involve the presence of other types of atoms within the crystal structure such as foreign atoms present as impurities in a crystal. In ionic crystals the intrinsic disorder gives rise to two types of mechanisms the Schottky defect [41, 42] and the Frenkel defect. [39] In a Schottky defect, oppositely charged ions are removed from the lattice in such a way that the charge of the entire crystal is maintained neutral. The Frenkel defect involves the movement of an ion from its lattice site to an interstitial site. This creates a vacancy in its initial lattice site. These defects normally occur due to thermal vibrations and it is believed that no such defects will exist in a crystal at zero Kelvin. Figure 6.4 in Chapter 6 shows both the Schottky and the Frenkel defect mechanism in t-ZrO_2 crystal.

2.3.8 Modelling Point Defects in Bulk Crystals

Perfect crystals never exist in nature, as imperfections like point defects, dislocations, grain boundaries etc are always found within a crystal lattice under real conditions. Hence for predicting properties including the effects of defects in a crystal lattice, it is necessary to simulate these defects on both bulk and surfaces. In this thesis the effects of point defects on both bulk and surfaces are analysed in Chapter 6. Two different approaches are utilised to calculate point defects in bulk systems using the static

simulation codes. The first approach is a periodic supercell method and the second one is a cluster based Mott-Littleton method based on the approximation. [43]

2.3.8.1 Supercell Method

In this method the size of the unit cell is increased as much as possible so that there are no defect-defect interactions. This method uses three dimensional periodic boundary conditions and is good to use when the number of defects is large in a given structure. However the method can converge slowly especially when the defects are charged. This can make the method computationally expensive. One solution is to perform a series of simulations on supercells of varying size. The converged energy is then the intercept of a plot of Energy *vs* 1/ (lattice site). The energy to form an isolated defect is then given by:

$$E_{def} = E\,[W\text{-}ZrO_2] - E\,[ZrO_2] \qquad (2.10)$$

Where E[W-ZrO_2] is the energy of the zirconia surface doped with a tungsten (W) atom, while E[ZrO_2] is the energy of the pure surface of zirconia.

2.3.8.2 Mott-Littleton Method

Using this approach to calculate the defect energies, the system is divided in to two regions. Region I contains the defect and the atoms surrounding the defects. The Region II is further divided in two regions, the inner part and the outer part. The inner part (Region IIa) has weak influence of the defect and the ions in this region are assumed to be constrained within a harmonic well. In the outer region (IIb) which extends to infinity is modelled by a quasi continuum approximation. The Figure 2.8 shows the schematic representation of this two region approach.

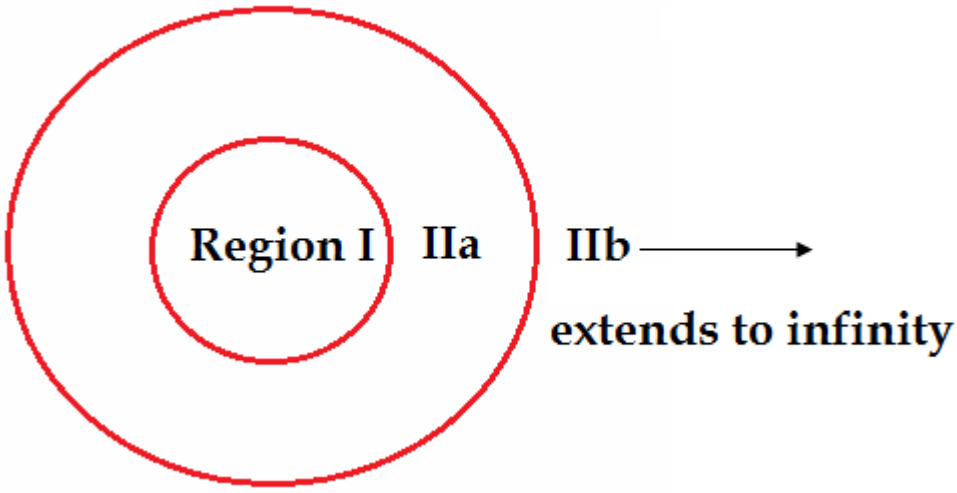

Figure 2.8 Schematic diagram of the Mott-Littleton method dividing the crystal into three regions.

The defect energy by this method is calculated as follows:

$$U(x,y) = U_1(x) + U_2(x,y) + U_3(y) \quad (2.11)$$

Where $U_1(x)$ is the energy of the inner region, $U_2(x,y)$ is the interaction between the two regions and $U_3(y)$ is the energy of the rest of the crystal. The advantage of this method over the supercell method is that, it allows charged defects to be treated more efficiently and like the supercell method it is important to ensure the calculated energy has converged with the size of region I and II a. This usually occurs quickly and can be assessed directly from plots of energy vs region size.

2.3.9 Modelling Point Defects at Surfaces

When modelling point defect on surfaces the computer program CHAOS was utilised in this thesis. The CHAOS code developed by Duffy and Tasker [44] is based on a two region approach similar to the Mott-Littleton method; however, here the regions are hemispheres of ions, centred on the defect see Figure 2.9. This approach is incorporated within the static simulation using the METADISE code; at first the structure of the pure lattice is calculated and the energy of the discs of ions lying parallel to the surface is summed. A modification to the Mott-Littleton method is made here for evaluating the defect energies by calculating the energy as a sum of planar integrals around the interfaces and a volume integral over the rest of the crystal as shown in Eq (2.12). While allowing for the calculation of clustered defects, this method converges poorly. In such

cases, it is generally easier to use an approach based on supercells where defects are added to a large 2D surface or 3D slab set up. This also has the advantage that the effect of concentration can be considered. This method is discussed from the Chapter 6 when calculating the point defects on the pure and doped surfaces of t-ZrO_2, as well as checking the oxygen migration on surfaces.

$$E_{IIb} = -\frac{Q^2}{2}\sum_{p\in I,IIa}\sum_{k} q_k K_k \int^{\infty} \frac{1}{\sqrt{(R_{IIb}^2 - r_b^2)}} \frac{1}{(r^2 + r_p)^2} 2\pi dr + \frac{1}{2}\sum_{k} q_k K_k \int_{R_{IIb}}^{\infty} \frac{1}{r^4} 4\pi r^2 dr \quad (2.12)$$

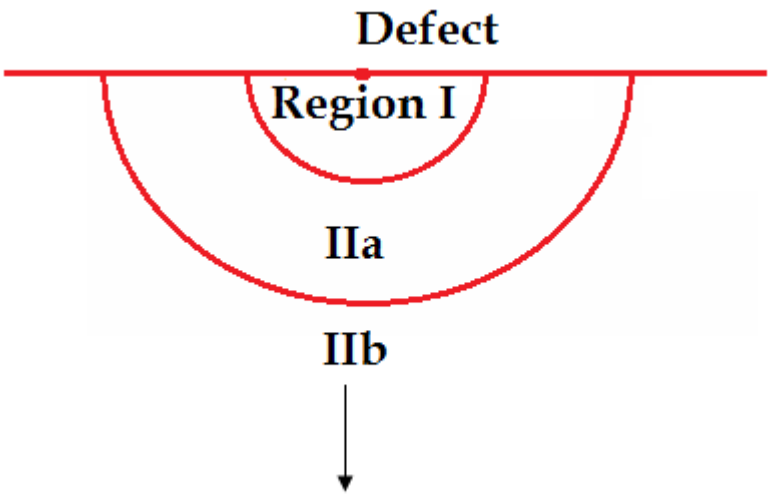

Figure 2.9 Schematic diagram of two region approach used in the CHAOS program.

The perpendicular distance between the origin and plane p is represented by r_p and the total charge in region I by Q. There also exist interaction of these charged defects with their image and for cases where two materials have different dielectric constants; the image charge interaction is given by:

$$q_i = q_{def}\left(\frac{\in_1 - \in_2}{\in_1 + \in_2}\right) \tag{2.13}$$

where q_{def} is the net charge of the defect.

2.3.9.1 Segregation of Defects

The movement of defects towards or away from a surface, interface or boundary is known as segregation. The effect of segregation of atoms can have a profound influence on the properties in a crystal especially when there is significant movement of defects. The segregation energy is defined as the energy difference between placing an impurity at the surface with placing the same impurity in the bulk. The segregation and defect surface energies are calculated as follows:

$$E_{seg} = E_{def}\,(surf) - E_{def}\,(bulk) \tag{2.14}$$

$$\gamma_{def} = \frac{E_{surf+def} - (E_{bulk} + nE_{def})}{Area} \tag{2.15}$$

Where n, is the number of defect atoms per area. To calculate the energetics of ionic substitution, it is necessary to also calculate the solution energy for the substitution. To calculate this it is assumed that when the dopant ions were introduced into the bulk lattice, the dopant ion replaces the bulk atoms to form a complex. The solution energy is the total energy involved in this process, and it gives an indication of the ease of substitution of the dopant ion into the lattice. In this thesis at Chapter 6 the segregation energy and solution energy of different mechanism of possible defect on WO_3 doped t-ZrO_2 are discussed.

2.4 Molecular Dynamics

This technique is used to model the kinetic and thermodynamic properties of molecular systems using the Newton's law of motion. It was first introduced by Alder and Wainwright in the late 1950's to study the interactions of hard spheres. [45, 46] The first molecular dynamics simulation of a realistic system was done by Rahman and Stillinger in their simulation of liquid water in 1974. [47] It clearly predicts the thermal properties for different materials as well as extracts the data about its dynamic behaviour at the atomic scale. However since Newton's equation of motions are classical by nature, no quantum effects or electronic states are taken into account. Although a great deal of information regarding the electronic states could be predicted using these techniques. One such method applied in this thesis was to propose the mechanism of electron delocalization using the RDF analysis obtained by MD calculation. MD simulations are

widely used in chemistry, for determining the structural variations occurring in a molecule and calculate the energies of the molecular systems. This technique is fast and computationally more efficient in calculating the energy of larger molecular systems but can be computationally expensive due to the number of steps required to achieve convergence. In this thesis the results obtained from the MD calculations provide an insight to suggest new experimental directions. A simple MD calculation considers a box of N particles and monitors their relative position, velocity and acceleration. Each particle is assigned a pseudo-random velocity, which is determined from a Boltzmann distribution. Eq (2.16) and (2.17) describes the initial conditions necessary to define these.

$$\sum_{i=1}^{N} m_i v_i^2(0) = 3Nk_bT \tag{2.16}$$

$$\sum_{i=1}^{N} m_i v_i(0) = 0 \tag{2.17}$$

Where m_i and v_i are the mass and the velocity of particle *i*. At finite intervals Newton's equation of motion are solved by calculating the forces acting on each particle at a small time step, given below as:

$$a_i(t) = \frac{F_i}{m_i} \tag{2.18}$$

$$v(t+\delta t) = v(t) + a_i(t)\delta t \quad (2.19)$$

$$r_i(t+\delta t) = r_i(t) + v_i(t)\delta t \quad (2.20)$$

One of the major limitations of this technique is that the size of the systems considered here is very small compared to real crystals. This affects the thermodynamic equilibrium at the start of the calculation causing temperature fluctuations. A correction to this is made by increasing the velocity at regular intervals where a convergence of kinetic energy of the entire system is achieved at the required temperature. The time steps chose in a MD calculation needs to be shorter than the period of any lattice vibration to achieve accuracy in the calculated properties. However the choice of a shorter time step results in an increasing number of iterations requiring more computational time. Therefore a compromise which offsets the length of time step with the CPU time reasonably to provide a more realistic approach

2.4.1 Integration Algorithms

The potential energy is a function of the atomic positions (3N) of all atoms in the system. Due to the complicated nature of this function, there is no analytical solution to the equations of motion; they must be solved numerically. The desirable features of an integration algorithm are to achieve a good accuracy for computing the forces at large time steps. Various numerical algorithms have been developed for solving these equations of motion. All these algorithms utilize a Taylor series to describe the positions, velocities and accelerations.

One of the popular integration algorithm used is the Verlet algorithm. [48] This method is a direct solution of the second order Eq. (2.18) in which the particle's position vectors which are the coordinates of the atom are expanded as a Taylor series. This method has been shown to have excellent energy conserving properties even with longer time steps. However, this algorithm does not provide any information on the velocities of the particles; hence a modification of this method known as the Verlet Leapfrog Algorithm (VLA) [49] overcomes this. The Verlet Leapfrog calculates the velocities using the position terms r_i at every time step. The position terms are calculated from the basic Verlet algorithm. The Figure 2.10 shows the successive steps of a simple Verlet algorithm. The VLA can be expressed by Equations (2.21 to 2.23) below:

$$r(t+\delta t) = r(t) + v(t+\tfrac{1}{2}\delta t)\delta t \tag{2.21}$$

$$v(t+\tfrac{1}{2}\delta t) = v(t-\tfrac{1}{2}\delta t) + a(t)\delta t \tag{2.22}$$

$$v(t) = \tfrac{1}{2}\, v(t+\tfrac{1}{2}\delta t) + v(t-\tfrac{1}{2}\delta t) \tag{2.23}$$

At first the Eq. (2.22) is implemented and the mid-step velocity is calculated, while Eq. (2.23) is used to calculate the velocity at the current step. This also facilitates the calculation of the energy at a certain time (t) and other variables which are functions of r_i and v. The new positions of all particles are given by Eq. (2.21), after which the next iteration will be ready to calculate the accelerations.

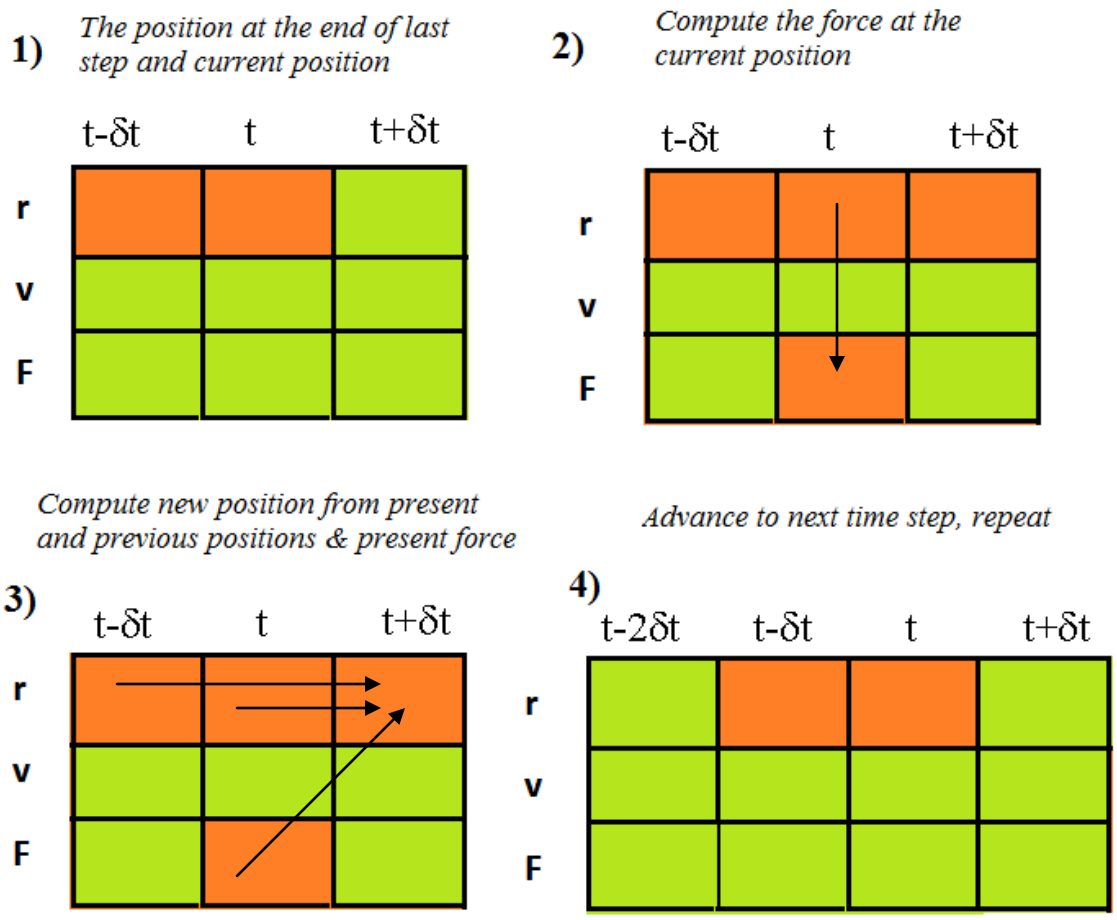

Figure 2.10 The Successive steps in the implementation of Verlet algorithm are shown. In each case, the stored variables are in the orange boxes.

2.4.2 Thermodynamic Ensembles

In 1989 Allen and coworkers [51] envisaged a method by which these MD calculations can offer more realistic comparisons with experimental conditions. Their method incorporated certain conditions known as Ensembles to address the issues relating to

change in variables such as temperature, pressure, volume etc. These ensembles can be directly chosen for a certain MD run. [51, 52]

In the microcanonical ensemble (NVE), the volume of the system is maintained at a constant value and is isolated from the surroundings and has a constant energy and constant number of particles. This is the simplest form of simulation.

In the canonical ensemble (NVT), the temperature, volume and number of particles have a specified value, while the total energy of the system is allowed to fluctuate.

In the isothermal-isobaric ensemble (NPT), the pressure, temperature and number of particles have a specified value, while the instantaneous volume (V) of the system can fluctuate.

The grand-canonical ensemble (μVT) has a constant volume and temperature (as the canonical ensemble), but is open for exchanging particles with a surrounding bath. In this case, the chemical potential (μ) of the different species has a specified average, while the instantaneous value N of the number of particles can fluctuate. The Table 2.1 below shows the key ensembles.

An NVT ensemble was used for the molecular dynamics runs in this thesis to calculate both the surface and adsorption energies for pure and doped zirconia surfaces and a NPT was utilized for studying the bulk zirconia.

Table 2.1 Thermodynamic Ensembles

Ensemble Name	Conditions
Microcanonical (NVE)	Constant-(Number, Volume, Total Energy)
Canonical (NVT)	Constant-(Number, Volume, Temperature)
Isothermal-Isobaric (NPT)	Constant-(Number, Pressure, Temperature)
Grand Canonical (μvT)	Constant-(Chemical potential, Volume, Temperature)

To achieve a more realistic environment, the MD calculations also incorporate periodic boundary conditions. When carrying out these calculations for surfaces, at first the lattice vectors are oriented such that two vectors are parallel to the surface while the third one is perpendicular to the surface. The perpendicular vector enables to introduce a gap in to the crystal, which can be increased producing repeated crystal slabs. The void chosen is normally large enough to avoid the interaction between opposite surfaces. After the creation of the void, the system is minimised to relax the surfaces and the ensembles are chosen before the MD calculation begins. The choice of ensembles here are limited to NVE and NVT, since the application of pressure can cause the reformation of the bulk structure. In this thesis the molecular dynamics code DL_POLY [28] has been applied to study the bulk and surface structure of t-ZrO_2 in pure and doped conditions.

2.4.3 Radial Distribution Function

Radial distribution function (RDF) *g (r)* [16] is the probability of finding an atom at a distance *r* from a given particle. From the molecular dynamics simulation the RDF of a system can be calculated. Chapter 8 of this thesis provides the RDF analysis for both pure and WO_3 added t-ZrO_2. An RDF plot is constructed by counting the atoms surrounding the particle within a distance of *r* and *r+dr*. This could be viewed as consequent spheres around the specified particle, of which each sphere is separated from the other by a distance of *dr* as shown in Figure 2.11. MD simulation calculates the RDF by taking snapshots at regular intervals and calculating all pair distances between all pairs of atoms. The calculated pair distances along with the average number of atoms n(r) are placed in an average histogram.

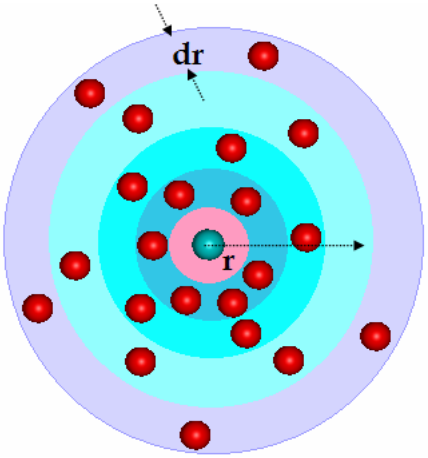

Figure 2.11 Spherical shells around the reference particle in Radial Distribution Function (RDF).

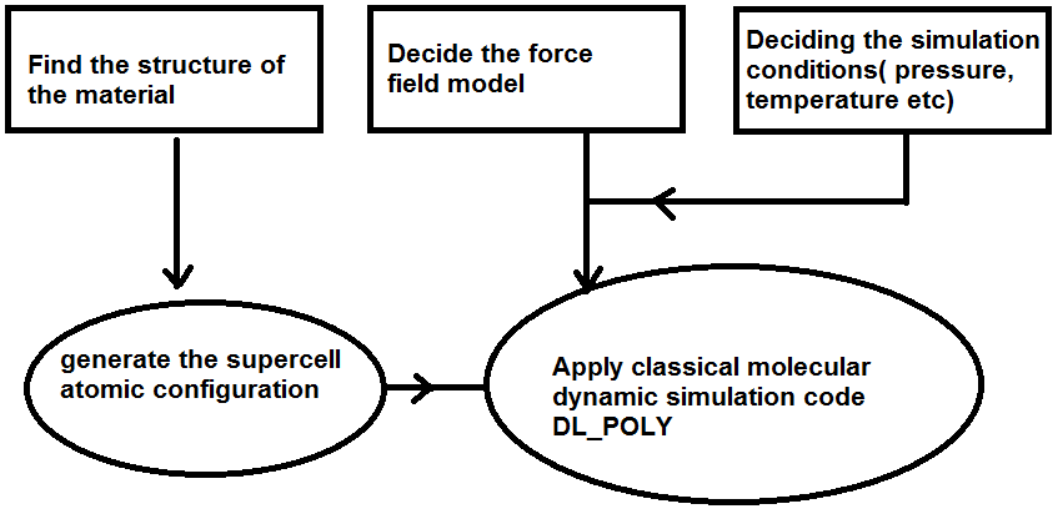

Figure 2.12 The Flow Chart of entire simulation work.

2.5 Conclusions

This chapter has provided an overview of the computational methods employed in this thesis. Although the different types of simulation codes used were described and a closer look at their theory was discussed, it is also important to understand the nature of the forces acting between atoms. These natures of the forces give us useful insight about the types of bonding between various atom pairs. At atomistic scale such forces are dominated by electrostatic interactions and for using them in simulation several models are developed to define these interactions, these are discussed in detail in the next chapter. The entire flow chart of the simulation is shown in Figure 2.12.

2.6 References

[1] J. D. Gale, *Philos. Mag.,* (1996) 73.
[2] J. D. Gale, *J. Chem. Soc. Faraday Trans.,* (1997) 93.
[3] G. W. Watson, E. T. Kelsey, N. H. de Leeuw, D. J. Harris, S. C. Parker, *J. Chem. Soc., Faraday Trans*., 92 (1996) 433.
[4] P. Atkins, *Physical chemistry, 6th edn. Freeman, New York* (1998).
[5] R. C. Evans, *An Introduction to Crystal Chemistry* (1964).
[6] T. Hahn, *International Tables for Crystallography, Volume A: Space Group Symmetry A, Berlin, New York* (2002).
[7] H. Brown, R. Bülow, J. Neubüser, H. Wondratschek, H. Zassenhaus, *Crystallographic groups of four-dimensional space, New York:* Wiley-Interscience (1978).
[8] N. Claussen, M. Rühle, A. H. Heuer, *Proc. 2nd Int'l Conf. on Science and Technology of Zirconia, Adv. Ceram.*, Vol. 11 (1984).
[9] C. R. A. Catlow, *Computer modelling in Inorganic Crystallography*. Academic Press Limited (1997).
[10] C. R. A. Catlow, E. Kotomin, *Comp. Mater. Sci.*, (2001).
[11] N. I. Levine, *Quantum Chemistry. Englewood Cliffs*, New Jersey: Prentice Hall. (1991) 455.
[12] M. Kilo, R. A. Jackson, G. Borchardty, *Philos.Mag*, 83 (2003) 3309.
[13] L. Minervini, M. O. Zacate, R. W. Grimes, *Solid State Ionics*, 116 (1999) 339.
[14] G. Balducci, M. S. Islam, H. Kašpar, P. Fornasiero and M. Graziani, *Chem. Mater*. 12 (2000) 677.
[15] T. X. T. Sayle, S. C. Parker and C. R. A. Catlow, *J. Phys. Chem*. 98 (1994) 13625.
[16] D. Chandler, *Introduction to Modern Statistical Mechanics*, Oxford University Press, (1987).
[17] P. E. Gill, W. Murray, M. H. Wright, *Practical Optimization*, London Academic, (1981).
[18] L. K. Nash, *Elements of Statistical Thermodynamics*, 2nd Ed. Dover Publications, Inc, (1974).
[19] P. E. Blöchl, *Phys. Rev. B*, 50 (1994) 17953.
[20] G. Kresse, D. Joubert, *Phys. Rev. B* 59 (1999) 1758.
[21] F. Jensen, *Introduction to Computational Chemistry*, Johnm Wiley & Sons, (2002).
[22] W. H. Press, S. A. Teukolsky, W. T. Vetterling, B. P. Flannery, *Numerical Recipes*, Cambridge University Press, Cambridge, 2nd edn., (1992).
[23] R. Fletcher, Practical *Methods of Optimisation*, Wiley,New York, (1980).
[24] H. J. Monkhorst, J. D. Pack, *Phys. Rev. B*, 13 (1976) 5188.
[25] R. J. D. Tilley, *Understanding Solids: The Science of Materials* (2012).
[26] P. W. Tasker, E. A. Colbourn, W. C. Mackrodt, *J. Am. Ceram. Soc*., 68 (1985) 74.
[27] W. Smith, T. R. Forester, *J. Mol. Graphics*, 14 (1996) 136.
[28] M.J. Ledoux, C. Phamhuu, *Catal.Today*., 15 (1992) 263.
[29] S. Chao, M.S. Wrighton, *J. Am. Chem. Soc*., 109 (1987) 5886.

[30] S.V. Filimonova, A.V. Nosov, M. Scheithauer, H. Knözinger, *J. Catal*., 198 (2001) 89.
[31] J.M. Grau, J.C. Yori, J.M. Parera, *Appl. Catal. A*, 213 (2001) 247.
[32] E. Iglesia, D.G. Barton, S.L. Soled, S. Miseo, J.E. Baumgartner, W.E. Gates, G.A. Fuentes, G.D. Meitzner, *Stud. Surf. Sci. Catal*., 101 (1996) 533.
[33] D. C. Whitley, *J. Math. Chem*., 23 (1998) 377.
[34] M. L. Connolly, *Network Science*, 2 (1996).
[35] S. Fleming, A. Rohl, *Z. Kristallogr*, 220 (2005) 580.
[36] B. K. P. Horn, *Proceedings of the IEEE*, 72 (1984) 1671.
[37] G. Wulff, *Z. Krystallogr. Miner.*, 34 (1901) 449.
[38] J. W. Gibbs, Longman: New York, 1928.
[39] J. Frenkel, *Z. Phys.*, 35 (1926) 652.
[40] F. A. Kröger, H. J. Vink, *in Solid State Physics*, 3 (1956) 307.
[41] W. Schottky, C. Wagner, *Z. Phys. Chem.*, 11 (1930) 335.
[42] W. Schottky, *Z. Phys. Chem.*, 29 (1935) 335.
[43] N. F. Mott, M. J. Littleton, *Trans. Faraday Soc*., 34 (1938) 485.
[44] P. W. Tasker, D. M. Duffy, *Surf. Sci.*,137 (1984) 91.
[45] B. J. Wain, T. E. Alderwright, *J.Chem. Phys*, 31 (1959) 459.
[46] B. J. Wain, T. E. Alderwright, *J.Chem. Phys*, 27 (1957) 1208.
[47] F. H. Stillinger, A. J. Rahman, *J.Chem. Phys*, 61 (1974) 4973
[48] L. Verlet, *Phys. Rev*., 156 (1967) 98.
[49] R. W. Hockney, *The potential calculation and some applications", Methods in Computational Physics*, Academic Press: New York (1970).
[50] P. W. Tasker, *A guide to MIDAS*. AERE Harwell Report R.9130, (1978)
[52] M. P. Allen, D. J. Tildesley, *Computer Simulation of Liquids*, Oxford University Press (1989).
[51] M. Cherkaoui, L. Capolungo, *Atomistic & Continuum Modelling of Nanocrystalline Materials*, (2009).
[52] R. Balescu, *Equilibrium & Nonequilibrium Statistical Mechanics*, A Wiley-Interscience Publication, New York (1975).

Chapter 3: The Potential Models

"*The existence of Intelligence in all creations is similar to a charge that polarises them through a spring attached to that Infinite CORE, the better the polarisability the higher is the Intelligence of that species.*"

— *Greeshma Nair*

3.1 Interatomic Potential Methods

This study utilises the simulation methods based on the Born Model of the ionic solid [1] employing interatomic potentials (IP) to describe the interactions between atoms. This model is chosen because it is relatively inexpensive, compared to QM methods but still gives atomistic detail making it better suited to modeling large scale systems. These methods find wide applications in elucidating the geometric structures and properties of periodic solid mostly ionic materials.

3.1.1 Born Model for Ionic Systems

The Born model of ionic solids is employed in this thesis, which assumes that the ions in the crystal interact *via* two types of forces. These are the long range electrostatic forces and the short-range forces, which include Pauli repulsions [2] and Van der Waals attractions [3] between electron charge clouds. The summation of these forces gives the potential energy function $U(r_1 \ldots r_N)$ of a particular system. The potential energy function

is the energy of an ensemble of N atoms as a function of the nuclear coordinate's $r_1 \ldots r_N$. Both the long range and short range interactions are described below in detail. Using this approach the lattice energy, U can be written in the form:

$$U(r_{i,j}) = \sum_{i}^{N} \sum_{\substack{j \\ j \neq i}}^{N} \frac{1}{4\pi \in_{\circ}} \frac{q_i q_j}{r_{ij}} + \sum_{i}^{N} \sum_{\substack{j \\ j \neq i}}^{N} \Phi_{i,j}(r_{i,j}) \qquad (3.1)$$

Here the first term describes the long range interactions and the second term defines the short range pair wise contributions. Both these interactions are discussed in detailed below.

3.1.1.1 Long Range Interactions

The interactions refer to the component of the lattice energy due to the electrostatic contributions from infinitely separated atoms being brought together. The corresponding potential energy of these long range interactions takes the form:

$$\Psi = \sum_{l_{i,j}}^{/} \frac{1}{4\pi \in_{\circ}} \frac{q_i q_j}{(r_{i,j} + l)} \qquad (3.2)$$

Where q_i and q_j are the charges on the ions i and j, $r_{i,j}$ is the displacement of ion i from ion j and l is the set of lattice vectors representing the periodicity of the crystal lattice. Although the Eq. (3.2) appears to be straightforward and simple, the sum converges poorly and therefore cannot be used directly to calculate the electrostatic energy in a simulation. Instead various methods have been developed to provide a quicker and reliable means of calculating the columbic energy. In this work two approaches have been used, Ewald [4] and Parry [5] summation, the choice of method depends on the type of system being considered. For three dimensional periodic systems Ewald's approach was utilised, while for two dimensional periodicity, Parry's method was utilised. Thus Ewald summation methods were successfully applied in calculating the bulk systems while Parry summations were used for calculating the surfaces using the two region approach but Ewald summation is used when working with slabs.

3.1.1.1.1 Ewald Summation

From the Eq. (3.2) it could be understood that the contribution to electrostatic potential energy due to the point-charges decays as 1/r, however, the number of interacting ions increases with the surface area of a sphere given by $4\pi r^2$. Hence, there is a faster increase in interaction energy compared to the rate the energy decays with increasing distance. Thus the convergence here is only conditional. So it can be understood from this that increasing the radius of the interacting spheres will not serve as a good method to evaluate the electrostatic energy in solids. Therefore in order to achieve a high degree of convergence an alternative procedure was first proposed by Paul Peter Ewald. [4] This

method, assumes that every particle i, with charge q_i, is surrounded by a diffused charge distribution of the opposite sign, such that the total charge of the cloud exactly cancels q_i. It can be expressed as the total sum of the real – space sum, the reciprocal or imaginary (Fourier) sum and the constant term known as the self-energy. At long distances, this fraction tends rapidly to 0 and the rate at which this occurs depends on the functional form of the screening charge distribution. The Gaussian distribution which describes the screening charge cloud is given by Eq. (3.3). This method which can sum the Coulombic interactions to infinity can transform the total Coulombic contribution into two convergent series, one in the real space and one in the reciprocal space, each of which converges rapidly. [7-8]

$$\rho_i = \exp\left(\frac{\left(r_i - r_{lattice}\right)}{\eta^2}\right)^2 \tag{3.3}$$

Where η is the half width of the Gaussian see Figure 3.1. Here the electrostatic potential at r_i can be easily computed from by direct summation, however the potential due to a set of screened charges is not of interest. This due to point charges and hence this screening cloud which has been applied to all particles must be corrected. In order to compute the electrostatic energy at the site of ion *i*, the electrostatic potential arising from the charge q_i must be excluded.

This idea is represented in Fourier series and at the end a correction for the inclusion of self-interaction of ion *i* and the compensating charge cloud is made as shown in Eq. (3.4).

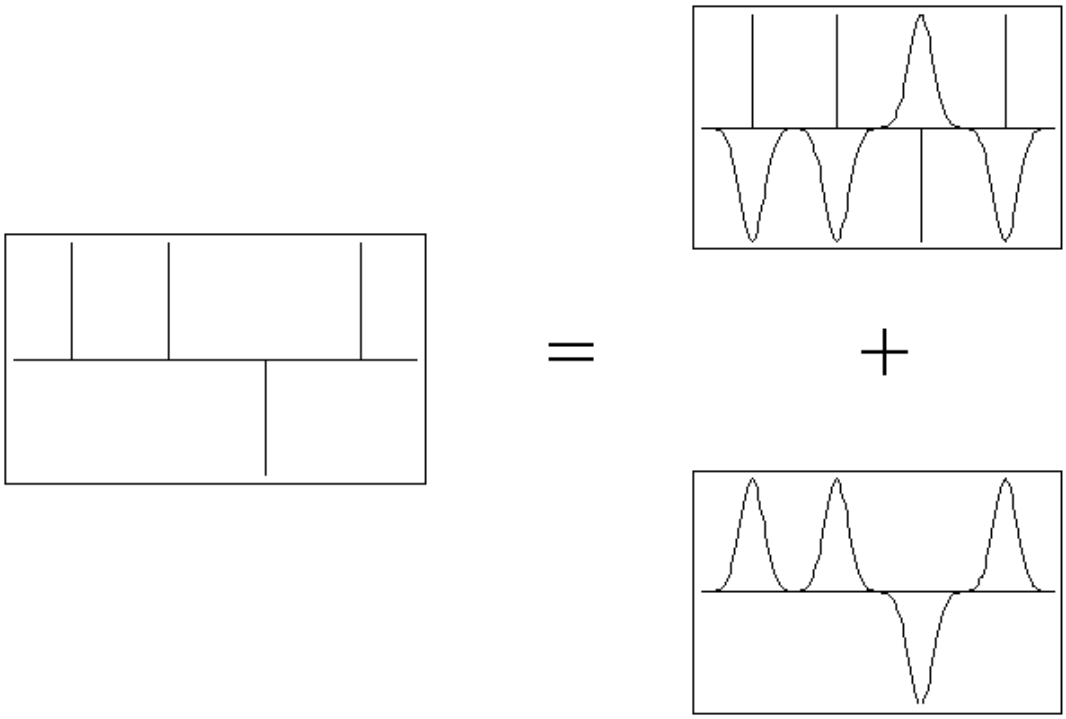

Figure 3.1 The point charges screening by Gaussian charge distribution.

$$\rho(r) = \left[\delta(r_i, r_{lattice}) - \exp\left(\frac{(r_i - r_{lattice})^2}{\eta^2} \right) \right] + \exp\left(\frac{(r_i - r_{lattice})^2}{\eta^2} \right) \qquad (3.4)$$

Where $\delta(r_i, r_{lattice})$ is the Direchelet delta function and becomes 1 if r_i represents the lattice site, else it becomes zero. The first term in this equation represents the interaction of the point charge with the Gaussian screening charge distribution solved in real space. The second term represents the compensating charge distribution solved by Fourier transforms. Finally the self-interaction term is removed by combining the potentials of

the first and the second terms and including an extra term to describe the self-interaction. The total equation for calculating the total columbic energy of the ion *i* is as follows:

$$\Psi_i = q_i \frac{q_i}{\pi V_k} \sum_{\substack{k \\ k \neq 0}} \left(\frac{\exp(-\pi^2 k^2 \eta^2) \exp(iK.R)}{k^2} \right) + q_i \sum_j \frac{q_i erfc(\eta r_i, j)}{r_i j} - \frac{2q_i^2 \eta}{\sqrt{\pi}} \qquad (3.5)$$

here *K* represents the reciprocal lattice vectors and *r* is $(r_i - r_{lattice})$ for all the ions in the unit cell. Ewald's approach to summing has been able to provide a high degree of accuracy to evaluation the energy of many inorganic materials and has been widely implemented.

3.1.1.1.2 Parry Summation

The Parry method [5, 6] is a modification of the Ewald method for a crystal periodic in two dimensions. Unlike the Ewald method of considering an infinite lattice, here the crystal is assumed to consist of a series of charged planes of infinite size. For the summation of the electrostatic interactions, the vectors are divided into in-plane vectors ρ_{ij} and vectors perpendicular to the plane u_{ij} and are given by:

$$\Psi = \frac{\pi}{A}\left\{ -2u_{i,j}erf\left(\eta u_{i,j}\right) - \frac{2\exp(-\eta^2 u_{i.j}^2)}{\sqrt{\pi\eta}} + \sum_{\substack{k \\ k\neq 0}} \frac{\exp(ikp_{i,j})}{k}\left[\exp\left(ku_{i,j}\right)erfc\left(\frac{k}{2\eta} - \eta u_{i,j}\right) + erf\left(-ku_{i,j}\right)erfc\left(\frac{k}{2\eta} - \eta u_{i,j}\right)\right] - \right\} \quad (3.6)$$

where erf(x) is the error function. This method too has been widely utilised for calculating the surface properties in solids.

3.1.1.2 Short Range Interactions

The short-range interactions are more complex in nature compared to the long range interactions. This is because they are composed of a combination of interactions. The interactions originate due to the overlapping of the electron clouds resulting in strong repulsive forces. These kind of repulsive forces prevent the crystal from collapsing in on itself. The van der Waals forces between neighbouring ions can also be included in these interactions and become significant when the separations between ions are increased. The van der Waals attraction, i.e. the attractive term, arises at close interatomic separations due to an induced-dipole interaction and covalence effects. [9, 10] It is also called the "London force" or dispersive interaction. Inclusion of other terms such as bond bending terms, which consider the interaction of three or more ions, could also be included here. Figure 3.2 represents the attractive and repulsive components as a function of ion separation in short range interactions.

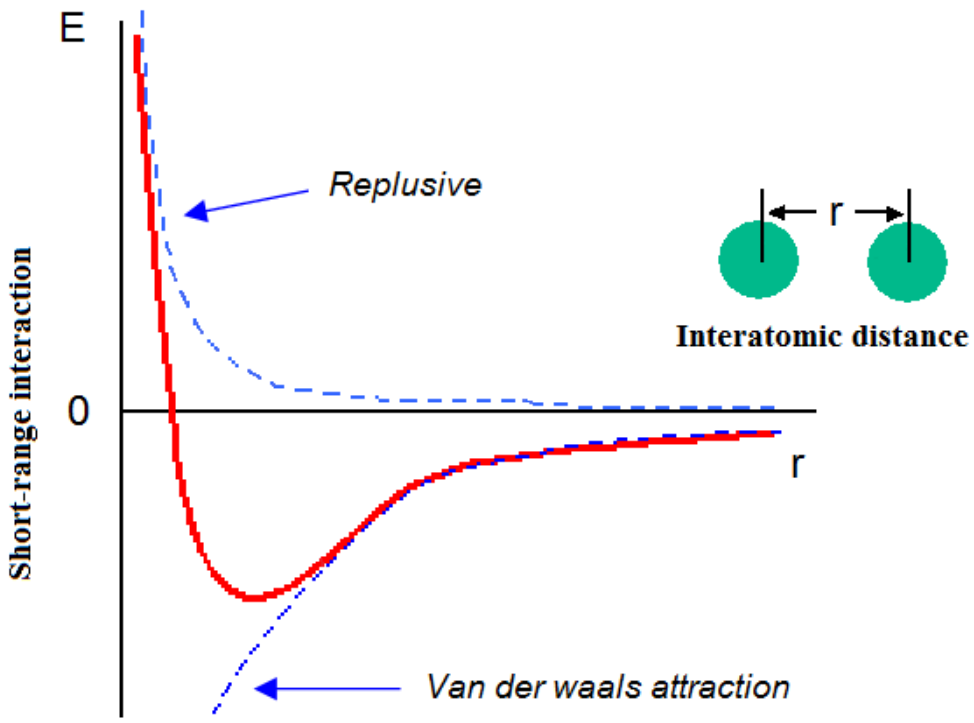

Figure 3.2 The non-Coulombic interaction including the attractive and repulsive components as a function of ion separation.

Some of the most commonly used potential models are discussed in the next section.

3.1.1.2.1 Lennard-Jones Potential

This form of the potential was first proposed in 1924 by John Lennard-Jones. [11] These are often used to model non-bonded interactions such as noble gases; however they were later applied to study the intermolecular interactions in molecular systems. [12] The most common way of expressing of the L-J potential is as follows:

$$\Phi_{i,j}\left(r_{i,j}\right)=\frac{A}{r_{i,j}^{12}}-\frac{B}{r_{i,j}^{6}}=E_0\left[\left(\frac{R_0}{r}\right)^{12}-2\left(\frac{R_0}{r}\right)^{6}\right] \qquad (3.7)$$

The r^{-12} term, is the repulsive term which describes Pauli repulsion at short ranges due to overlapping electron orbitals and the r^{-6} term, which is the attractive long-range term, describes attraction at long ranges (van der Waals force, or dispersion force). The equilibrium separation depends on the variable parameters A and B in the equation. An alternative method for defining the LJ potential is in terms of the coordinates of the minimum as shown in Figure 3.2 E_0 and R_0. This is also the form most often used when applying mixing rules. The limitation of this method is that since there are only two parameters involved in the equation, it can be only be fitted to a maximum of two physical quantities. However, the L-J potential gives relatively good approximation and due to its simplicity is often used to describe the properties of gases, and to model interactions in molecular models. The Lennard-Jones function is widely used by various

standard force fields codes such as CHARMM [15], DREIDING [16] , UFF [17] , AMBER [18] and OPLS [19].

3.1.1.2.2 The Buckingham Potential

This is one of the most frequently used functional forms for the short-range two body potential in ionic and semi ionic solids. [13] It is similar to the Lennard-Jones Potential; however an exponential is now used to describe the repulsive forces and takes the form.

$$\phi_{i,j}(r_{i,j}) = A_{i,j} \exp\left(\frac{-r_{i,j}}{\rho_{i,j}}\right) - \left(\frac{C_{i,j}}{r_{i,j}^{6}}\right) \qquad (3.8)$$

Where A_{ij} and ρ_{ij} describe components of the repulsive interaction and C_{ij} describes the attractive interaction. A_{ij} and ρ_{ij} relate to the number of electrons and the electron density respectively, while C_{ij} represents the van der Waals interaction. In the case where ions have small polarisabilities the C-term is often omitted giving rise to a Born-Mayer potential. The Buckingham potential is widely utilised to model many systems such as $CaCO_3$ [21], ThO_2 [22], CeO_2 [23], CaF_2, [24] $LiFePO_4$. [25] In this thesis we have

employed the Buckingham potential to study the short range interactions between the cation- oxygen and oxygen-oxygen. These were fitted empirically to reproduce the lattice parameters of t-ZrO_2. Although this method is suitable for many systems, they are not much suited to systems where strong localised bonds such as covalent bonds exist. In such situations additional intramolecular interactions to describe bond stretching and bond bending must be included.

3.1.1.3.3 The Morse Potential

This is a two body potential function developed by Philip Morse, [26, 27] generally used to describe bonding interactions. Here the energy is exponentially related to the interatomic spacing (r_{ij}) and the equilibrium distance (r_0). It is mainly used for interaction involving covalent bonding as it displays anharmonic behaviour. The Morse potential is described by the expression:

$$V(r_{i,j}) = A_{i,j}\,(1- \exp\,[-\,B_{ij}\,(r_{ij} - \phi_{ij})])^2 - A_{ij} \qquad (3.9)$$

where $A_{i,j}$ is the bond dissociation energy, $\phi_{i,j}$ is the equilibrium bond distance and $B_{i,j}$ is related to the curvature of the slope of the potential energy well and can be obtained from spectroscopic data. [28]

3.1.1.3.4 Three Body Potential

In the case of covalent materials the hybridization of the atoms may give rise to preferred bond directions, the so-called valence angle. The potentials described above will fail to accurately predict the properties in such conditions as any deviation from the in the equilibrium bond angles will cost energy and hence this should be described by an adequate potential. The changes in interaction energy caused by deviation from the equilibrium bond angle Θ_0, which is described as the angle between a central ion, i, and two adjoining ions j and k is modelled by a three body potential. The potential is described as shown below:

$$\phi_{i\,j\,k} = \frac{1}{2} K_{i\,j\,k} \left(\theta - \theta_0\right)^2 \tag{3.10}$$

where $K_{i,j,k}$ represents the harmonic force constant and μ is the bond angle. In the case of equilibrium bond angle Θ will become equal to Θ_0, which results in that entire expression getting reduced to zero.

3.2 Ionic Polarisability

The models discussed above only treat ions as point charges. In the case of complex oxides, the effects of defects present in them plays a major role in determining its properties. The electron cloud of an atom can get distorted by being influenced by defects or in the presence of electric field. This leads to the induction of a dipole in its electron cloud, affecting the short ranged interaction. Simple point dipole models are inadequate for modeling ionic crystals as they over estimate the polarization energy. Using the point polarisable model a simple description of ionic polarisability is as follows:

$$E = \mu\alpha \tag{3.11}$$

Where E represents the electric field, μ is the fixed dipole and α the ion polarisability. This type of model has been found to work well over a wide range of systems. [29-30] Even though this method has been capable to predict the properties of point ions and small molecules, the methods fail for larger systems. This failure is due to its inability to account for the coupling between the short-range interactions and the polarisation. An improved model was later developed in 1958 by Dick and Overhauser [31] and was called the Shell Model.

3.2.1 The Shell Model

In this model each ion is treated as a core and shell. The whole mass of the ion is in the core, which has a positive charge, and around the core there is a negatively charged massless shell. The core and the shell are connected via a harmonic spring as illustrated in Figure 3.3. The total charge of the ion is the sum of the core charge and the shell charge. The total interaction of the core and shell of an ion is given by:

$$\phi_i(r_i) = \frac{1}{2} k_i r_i^2 \qquad (3.12)$$

where r is the distance between the core and the shell and k is the spring constant. The polarisability (α) of the model ion is determined by the spring constant (k) and the shell charge (*Y*) and is represented as follows:

$$\alpha = \frac{Y^2}{4\pi \in_0 k_i} \qquad (3.13)$$

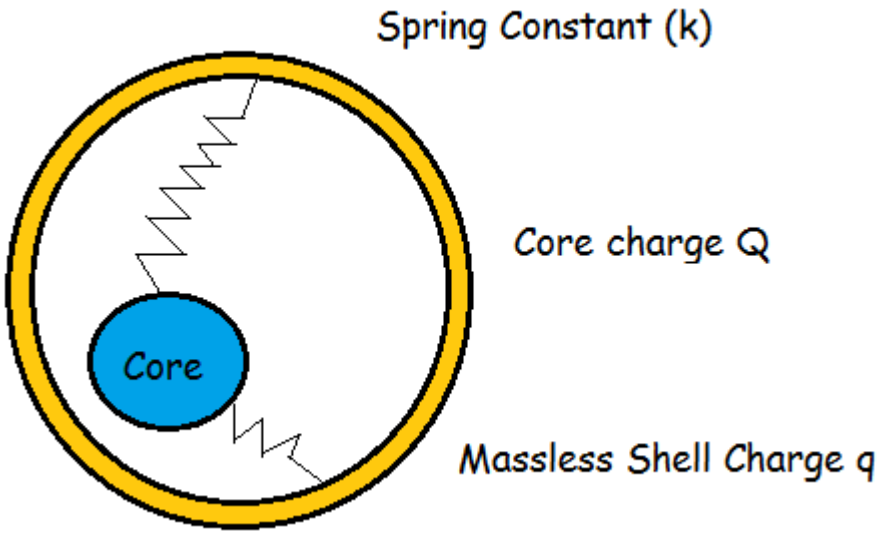

Figure 3.3 Schematic representation of the Core- Shell Model

There is an extension to this model known as the breathing shell model. [33] In this method the polarisability is capable of changing as it responds to changes in the ions environment. The computational cost of using either model is that the number of species involved in the computer simulation is doubled. The shell model is widely adapted and has accurately predicted the properties of various systems involving defects energies, phonon dispersion curves etc.

3.3 Potentials Used in this Work

This chapter discussed an overview of different potential methods commonly used in simulations. The Potential parameters used in this thesis to study the interactions in t-ZrO_2 were transferred directly from the previous study done by Grimes et. al [34] on t-ZrO_2. To evaluate the Phonon DOS and thermodynamic properties of t-ZrO_2, the Grimes potentials were not suitable due to the problem of the shell leaving the core; hence these studies in Chapter 4 utilised the Dwivedi and Cormack (1990) potentials. [35] To study the defect interactions occurring between various cations mentioned in Chapter 6, the potentials were used directly from the previous study done by Kilo et. al. [36] The potentials for Calcium ions used were developed by Dwivedi and Cormack (1990) [35], for Ceria by Minervini et al. (1999) [37], for Yittria by Lewis and Catlow (1985) [38] and for Niobium ions by Woodley *et al.* (1999) [39]. In order to model WO_3 groups on t-ZrO_2 described in Chapter 7, the potentials were used by the previous work done by Mairesse et. al. [40] Having established the theory and potential models applicable to carry out the study, the next chapter will begin to discuss the simulation studies on the structure of bulk t-ZrO_2. The potentials used in this study are tabulated below.

Table 3.1 Potential parameters used in the calculations: the Buckingham potential.

Species	*A* (eV)	ρ (Å)	*C* (eV Å^6)	References
Ca^{2+} -O^{2-}	1090.4	0.344	0.0	[35]
Ce^{4+} -O^{2-}	1809.68	0.354	20.40	[37]
Zr^{4+} -O^{2-}	1502.11	0.347	5.1	[34]
Zr^{4+} -O^{2-}	1024.6	0.376	0.0	[35]
Y^{3+} -O^{2-}	1325.6	0.3461	0.0	[38]
Nb^{5+} -O^{2-}	3023.18	0.300	0.0	[39]
W^{6+} -O^{2-}	767.43	0.438	0.0	[40]
O^{2-} -O^{2-}	9547.96	0.224	32.0	[34]
O^{2-} -O^{2-}	22764.0	0.149	27.89	[35]

Table 3.2 Potential parameters used in the calculations: the shell model.

Core-Shell Interactions			
Ion	**k/eV Å^{-2}**	**Y**	**Reference**
O_{core} - O_{shell}	6.3	-2.04	[34]
O_{core} - O_{shell}	27.29	-2.077	[35]

3.4 References

[1] M Born, K. Huang, Oxford (1954).
[2] L. Pauling, *The Nature of the Chemical Bond*, Cornell University Press, Ithaca, NY, (1960).
[3] F. Senese, *What are van der Waals forces*, Frostburg State University, (1999).
[4] P. P. Ewald, *Annalen der Physik*, 64 (1921) 253.
[5] D. E. Parry, *Surf. Sci.*, 49 (1975) 433.
[6] D. E. Parry, *Surf. Sci.*, 54 (1976) 195.
[7] C. Kittle, *Introduction to Solid State Physics*, 7th Ed, John Wiley & Sons, Inc., (1996).
[8] T. Darden, D. York, L. Pedersen, *J. Chem. Phys*., 98, 10089.
[9] F. London, *Z. Phys*., 63, 245, 1930.
[10] T. L. Hill, *J. Chem. Phys*., 16, 399, 1948.
[11] J. E. Lennard-Jones, *Proc. R. Soc*., Lond. A, 106 (1924) 463.
[12] Lennard-Jones, J. E. *Proc Phys Soc.*, 43 (1931) 461.
[13] R. A. Buckingham, *Proc. R. Soc. Lond. A*, 168 (1938) 264.
[14] W. Smith, T. R. Forester, *J. Mol. Graphics*, 14 (1996) 136.
[15] R. Brooks, R. E. Bruccoleri, B. D. Olafson, D. J. States, S. Swaminathan, M. Karplus, *J. Comput. Chem*., 4 (1983) 187.
[16] S. L. Mayo, B. D. Olafson, W. A. Goddard III, *J. Phys. Chem.*, 94 (1990) 8897.
[17] A. K. Rappe, C. J. Casewit, K. S. Colwell, W. A. Goddard III, W. M. Skiff, *J. Amer. Chem. Soc*., 114 (1992) 10024.
[18] W. D. Cornell, P. Cieplak, C. I. Bayly, I.R. Gould, K. M. Merz Jr., D. M. Ferguson, D. C. Spellmeyer, T. Fox, J.W. Caldwell, P. A. Kollman, *J. Am. Chem. Soc*., 117 (1995) 5179.
[19] W. Damm, A. Frontera, J. Tirado-Rives, and W. L. Jorgensen, *J. Comput. Chem*., 18 (1997) 1955.
[20] M. O. Zacate, L. Minervini, D. L. Bradfield, R. W. Grimes, K. E. Sickafus, *Solid State Ionics*, 128 (2000) 243.
[21] D. J. Cooke, R. J. Gray, K. K. Sand, S. L. S. Stipp, J. A. Elliott, *Langmuir*, 26 (2010) 14520.
[22] P. Martin, D. J. Cooke, R. Cywinski, *J. Appl. Phys*., 112 (2012) 073507.
[23] S. Vyas, R. W. Grimes, D. H. Gay, A. L. Rohl, *J. Chem. Soc., Faraday Trans*., 94 (1998) 427.
[24] Z. Zhao-Yi, C. Xiang-Rong, Z. Jun, H. Cui-E, *Chin. Phys. Lett.*, 25 (2008) 230.
[25] S. Islam, D. J. Driscoll, C. A. J. Fisher, P. R. Slater, *Chem. Mater*., 17 (2005) 5085.
[26] W. B. Shore, *J. Chem. Phys*., 59 (1973) 6450.
[27] P. M. Morse, *Phys. Rev.*, 34 (1929) 57.
[28] W. M. Haynes, D. R. Lide, T. J. Bruno, *CRC Handbook of Chemistry and Physics*, 87th ed, (2012).
[29] J. H. Harding, *Rep. Prog. Phys*., 53 (1990) 1403.
[30] G. W. Watson, S. C. Parker, A. Wall, *J. Phys. Condens. Matter*., 4 (1992) 2097.
[31] B. G. Dick; A. W. Overhauser, *Physical Review*, 112 (1958) 90.
[32] S. Sarkar, S. K. Chakrabati, Z. Physik B., 22 (1975) 309.

[33] W. Cochran, *Phonons in Perfect Lattices and in Lattices with Point Imperfections* ed R W H Stevenson: New York.
[34] S. E. Redfern, R. W. Grimes, R. D. Rawlings, *J. Mater. Chem*., 11 (2001) 449.
[35] A. Dwivedi, A., A. N. Cormack, A. N., *Philos. Mag. A*, 61 (1990) 1.
[36] M. Kilo, R. Jackson, G. Borchard, *Philos. Mag*., 83 (2003) 3309.
[37] L. Minervini, M. O. Zacate, R. W. Grimes, *Solid St. Ionics*, 116 (1999) 339.
[38] G. V. Lewis, G. V., C. R. A. Catlow, *J. Phys., C*, 18 (1985) 1149.
[39] S. M. Woodley, P. D. Battle, J. D. Gale, C. R. A. Catlow, *Phys. Chem.Chem. Phys*., 1 (1999) 2535.
[40] C. Pirovano, M. S. Islam, R. Vannier, G. Nowogrocki, G. Mairesse, *Solid State Ionics*, 140 (2001) 115.

Chapter 4 Bulk Structures of Pure t-ZrO_2

"Nothing that I can do will change the structure of the universe. But maybe, by raising my voice I can help the greatest of all causes - goodwill among men and peace on earth."

— *Albert Einstein*

4.1 Introduction

Zirconia is a polymorphic metal oxide, displaying various phases at various temperatures. In its natural form it is known as baddeleyite which has a monoclinic crystalline structure and was first described in 1892 and named after Joseph Baddley. [1] The three low pressure phases of zirconia includes cubic (c-ZrO_2, Fm-3m), tetragonal (t-ZrO_2, $P4_2$ /nmc), and monoclinic (m- ZrO_2, $P2_1/c$) structures. [2, 3] All these structures have great scientific and technological importance. At ambient pressure, ZrO_2 has a monoclinic structure, at temperatures above ~1450 K, the monoclinic phase transforms to the tetragonal phase. This transition is accompanied by a decrease in unit cell volume since the 7-fold coordination of zirconium cations (Zr^{4+}) changes to 8-fold. The tetragonal form is usually stable until ~ 2370K after which it transforms to the cubic form. This thesis attempts to study the properties of the tetragonal phase of zirconia. Tetragonal ZrO_2 (t-ZrO_2) is widely applied as a catalyst/catalyst support for various gas-phase reactions. [4, 5] A great deal of experimental analysis has been carried out in zirconia materials. This includes the use of Auger-photoelectron spectroscopy, vibrational spectroscopy as well as electron microscopy and X-ray diffraction studies. [6-14] However due to the structural

complexity of this material, less theoretical work on t-ZrO_2 has appeared in the literature than the cubic polymorph. The bulk properties of t-ZrO_2 have been examined using density functional methods [15-17], semi empirical modelling combined with *ab initio* techniques in the past [17-21] This chapter presents the results of the properties of bulk t-ZrO_2 and also the influence of higher temperatures on the structural stability. We use static energy minimization techniques to relax the t-ZrO_2 structure and then do a constant pressure minimisation using molecular dynamics (DL_POLY 2.14 package [22]). The accuracy of the computed data are compared with experimental and previous theoretical results; enabling us to evaluate the reliability of this model to predict the accurate structure.

4.2 Simulation of pure bulk t-ZrO_2

There exists a large body of experimental and theoretical results for t-ZrO_2 properties at ambient conditions; however, care was taken in selecting the structure that can be used to validate the theoretical results. The tetragonal modification of ZrO_2 selected here has a space group of 137, ($P4_2/nmc$), where each zirconium atom is surrounded by eight oxygen atoms. [23] The starting point for this work was the experimentally determined structure by G. Teufer, [23] which has lattice parameters of $a = b = 3.64$ Å & $c = 5.27$ Å.

The Buckingham potential model were developed by Grimes [24] and co-workers and described in Table 3.2 of Chapter 3. These were used in to the static simulation code

(METADISE [25]) and the energy minimisation was carried out. A constant pressure minimisation (*CONP*) was utilised for reasons mentioned in section 2.3.1 of Chapter 2. In the tetragonal phase, the zirconium atom is located on the Wyckoff position 2a (0 0 0) and the oxygen atom is located on the Wyckoff position 4d (0 0.5 0.185). The oxygen atoms are displaced along the z-direction and the oxygen columns are shifted up and down by a certain amount. This arrangement in t-ZrO_2 is normally referred as a body centered tetragonal (*bct*) pseudo fluorite structure. [26] The variation of tetragonal structure from its cubic fluorite phase is represented by two parameters known as "*A*" and "*dz*".[27] the tetragonal distortion of the cell parameters are represented by $A = \frac{c}{a\sqrt{2}}$ and the internal distortion parameter $dz = \frac{\Delta Z}{C}$, where ΔZ is the difference in the z-coordinate of the oxygen atom in the tetragonal structure see Figure 4.1. For the cubic phase $A = 1$ and $dz = 0$, while for tetragonal phase, the earlier experimental evidences [23, 27-30] have suggested the values of dz to lie between 0.041 to 0.065 and hence the computed values of our dz in t-ZrO_2 should be close to these values to begin this study with the right structure.

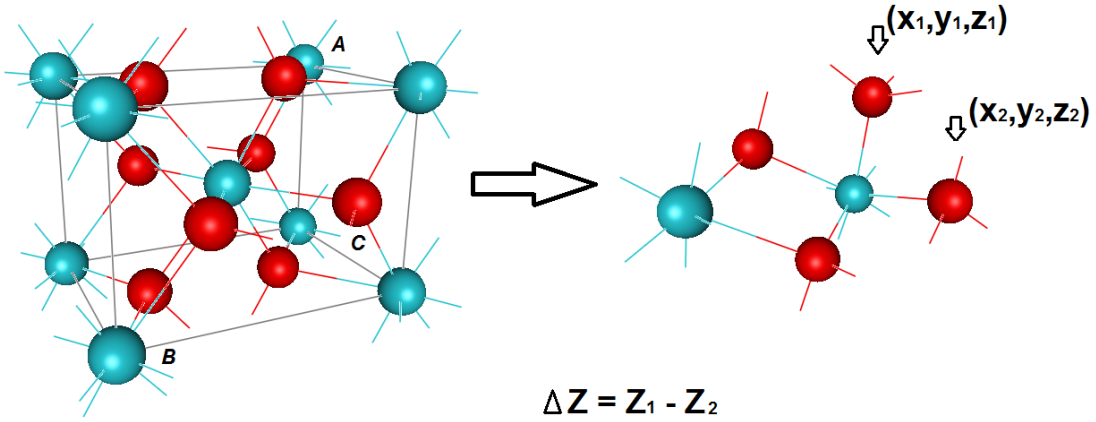

Figure 4.1 The graphical representation of the ΔZ parameter in t-ZrO_2. Zirconium atoms are shown in blue and Oxygen in red.

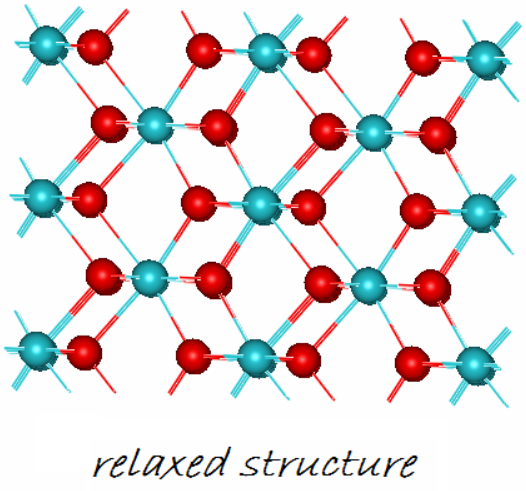

Figure 4.2 Structural relaxations in t-ZrO_2 using static simulations.

Table 4.1 Calculated and observed interatomic distances for t-ZrO_2

Parameters	***r* (Å) (expt.)** *Reference [29,30]*	***r* (Å) (DFT - studies)** *Reference [28]*	***r* (Å) (calc.) (METADISE)**	***r* (Å) (calc.) (METADISE)** *(c= 5.23 Å parameter values)*
Zr ……O_I	2.06	2.07	2.21	2.13
Zr …….O_{II}	2.46	2.33	2.21	2.33
O_I …….O_{II}	2.63	-	2.56	2.57
Zr …….Zr	3.68	-	3.62	3.65
a* = *b	3.60	3.57	3.61	3.61

c	5.27	5.12	5.11	5.23
A = $\frac{c}{a\sqrt{2}}$	1.032	1.0166	0.99	1.024
Internal distortion (d_Z)	0.065	0.0441	-	0.063
$\alpha = \beta = \gamma$	90	90	90	90
Lattice Energy Per ZrO_2 (eV)	-	-	-111.11 eV	-111.08 eV

The Figure 4.2 shows the relaxed structure of t-ZrO_2 represented by the static simulation techniques using the METADISE code. The structural relaxations indicate that the distance between the zirconium and it's nearest neighbour oxygen atom (O_I) and the next nearest neighbouring oxygen atom (O_{II}) to be equal to 2.21 Å. However, the earlier experimental and DFT work [28-30] have reported an increase in values for the zirconium

bound to the next nearest neighbouring oxygen atom. Although an overall matching was found with the computed results, it was not possible to compute the *dz* parameter with our results. It was noted that the variation in "*c*" parameter caused an error in computing the *dz* parameter. Since the tetragonal phase is a high temperature polymorph, the effects of temperature on the lattice parameters must be included. This effect is included by performing a series of molecular dynamics simulations using DL_POLY 2.14 package. [28] In this simulation, an isothermal-isobaric ensemble (NPT) was used, where N represents the number of particles, P the pressure and T, the temperature. They are all kept constant using the Nosé-Hoover thermostat, [31, 32] within the Verlet-Leapfrog algorithm, [33] which are used to generate the trajectories. The simulation was monitored using the VMD analysis software, [34] from which the structural changes occurring at different time steps could be recorded.

4.3 Molecular Dynamics

The simulation box consisted of 392 zirconium atoms and 784 oxygen atoms in a 7x7x4 supercell and the simulation was carried out using periodic boundary conditions. The macroscopic computational sample of t-ZrO_2 is thus formed by a periodical replication in all directions as shown in Figure 4.3. The simulation also needs a proper definition of the thermodynamic state of a molecular system. A collection of these points are known as thermodynamic ensembles described in detail in section 2.4.2 of Chapter 2. These ensembles are described properly in the CONTROL file. In this study a cut-off radius of

10 Å was used and it was run using an NPT ensemble. At the start of the simulation the temperature is gradually scaled to achieve the desire temperature. To maintain the heat exchange between the system and surroundings, thermostats are used. [48, 49] In this study the system was equilibrated at 300 K, at zero pressure, maintained via a Nose-Hoover thermostat and barostat respectively. The use of this treats the system as being in contact with a constant temperature bath.

The shake algorithm [35, 36] was used to constrain the intermolecular degrees of freedom. The equations of motion were integration using a leapfrog algorithm. Each simulation was run for a time step of 0.1 femto second and the stat file was recorded at every 250 steps. 1 million steps were used to run for 0.1 femto second and the job time was 60,000 sec, these steps were enough to allow structural relaxation in order to find the equilibrium lattice parameters. The Grimes potential parameters were incorporated in the FIELD file of the DL_POLY code. After the finish of the MD run, the average values of lattice parameters were estimated. MD runs were further repeated under similar NPT conditions for higher temperatures to evaluate the structural changes occurring at high temperatures. The temperatures were increased from 300 K till 2000 K.

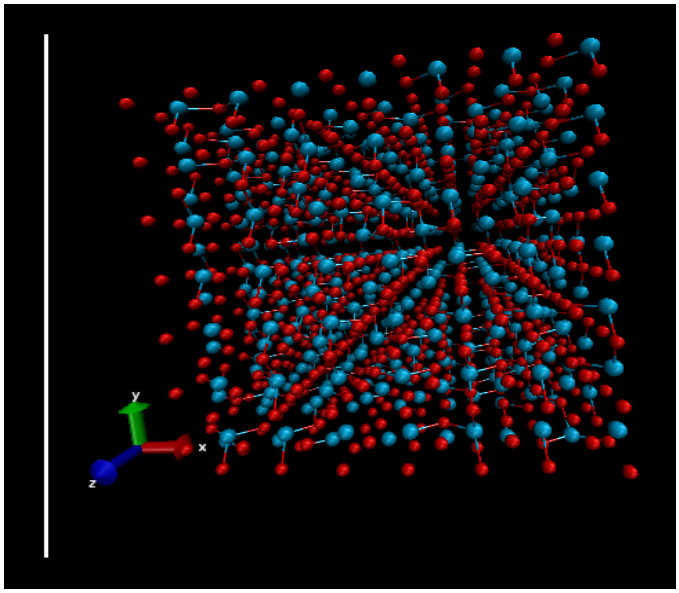

Figure 4.3 Periodic boundary conditions in MD simulation (perspective view generated using VMD software), Zirconium atoms shown in blue and Oxygen in red.

The snapshots were taken from the MD runs using VMD software at various time steps as shown in Figure 4.4. At higher temperatures, an increase in length for Zr-O bond was observed, this increase was estimated to be approximately 1-2 %. The lattice parameters a and c exhibited gradual and linear increase with temperature as shown in Figure 4.5 (a) and (b). However, the tetragonal distortion parameter *"A"* remained at a constant value throughout this temperature range as shown in Figure 4.6. Therefore it is evident that the structure still maintained its tetragonal phase without undergoing any transition to other polymorphic forms. This ensures the thermal stability of the optimised structure. The

equilibrated values of a parameter were 3.61 Å and that for c was 5.23 Å. The final relaxed structure from the MD run indicates that each zirconium atom is surrounded by eight oxygen atoms, having four long Zr-O bonds, with bond lengths ranging between 2.33 Å - 2.45 Å and four short Zr-O bonds of 2.09 Å - 2.13 Å. Using the values of the *c*-parameter from the molecular dynamics run, the tetragonal distortion parameter "*A*" was computed to be 1.024 and the dz parameter 0.063, which is in very good agreement with the experimentally reported values of 0.065 see Table 4.2. We therefore have rightly optimised the structure to extend our analysis on t-ZrO_2.

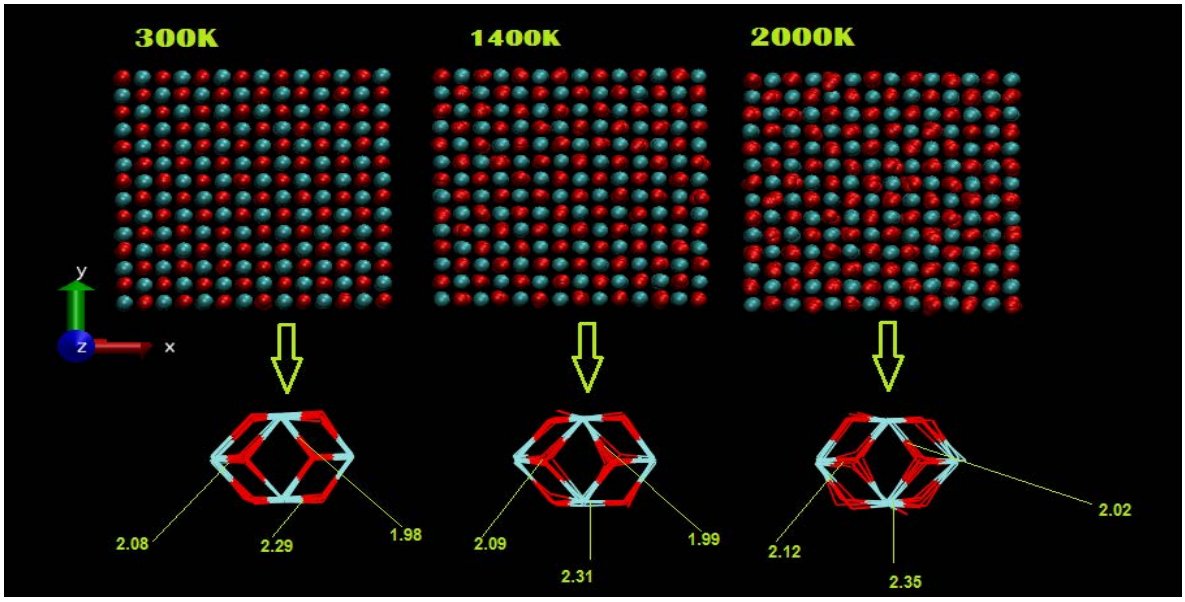

Figure 4.4 Snapshots of MD simulation runs at various temperatures using VMD analysis software, the bond distance shown are in Angstrom.

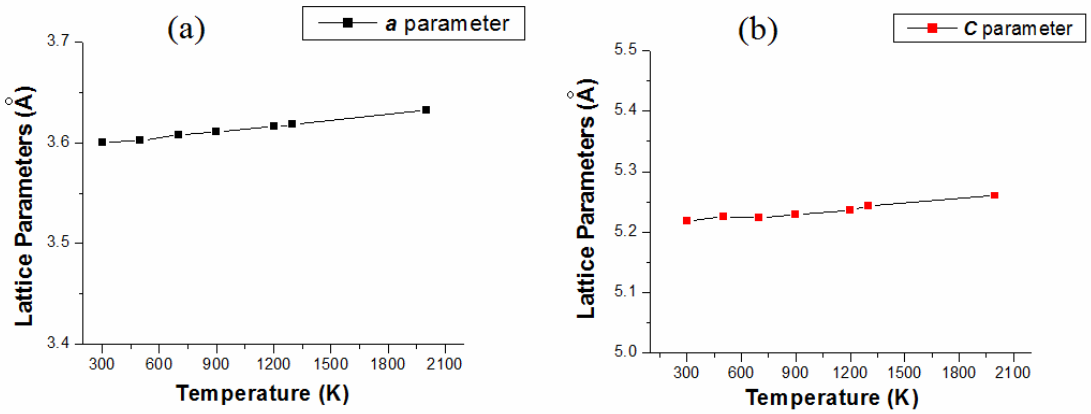

Figure 4.5 The plot of lattice parameters versus increasing temperatures. (a) the "a" parameter values (b) the "c" parameter values.

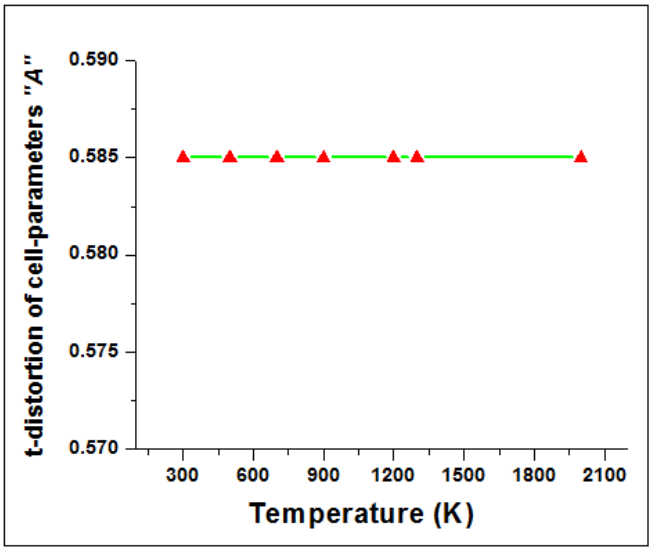

Figure 4.6 The plot of tetragonal distortion parameter ("A") versus temperature.

4.4 Phonon Density of States

The thermodynamic properties of a crystal are directly related to its phonon structure. [37] Understanding the phonon modes is important to predict the thermodynamic behaviour of the crystal. Hence, the next part of the study was to identify the phonon density of states for t-ZrO_2. Experimentally there are only two ways to determine the phonon density of states 1) Raman spectra and 2) Neutron scattering. [38] The Raman spectra give us the information on the zone centre phonons, while neutron scattering gives useful information about the phonon modes. However, probing the phonon modes across the entire Brillouin zone is extremely difficult even when using neutron scattering. Using modelling techniques, all the total number phonons modes can be estimated. The symmetry of the crystal determines which of the phonons will become Raman active. In order to be Raman active, the first derivation of the polarisability with respect to its vibrational coordinate should be non-zero.

The group theory from previous studies, report 18 phonon branches for t-ZrO_2, out of which there are around six observed optical modes of Raman spectra. [39] The important ones for t-ZrO_2 are computed and are compared with the experimental results. To do this, a 1x1x1 unit cell of t-ZrO_2 was simulated using the lattice dynamic simulations implemented in the GULP code. [40]

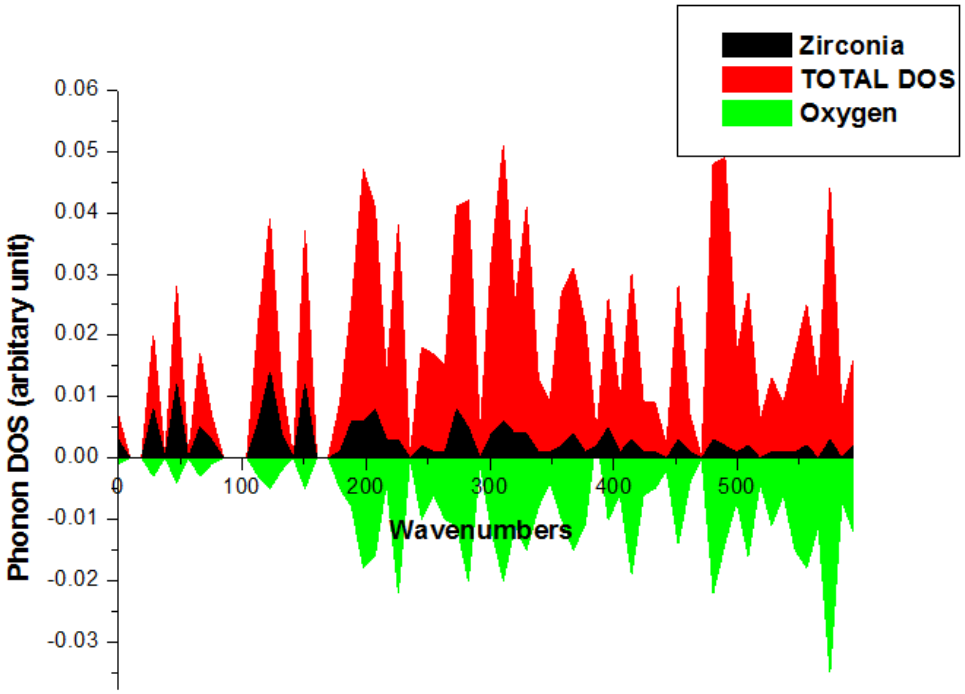

Figure 4.7 The Partial and Total Phonon Density of States at 300 K for t-ZrO_2 calculated using GULP code.

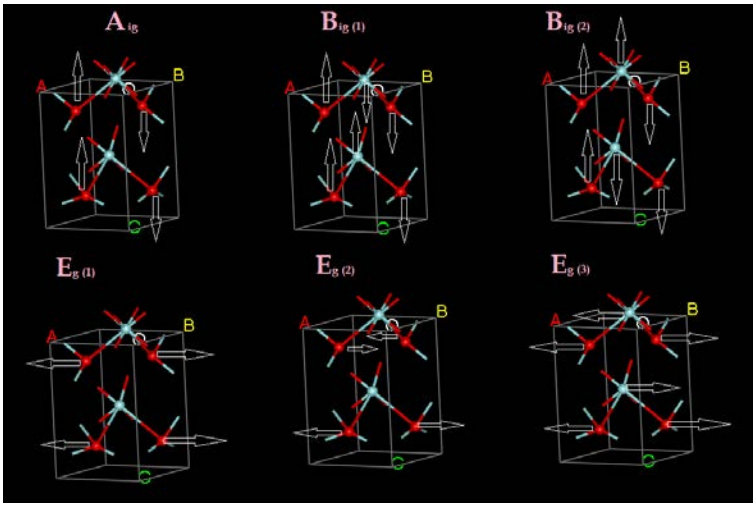

Figure 4.8 The Raman active vibrations occurring in the crystal lattice of t-ZrO_2 (reproduced from Reference [39])

When the Grimes potential [24] were used in this study, the shell left the core at higher temperatures, hence the Dwivedi and Cormack (1990) potentials described in Chapter 3 were utilized. Evaluating the phonon density of states (DOS) at 300 K noted a large number of sharp phonon peaks as shown in Figure 4.7. This sharpness in the peaks was due to the fact that many of the phonon branches had low dispersion. Analysing the nature of the participation of the zirconium and oxygen in these phonon modes, it could inferred here that zirconium tends towards the lower energy end of the DOS. The majority of the DOS was dominated by the lighter oxygen. The DOS of oxygen in Figure 4.7 is plotted on the negative axis for clarity and comparison.

The previous literature [39] on Raman spectra suggests that there are few fundamental phonon modes for t-ZrO_2. Depending on the type of sample the band intensity may vary, but the characteristic peaks help us to identify the phases present in the crystals. The Raman active modes for t-ZrO_2 are designated as A_{1g}, B_{2g} and E_{3g} shown in Figure 4.8. The values of each of these Raman active modes were estimated from the GULP calculations and compared with the previous literature reports. The values in Table 4.2 indicate that a good matching of results was achieved with the computed Phonon DOS values in comparison with the previous DFT and experimental studies.

Table 4.2 Comparison of Phonon frequencies at 300 K obtained by GULP and other reported methods

Raman active Modes	**Phonon Frequencies using GULP** cm^{-1} this work	**Phonon Frequencies using GGA** cm^{-1} *Reference* [39]	**Phonon Frequencies using LDA** cm^{-1} *Reference* [39]	**Phonon Frequencies Experimental** cm^{-1} *Reference*[39]
$\mathbf{E_{1g}}$	151	126	146	150
$\mathbf{A_{1g}}$	280	286	270	262
$\mathbf{B_{1g}}$	310	290	330	328
$\mathbf{E_{1g}}$	452	411	473	470
$\mathbf{B_{1g}}$	574	569	607	609
$\mathbf{E_{1g}}$	593	625	659	643

4.5 Thermodynamic properties of t-ZrO_2

In order to understand the crystal behaviour at higher temperatures, lattice dynamic simulations were performed and the specific heat (C_v) against the temperature was plotted. The heat capacity of a substance is very important in terms of its application; hence an idea of zirconia's thermodynamic behaviour can be evaluated exploring this property. The Figure 4.9 indicates that at lower temperatures C_v is directly proportional to temperature while at higher temperatures, the specific heat capacity slowly approaches a constant value. This indicates that the crystal clearly follows the Debye law. The results are in agreement with the previous experimental results of t-ZrO_2. [41-44] The specific heat capacity evaluated from the lattice dynamic calculations were estimated to 73.5 J/ mol K. To compare these values with the earlier MD calculations done using Grimes potential, the enthalpy obtained from the these calculations were plotted against the temperature as shown in Figure 4.10. The slope of the straight line in the plot gave the specific heat capacity which was found to be 77 J/ mol K, this indicates that only less than 5 % deviation from the values estimated from the lattice dynamic calculations. From the specific heat plot (Figure 4.9 (a)), it is also easy to determine the Debye temperature Θ, which is the temperature below which the quantum effects in a crystal are more important in understanding the thermodynamic properties. In this temperature range, the vibrations within the crystal behave according to the Dulong-Petit Law and the heat capacity is 3Nk and the quantum effects can be neglected. Debye temperature is an important parameter, which is related to many physical properties of crystals.

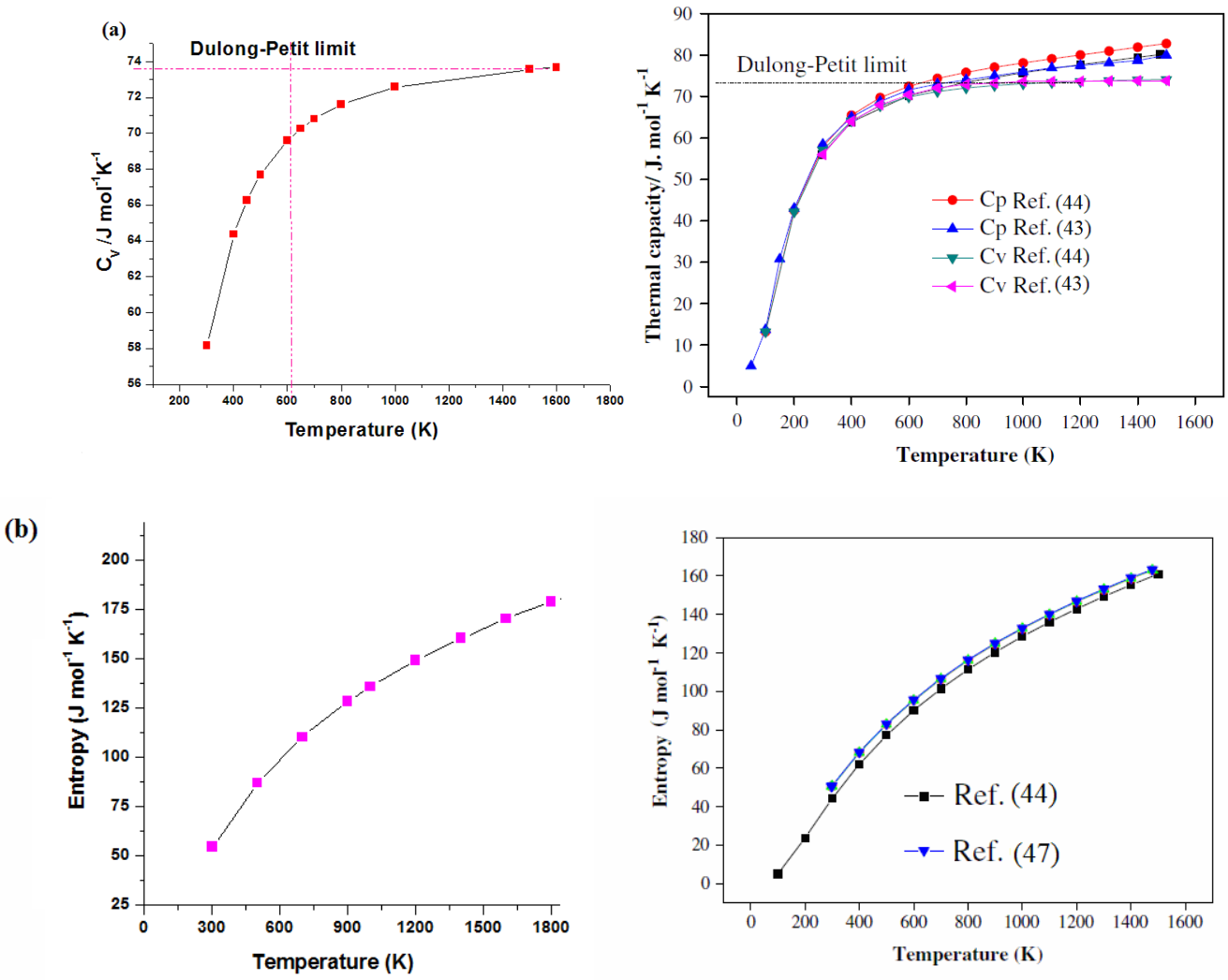

Figure 4.9 (a) The plot of specific heat versus temperature, the horizontal dotted line represents the Dulong-Petit limit and the vertical dotted line represents the estimation of Debye temperature (Θ) from the plot, left side: lattice dynamic and right side:previous references (b) The plot of entropy versus temperature. left side: lattice dynamics and right side: previous references.

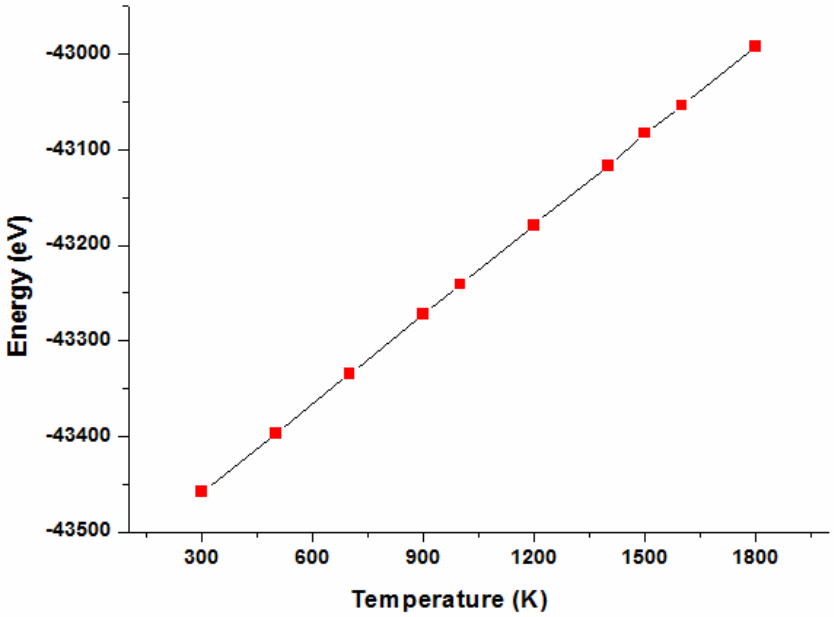

Figure 4.10 The plot of enthalpy versus temperature from the molecular dynamics run.

The Debye temperature for t-ZrO_2 estimated from Figure 4.9(a) is approximately 620 K, which is close to the previously study reported values of 590 ± 20 K. [41] Similarly the variation of vibrational entropy with increasing temperature shown in Figure 4.9(b), was also in good agreement with the previous computational work. [44, 47]

4.6 Conclusions

A successful modelling of the bulk tetragonal phase of zirconia was achieved using the simulation studies mentioned in this chapter. These results were also in agreement with the previous experimental and computational results. The maintenance of a constant value for tetragonal distortion parameter suggested the stability of this computed structure to maintain its tetragonal phase even at higher temperatures. The phonon studies indicated the dominance of lighter oxygen's over zirconium in the DOS profiles. The frequencies for the Raman active modes obtained by phonon studies were in close agreement to the previous experimental and theoretical studies. The predicted values of thermodynamic entities were also found to be agreeable with the previously reported work. The crystal clearly follows the Debye law and their plateaus reach the Dulong-Petite limit. Although the bulk structures have been correctly optimized, the important parameters that dominate the stability and catalytic properties are located on the surfaces of the crystal. A closer look at the phenomena occurring at the surfaces will give us an idea about the factors that influence the catalytic properties of this material. This motivates to explore us the next part of the investigation, where the surface structures of t-ZrO_2 will be analysed.

4.7 References

[1] S. A. Heimstra, *Amer. Mineral*., 40 (1955) 275.
[2] E. V. Stefanovich, A. L. Shluger, C. R. A. Catlow, *Phys. Rev. B*, 49 (1994) 11560.
[3] O. Ohtaka, T. Yamanaka, S. Kume, E. Ito, A. Navrotsky, *J. Am. Ceram. Soc*.,74 (1991) 505.
[4] M. Haruta, T Kobayashi, H. Sano, N. Yamada, *Chem. Lett*., 829 (1987) 405.
[5] A. Knell, P. Barnickel, A. Baiker, A. Wokaun. *J. Catal*., 137 (1992) 306.
[6] K. O. Axelsson, K.-E. Keck, B. Kasemo, *Appl. Surf. Sci*., 25 (1986) 217.
[7] I. Birkby, P. Harrison, R. Stevens, *J. Eur. Ceram. Soc*., 5 (1989) 37.
[8] D. Majumdar, D. Chatterjee, *Thin Solid Films*, 206 (1991) 349.
[9] N. K. Huang, *J. Mater. Sci. Lett*., 11 (1992) 681.
[10] G. S. A. M. Theunissen, A. J. A. Winnubst, A. J. Burggraaf, *J. Mater. Sci*., 27 (1992) 5057.
[11] C. Morterra, G. Cerrato, L. Ferroni, A. Negro, L. Montanaro, *Appl. Surf. Sci*., 65/66 (1993) 257.
[12] C. Morterra, G. Cerrato, L. Ferroni, L. Montanaro, *Mater. Chem. Phys*., 37 (1994) 243.
[13] L. E. Depero, R. Bertoncello, T. Boni, P. Levrangi, I. Natali Sora, E. Tempesti, F. Parmigiani, *J. Mater. Res.*, 12 (1997) 1376.
[14] G. Cerrato, S. Bordiga, S. Barbera, and C. Morterra, *Surf. Sci*., 50 (1997) 377.
[15] N. I. Medvedeva, V. P. Zhukov, M. Ya. Khodos, V. A. Gubanov, *Phys. Status Solidi B*, 160 (1990) 517.
[16] H. J. F. Jansen, *Phys. Rev. B, 43* (1991) 7267.
[17] R. H. French, S. J. Glass, F. S. Ohuchi, Y.-N. Xu, W. Y. Ching, *Phys. Rev. B*, 49 (1994) 5133.
[18] L. Soriano, M. Abbate, J. Faber, C. Morant, J. M. Sanz, *Solid State Commun.*, 93 (1995) 659.
[19] L. L. Boyer, B. M. Klein, *J. Am. Ceram. Soc*., 68 (1985) 278.
[20] E. V. Stefanovich, A. L. Shluger, C. R. A. Catlow, *Phys. Rev. B*, 49 (1994) 11560.
[21] M. Wilson, U. Schoberger, M. Finnis, *Phys. Rev. B*, 54 (1996) 9147.
[22] W. Smith, T.R. Forester, *J. Mol. Graphics*, 14 (1996) 136.
[23] G. Teufer, *Acta. Cryst*., 15 (1962) 1187.
[24] E. Redfern, R. W. Grimes, R. D. Rawlings, *J. Mater. Chem*., 11 (2001) 449.
[25] G.W. Watson, E.T. Kelsey, N.H. De Leeuw, D.J. Harris, S.C. Parker, *J. Chem.Soc*., 92 (1996) 433.
[26] E. C. Subbarao, H. S. Maiti, K. K. Srivastava, *Physica status solidi*, 21 (1974) 9.
[27] A. Christensen, E. A. Carter, *Phys. Rev. B*, 58 (1998) 8050.
[28] V. Milman, A. Perlov, K. Refson, S. J. Clark, J. Gavartin, B. Winkler, *J. Phys.: Condens. Matter*, 21 (2009) 485404.
[29] JCPDS pattern No. 42-1164
[30] R. Orlando, C. Pisani, C. Roetti, *Phys. Rev. B*, 45 (1992) 592.
[31] S. Nosé, *J. Chem. Phys*., 81 (1984) 511.
[32] W.G. Hoover, *Phys. Rev. A*, 31 (1985) 1695.
[33] L. Verlet, *Phys. Rev*., 156 (1967) 98.

[34] W. Humphrey, A. Dalke, K. Schulten, *J. Mol. Graph*., 14 (1996) 33.
[35] J. P., Ryckaert, G., Ciccotti, H. J. C., Berendsen, *J. Comput. Phys*., 23 (1977) 327.
[36] W. Smith, T. R. Forester, *Comput. Phys. Commun*., 79 (1994) 63.
[37] L. F. Lou, *Introduction to phonons and electrons*, (2003).
[38] P. P. Yu, *Fundamentals of Semiconductors: Physics & Materials Properties*, (2010).
[39] A. P. Naumenko, N. I. Berezovska, M. M. Biliy, O. V. Shevchenko, *J. Phys. Chem. Solids*, 9 (2008) 121.
[40] J. D. Gale, J. Chem. Soc., Faraday Trans. 93 (4), 629, 1997.
[41] C. Degueldre, P. Tissot, H. Lartigue, M. Pouchon, *Thermochim. Acta,* 403 (2003) 267.
[42] H. Inaba, *Int. J. Thermophys*., 21 (2000) 263.
[43] A. T. Petit, P. L. Dulong, *Ann. Chim. Phys*., 10 (1819) 95.
[44] L. Jin, L. Ni, Q. Yu, A. Rauf, C. Zhou, *Comp. Mater. Sci*., 65 (2012) 170.
[45] I. Barin, Beijing, *Science Press*, (2003) 1023.
[46] C. Wang, M. Zinkevich, F. Aldinger, *Calphad*, 28 (2004) 281.
[47] P. Liang, N. Dupin, S. G. Fries, H. J. Seifert, I. Ansara, H. L. Lukas, F. Aldinger, *Z. Metallkd*. 92 (2001) 747.

Chapter 5. Pure Surfaces of t-ZrO_2

"It is not the strongest of the species that survives, nor the most intelligent that survives. It is the one that is the most adaptable to change."

— *Charles Darwin*

5.1 Introduction

Chapter 4 studied the bulk structure of t-ZrO_2; however just as bulk, surfaces too are important. In order to probe and understand the nature of the various chemical reactions, the knowledge of the surface chemistry of the material involved is necessary. [1-3] Since surface chemistry takes place at the border between the solid state and the liquid or gas phase; it can be viewed as a meeting place between solid state and solution chemistry. [4-6] A great deal of quantitative description of a range of surface phenomena such as diffusion, adhesion, wetting, defect chemistry etc can be understood by surface science experiments. [7-11] The computational approach described in this chapter will shed more light in to the processes occurring at atomic level which will provide a basic understanding for factors contributing to the mechanisms of surface stabilities in t-ZrO_2. The results obtained from this study are of great importance to understand the catalytic applications of this material. The study of surface chemistry in the past has made countless contributions to the understanding of catalytic processes. [12] The concept of active site in heterogeneous catalysis is of great value and could be understood by looking at the surface chemistry of materials. [13-16]

Hence, for a proper understanding of this surface chemistry, it is important to identify the local geometries constitute the active site where catalysis actually takes place. In 1925 H. S. Taylor at Princeton University was one of the first to have envisaged the idea of active sites for catalysis by a coordinated unsaturated metal atom site. [17] Since then there has been significant research efforts aimed at detecting the active sites on surfaces needed for catalytic reactions. [18-21]

With the advent of the both computational and experimental surface science methods, working on atomically clean crystals, by cutting high miller index surfaces has been possible. [22-24] Computer simulation of clean surfaces can give us an insight to the atomic scale structure and any transitions that can occur during the various processes. [25-27] The motivation of this chapter is to understand the surface chemistry of the low index surfaces of t-ZrO_2. This kind of fundamental understanding will provide a detailed relationship between surface atomic structure and the chemical reactivity of the materials for future applications in catalysis research.

Since t-ZrO_2 has been widely used as a catalyst for many important reactions, understanding the surface structures is very critical for its application in this area. [28-31] The earlier simulation work on the surfaces of zirconia was done by Christensen and Carter, [32] where they applied the density functional theory (DFT) to calculate the surface energies and relaxations in zirconia. Similarly the earlier work of Robin Grimes

and his co-workers [33] studied the effect of hydroxylation of t-ZrO_2 surfaces. The surface energies obtained by Grimes *et. al*. are compared in this study.

5.2 Surface geometries and computational parameters

5.2.1 Static Energy Minimisation

We carried out surface relaxations using static energy minimization using the METADISE code [34-35] (Minimum Energy Techniques Applied to Defects, Interfaces and Surface Energies). The surfaces of interest here were the low miller index surfaces mainly {101}, {110}, {100}, {001} and {111} surface. The surface simulation cells are created by orientating the bulk unit cell so the surface of interest is perpendicular to the x-axis. The METADISE code then cuts through the planes to create possible surface terminations. This gives all the possible configurations for the particular Miller index. The structures were then relaxed using the Newton-Raphson [36] method. The size of region I and II is varied for each case until convergence is achieved. The cleavage of all the zirconia surfaces resulted in three types of possible terminations, one with zirconium, the second one with oxygen and the third one with equal amounts of both zirconium and oxygen. Table 5.1 provides a comparison of the energy differences between the zirconium and oxygen terminated surfaces. The surface energies of zirconium terminated surfaces were nearly double the energies of the oxygen terminated ones. This clearly indicates that the oxygen terminated surfaces have a much higher stability compared to

the zirconium terminated ones. Hence for the further study only the oxygen terminated ones were considered.

Table 5.1 Comparison of surface energies between zirconium and oxygen terminated surface

MILLER INDICES	ZIRCONIUM TERMINATED SURFACE (J/m^2)	OXYGEN TERMINATED SURFACE (J/m^2)
{101}	3.01	1.70
{110}	5.39	2.75
{001}	5.44	2.48
{111}	5.65	2.87

5.2.2 Molecular Dynamics

When temperatures were required in the model, we employ the MD computer code DL_POLY (Version 2.14), using a slab model to simulate the surface within 3D periodic boundary conditions. [37] A stack of two-dimensional slabs were generated for the present study. Using Region I from the previous calculation such that there is no interaction between the top and bottom of cell is included. The lattice vector perpendicular to the surface of interest is extended to create a vacuum gap in order to avoid mutual interactions. For the surface energy calculation we have used the convergence criteria where we increased the thickness of the slab until the energy values converged towards a constant value.

The slab-supercell geometry allows the application of periodic boundary conditions. The MD simulations of all oxygen terminated surfaces were performed in vacuum. A vacuum separation of 60 Å was set between the two periodically repeated slabs and each slab was symmetrical to avoid dipole-dipole interactions. The trajectories were generated in the NVT (constant number of particles, volume, and temperature) ensemble by means of the Verlet leapfrog algorithm. [38, 39] The slabs were run at 300 K for a time step of 0.1 femtosecond, using an NVT ensemble. In all simulations, the temperature is kept constant using the Nosé–Hoover thermostat. [40, 41] The simulation was monitored using the VMD analysis software [42] from which the structural changes occurring at different time steps could be recorded. The surface energies were calculated using the following formulae:

$$\gamma = [E_{surf} - E_{equiv\ bulk}]/2A \qquad (5.1)$$

Here E_{surf} is the total energy of the surface slab and $E_{equiv\ bulk}$ is the total energy of the bulk zirconium with equivalent number of atoms. The surface area is denoted as A and γ is divided by two because each slab has two equivalent surfaces.

5.3 Surfaces

The results from both the static and MD simulations are now discussed below:

5.3.1 *{101} Surface*

This surface is formed by a stacking sequence of charged planes. The repeat of the surface unit cell here is decided by looking at the layers forming the surface from the top view of the Figure 5.1. The figure illustrates the repeat unit to be made up of two oxygen layers on the surface followed by a zirconium layer, which is in agreement with earlier reported work. [33] Although this surface contains charged planes, the repeating unit here is adjusted in such a way that the entire unit has no dipole moment perpendicular to the surface and hence it is called a Type II surface. [33] It was observed that during the creation of this surface, the zirconium and oxygen atoms exposed on the surface lose one atom each. This results in zirconium assuming 7 fold coordination while oxygen a 3 fold coordination. The computed interlayer spacing between the outermost oxygen atom and

the zirconium atom below was found to be 0.6 Å as shown in Figure 5.1. Analysing the surface relaxations, it was noted that the relaxations happened only at the two uppermost layers. Chapter 4 indicated the presence of two types of bonds between Zr-O atoms, these were characterised as short bonds and long bonds. The shorter bond lengths were found to be 2.01 Å and the long ones were approximately 2.37 Å. The molecular dynamics run at 300 K also revealed values close to the static simulations, where the short Zr-O bond lengths were approximately 1.98 Å and the long ones were around 2.35 Å. Among the Zr-O atoms held between two layers, a shortening of bond lengths were observed as shown in Figure 5.3. The shortening of bond lengths was minimum for Zr-O atoms lying in the bulk. This shortening of bond lengths was only 0.5-0.8 % for the atoms in bulk while those for the surface varied between 4 to 10 % for atoms. This indicates that the displacement of atoms were minimum within the surface. From Figure 5.2 (b) it is noted that the surface retained much of its initial character after the static run. Table 5.2 reveals that the surface energies computed by both static and molecular dynamic techniques gave the lowest energy for this surface compared to all the other surfaces. Both methods also gave the similar surface energy values. Finally it is inferred here that the {101} surface is the most stable surface of t-ZrO_2.

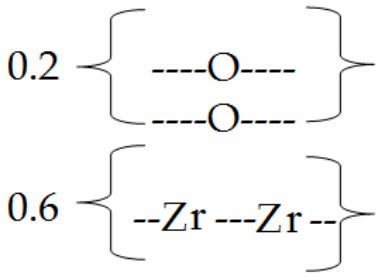

Figure 5.1 The stacking sequence and interlayer spacing (Å) on the oxygen terminated {101} surface of t-ZrO_2

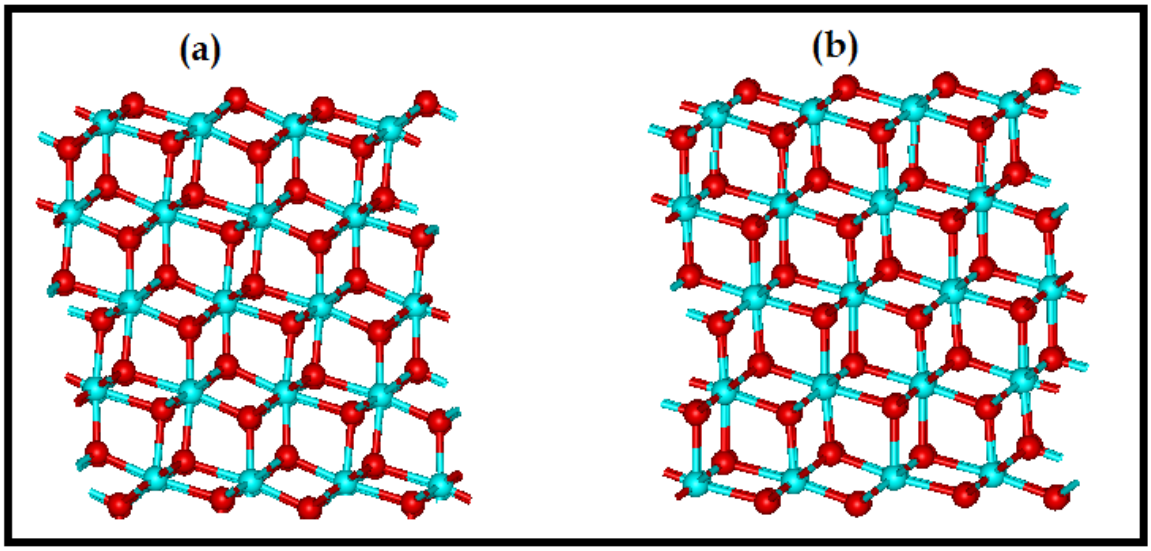

Figure 5.2 Comparison of structural relaxations using METADISE code for (101) surface (a) unrelaxed surface (b) relaxed surface.

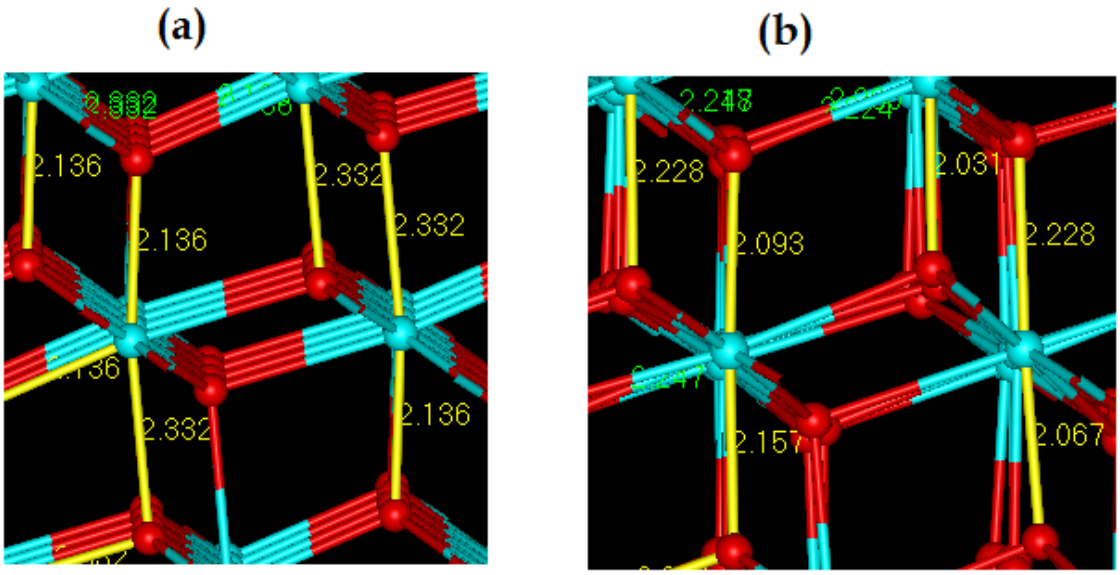

Figure 5.3 Change in bond length between the interlayer after the molecular dynamics run on pure {101} surface (a) unrelaxed surface (b) relaxed surface.

5.3.2 *{001} Surface*

The {001} surfaces of t-ZrO_2 were chosen for the study because these {001} phases and crystallite orientations were predominantly observed in experimental studies of ZrO_2 .[43]. It was observed that after cleavage of this surface, it is characterized by columns of oxygen atoms that lie perpendicular to the surface as shown in Figure 5.5. This is consistent with the earlier theoretical work done on this surface by Christensen et al. [32] The repeat of the surface unit cell here is formed from layers of oxygen alternated with zirconium as shown in Figure 5.4. Just as in the case of the {101} surface the repeating unit here is adjusted such that, the entire unit has no dipole moment perpendicular to the

surface and hence this too can be called as a Type II surface. The interlayer spacing between the outermost oxygen atom and inner zirconium atom is 1.2 Å, which is almost double that of the {101} surface. This indicates that the total compactness between the atoms is less here when compared to the {101} surface. The higher the compactness between atoms, the higher is the stability of the structure. The surface zirconium atoms are 6-fold coordinated while oxygen atoms are 2-fold and less than the {101} surface discussed earlier. Analysing the structural relaxation obtained from the static calculations, it was revealed that the relaxation process resulted in surface energies becoming almost half of the unrelaxed structures as observed from Table 5.2. The structural rearrangement here indicated that there was a shortening of the bond length of the surface oxygen atoms with the zirconium lying below it. The bond lengths decreased from 2.13 Å to 1.96 Å. During the relaxation process it was also noted that the surface atoms moved away from the bulk.

This resulted in an increase of Zr-O bond distance between the interlayer atoms. The largest Zr-O bond length was found to around 2.49 Å and the shortest around 1.96 Å. The MD run at 300 K showed a slight drop in surface energy values resulting in increased stability. It was observed here that there was a reduction in the coordination of the surface zirconium's atoms with the neighbouring oxygen atoms. The surface relaxation resulted in the zirconium atoms losing one more ligand and finally being coordinated to only five oxygen atoms on the surface. The shortening of Zr-O bond length for surface atoms was also observed here. This bond length varied between 1.9 Å to 2.1 Å. The final surface

energy values from Table 5.2 indicated that this surface is the second most stable surface among the other surfaces evaluated in t-ZrO_2.

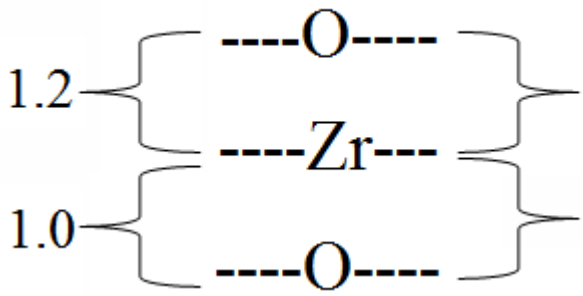

Figure 5.4 The stacking sequence and interlayer spacing (Å) on the oxygen terminated {001} surface of t-ZrO_2.

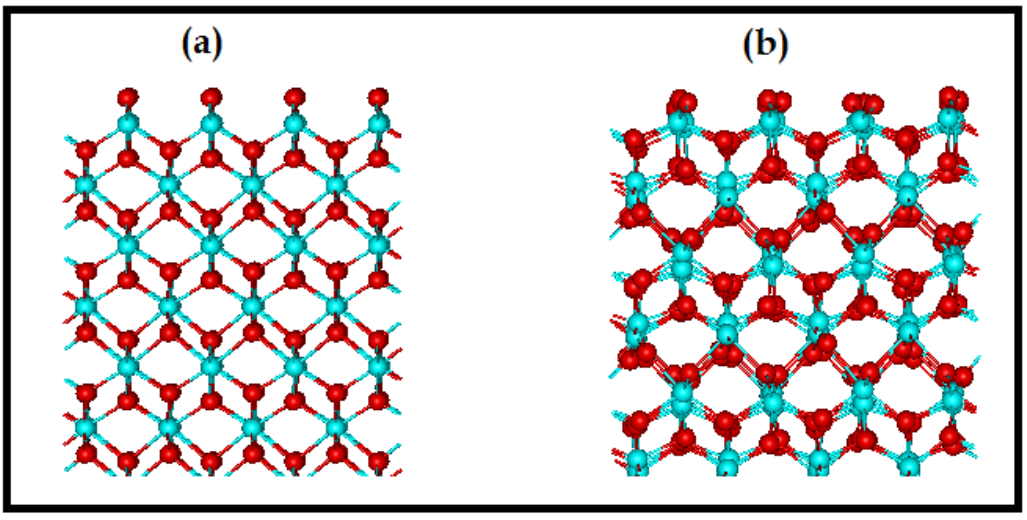

Figure 5.5 Comparison of structural relaxations using METADISE code for {001} surface (a) unrelaxed surface (b) relaxed surface

5.3.3 *{100} Surface*

This surface consists of stoichiometric amounts of ZrO_2 and hence is an example of a type I surface. This is in agreement with the earlier theoretical work reported by Robin Grimes and co-workers. [33] The repeat unit for this surface consists of equal amount of zirconium and oxygen on each layer. The interlayer spacing between the adjacent layers is 1.8 Å, which is the largest interlayer distance observed in this study see Figure 5.6. This indicates the atoms are less compact and hence the stability of this surface could also be expected to be lower. The surface energy values reported in Table 5.2 indicate that the energies obtained from the MD study showed the highest value. The surface zirconium atoms here are 6- fold and oxygen atoms are 3 fold in coordinations. The long and short Zr-O bond lengths were 2.33 and 2.13 Å respectively. The atomic arrangement of atoms on this surface is the same as to the one observed in bulk t-ZrO_2. The MD run at 300 K did indicate shortening of the Zr-O bond lengths for the surface atoms. The atoms on the surface moved around 0.1 Å towards the bulk from their equilibrium positions. Similarly, for the atoms within the bulk, increase in Zr-O bond lengths between 0.08 to 0.1 Å from their equilibrium position were noted. Although the relaxations on this surface were not very high, this surface was found to be the most unstable surface of t-ZrO_2 due to its high surface energies.

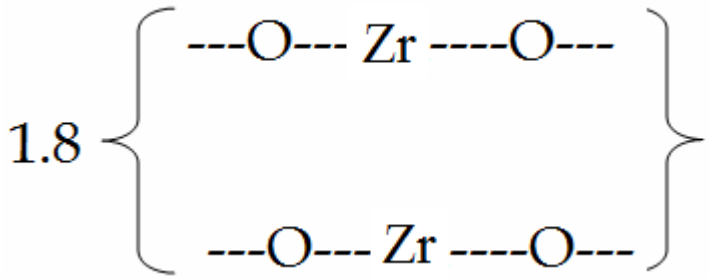

Figure 5.6 The stacking sequence and interlayer spacing (Å) on the Zr-O terminated {100} surface of t-ZrO_2.

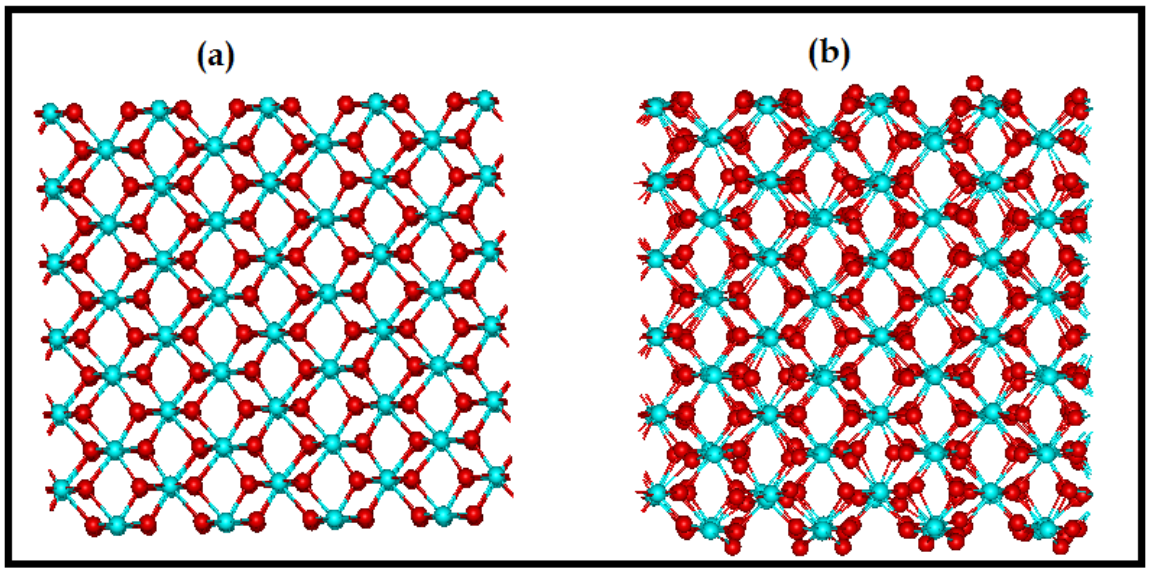

Figure 5.7 Comparison of structural relaxations using METADISE code for {100} surface (a) unrelaxed surface (b) relaxed surface.

5.3.4 *{110} Surface*

The earlier studies on the {110} surface of t-ZrO_2, revealed that this surface is formed in many catalytic preparations. [44] The HRTEM studies by Benaissa et. al. [44] on sulphated zirconium indicated the presence of a long flat {110} plane. Earlier DFT studies done by R. Añez *et al*. [45] also observed that the hydroxylation of t-ZrO_2 induces a strong stabilisation of the {110} surface of t-ZrO_2. They found that the hydroxylation on this surface was highly exothermic. It was postulated by them [45], that this higher stabilisation were due to the lower coordination of zirconium atoms on this surface compared to the {101} surface. It was suggested that this could be the reason for this surface appearing in many catalytic preparations. Therefore, it is important to analyse the characteristics of this surface. It was found that after cleaving the oxygen terminated surface, alternating negative and positively charged planes were observed. This suggests that the {110} surface is polar which is in agreement with the earlier studies. [33] Thus {110} surface is known as a type III surface and the repeat unit here is composed of alternating rows of oxygen and zirconium. The surface is reconstructed to remove the dipole using the methods described in section 2.3.3.2 of Chapter 2. The interlayer distance here is 1.2 Å, which shows it is more compact than the {100} surface Figure 5.8. The noticeable feature on this surface before reconstruction reveals that the oxygen atoms on the surface are arranged in a zig-zag manner as shown in Figure 5.7 (a). After the reconstruction, the zigzag manner is lost and it was observed that the oxygen atoms in the

surface layer are translated at least 1 Å from their bulk positions, away from the bulk crystal. The magnitude of changes in oxygen ion positions decreases with the increasing depth. After the MD run, the surface layer still consists of rows of alternating zirconium and oxygen atoms and the oxygen atoms were found to be still above the zirconium atoms. The shortest surface Zr-O bond lengths were found to be 1.88 Å and the largest was found to 2.41 Å. The relaxation process brought forth a reduction in the coordination of surface zirconium atoms which reduced from 6 to 5 and even 4. For oxygen atoms on surface a 2 or 3-fold coordination was found. The Table 5.2 indicates that the static simulation was successful in reconstructing the surface, which is indicated by the reduction in surface energies from 10 J/m^2 to 3.6 J/m^2. Similarly the rearrangement process by molecular dynamic calculations further reduced the surface energies to 2.7 J/m^2 which was close the earlier reported values. Thus a marked decrease in surface energies indicating higher stability was noted for this surface after the reconstruction process.

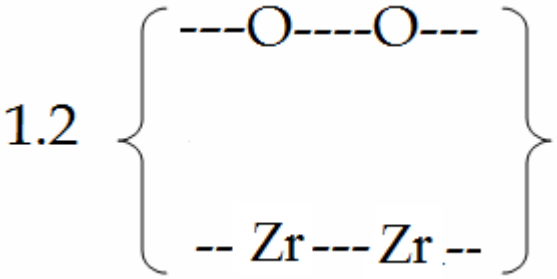

Figure 5.8 The stacking sequence and interlayer spacing (Å) on the oxygen terminated {110} surface of t-ZrO_2

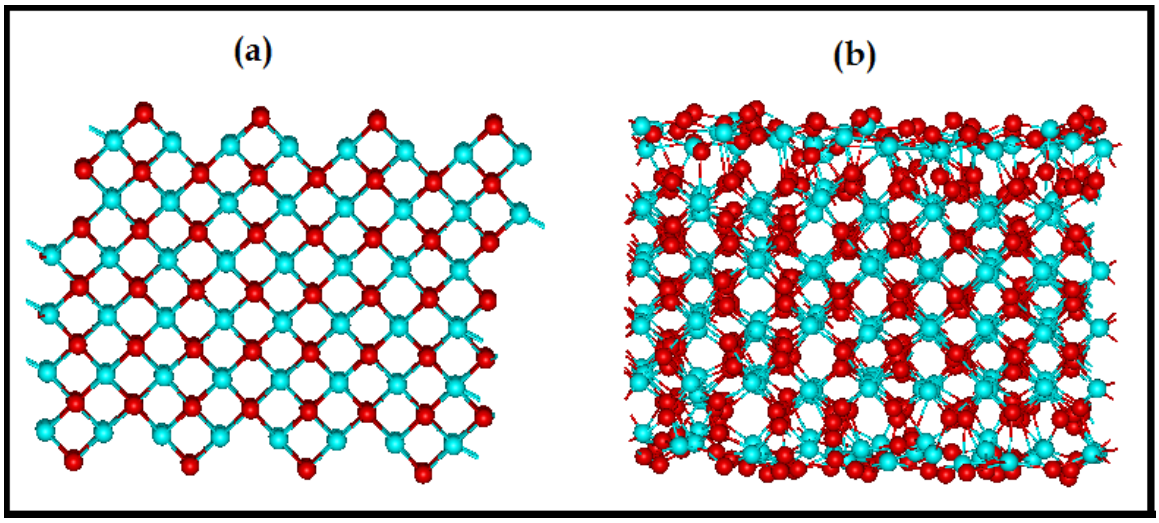

Figure 5.9 Comparison of structural relaxations (a) unrelaxed surface generated by METADISE code (b) relaxed surface generated after the MD run.

5.3.5 *{111} Surface*

The presence of {111} surfaces in t-ZrO_2 were observed experimentally when materials like molybdenum oxide [46] or sodium nitrate [47] were either doped or dispersed within the framework of zirconium. The HRTEM studies done by Morterra *et al*. [48] at lower calcination temperatures of 600°C, showed that yittria stabilized t-ZrO_2 appears to display small coin-like morphology with the {111} surface favoured. Since many such synthesis methods have detected the formation of {111} surface of t-ZrO_2 in their study, it is important to look at the structural arrangement of atoms on this surface.

The cleavage of the {111} oxygen terminated surface from the bulk t-ZrO_2 resulted in a stepped surface as shown in Figure 5.9 (a). The surface consisted of upper and lower terraces along with step edges. Since terraces and step-edges have different local geometries, they aid in additional adsorption capability for dopant atom. This causes enhanced segregation of dopants and is thus catalytically favourable. The repeat unit here was found to be same as that of {001} surface which is O-Zr-O. However, the computed interlayer distance between the top most oxygen layer and the zirconium layer beneath was found to be 0.6 Å, which is almost half that on the {001} surface, indicating higher compactness of atoms. The surface energy values obtained by METADISE calculation were found to be same as that on the {100} surface indicating instability of the structure. The MD run at 300 K was able to a achieve better structural relaxation leading to further lowering of the surface energies and making this surface more stable than the {110} and {100} surface.

The enhanced stability of this surface achieved after the MD run is indicated from the values obtained on Table 5.2. The stepped character of this surface was retained even after the MD run as shown in Figure 5.9. The shortest Zr-O bond length on this surface was found to be 1.84 Å and largest to be 2.33 Å respectively. The zirconium atoms on the terraces revealed a 5-fold coordination, while those at the corner sites between the upper and lower terraces where 6-fold or 7-fold in coordination. The oxygen atoms on the edges of the step were 2-fold coordinated, while those on the terraces were 3 fold in coordination as shown in Figure 5.12. The different species of under coordinated atoms

existing here are due to breaking up of bonds which could serve as a driving force for enhanced segregation of atoms. The oxygen atoms on the edges of the step moved 0.1 Å away from their initial position after relaxation resulting in an increase in Zr-O bond length. The layer of oxygen atoms lying below the surface zirconium atoms move towards the surface. Finally it is noted that this surface is the third most stable one of the t-ZrO_2 surfaces considered. This stability might be due to the higher compactness of atoms found on this surface.

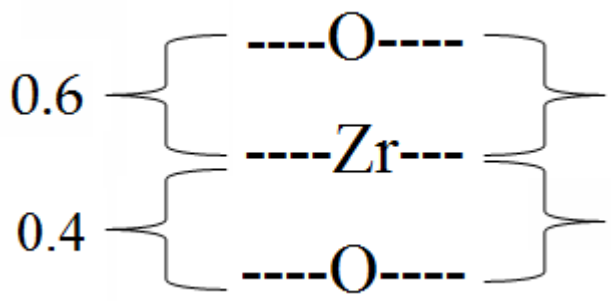

Figure 5.10 The stacking sequence and interlayer spacing (Å) on the oxygen terminated {111} surface of t-ZrO_2.

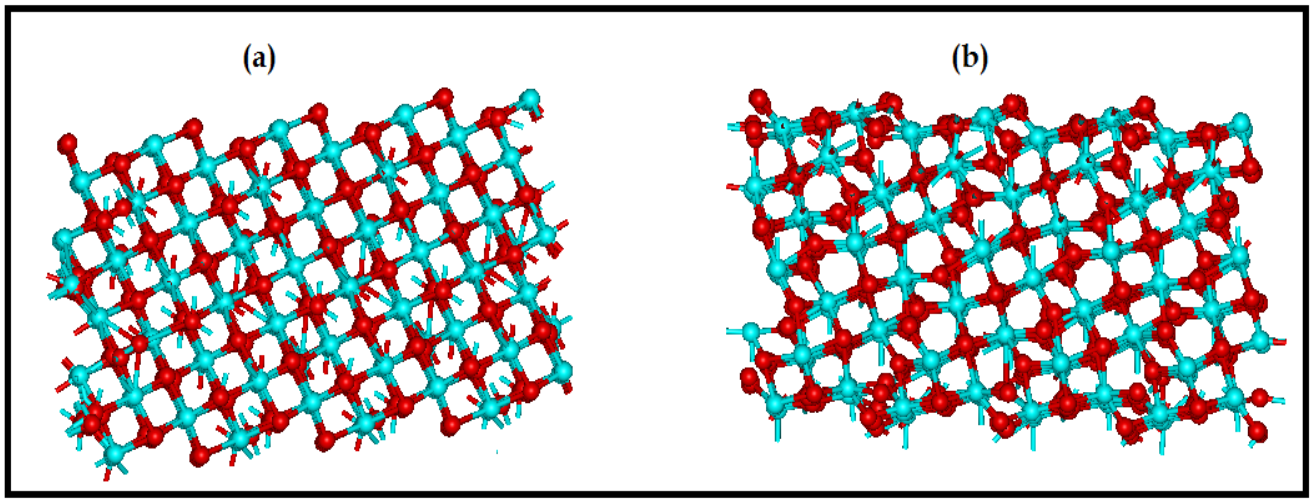

Figure 5.11 Comparison of structural relaxations (a) unrelaxed surface generated by METADISE code (b) relaxed surface after a 300 K MD run.

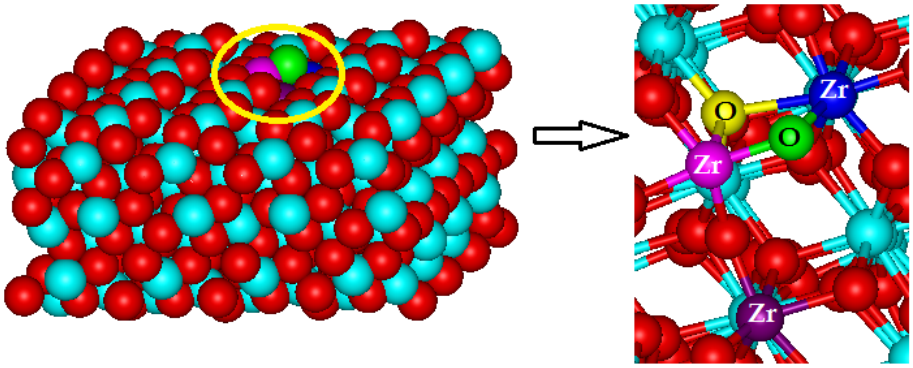

Figure 5.12 The variation of different coordination environments for zirconia and oxygen atoms, the following are the coordination numbers: Zr in blue is 7, in Purple is 6, in Pink is 5. Oxygen in yellow is 3 and in green is 2.

Table 5.2 Comparison of surface energies using different approaches

Surface	γ unrelaxed (J/m^2) Using METADISE	γ relaxed (J/m^2) Using METADISE	γ relaxed (J/m^2) from previous work	γ relaxed (J/m^2) at 300 K using DL_POLY
{101}	1.9	1.7	1.65	1.7
{001}	4.8	2.4	-	2.3
{100}	4.0	2.8	2.57	2.9
{110}	10.1	3.6	2.63	2.7
{111}	6.7	2.8	-	2.6

5.4 Conclusion

This study found the characteristics of the low index miller surfaces of t-ZrO_2 were in accordance with the previous computational study done by Grimes and co-workers [33]. The stability of an oxygen terminated surface was found to be always higher than the zirconium terminated ones. The cleavage of the surfaces from the bulk resulted in the breaking up of the Zr-O bonds on the surface. This resulted in variation of Zr-O bond

lengths for all surfaces. In the bulk phase of t-ZrO_2 each zirconium atom is surrounded by eight oxygen atoms forming two tetrahedra, one with short Zr-O bonds and one with long Zr-O bonds. However, cutting of surfaces resulted in reduction of the zirconia coordination. The highest coordination for zirconium atoms were found to be on the {101} surface.

The {101} surface is by far the most stable followed by the (001) surface. This conclusion is supported by the earlier experimental and computational studies done on t-ZrO_2 where the oxygen terminated {101} crystal planes were detected to be preferentially exposed followed by oxygen terminated {001} surface. This higher stability could be attributed to its higher coordination of the surface zirconium atoms and lower surface energies. This conclusion is also corroborated by earlier DFT work done by Sojka *et al*., [49] who observed long {101} plane terminations in t-ZrO_2 followed by {001} and {111} planes. The surface stability for t-ZrO_2 after the MD study at 300 K was found to be in following order {101} > {001} > {111} > {110} > {100}. Although this chapter successfully looked at the various surfaces of t-ZrO_2, all these studies were done on clean surfaces. The next chapter will look at the effects of defects on both the bulk and pure surfaces of t-ZrO_2.

5.5 References

[1] C. T. Campbell, S. C. Parker, D. E. Starr, *Science*, 298 (2002) 811.
[2] T. Tsirlin, J. Zhu, J. Grunes, G. A. Somorjai, *Top. Catal*, 19 (2002) 165.
[3] G. Ertl, *Angew. Chemie Int Ed*, 47 (2008) 3524.
[4] J. K. Nørskov, F. Abild-Pedersen, F. Studt, T. Bligaard, *Proc. Natl. Acad. Sci*., 108 (2011) 937.
[5] M. Valden, X. Lai, D.W. Goodman, *Science*, 281 (1998) 1647-1650.
[6] R. Schlogl, *Angew. Chemie Int Ed*, 42 (2003)2004.
[7] S. Linic, J. Jankowiak, M. A. Barteau, *J. Catal*, 224 (2004) 489.
[8] Y. Y. Yeo, L. Vattuone, D. A. King, *J. Chem. Phys*, 106 (1997) 392.
[9] D. W. Goodman, R. D. Kelley, T. E. Madey, J. T. Yates, *J. Catal*, 63 (1980) 226.
[10] O. Lytken, W. Lew, J. J. W. Harris, E. K. Vestergaard, J. M. Gottfried, C. T. Campbell, *J. Am. Chem Soc*, 130 (2008) 10247.
[11] B. Xu, L. Zhou, R. J. Madix, C. M. Friend, *Angew. Chem Int Ed*, 49 (2010) 394.
[12] J. T. Yates, C. T. Campbell, *Proc. Natl. Acad. Sci*, 108 (2011), 911.
[13] M. Boudart, *Adv. Catal*., 20 (1969) 153.
[14] M. Boudart, G. Dje´ga-Mariadassou, *Kinetics of Heterogeneous Catalytic Reactions, Princeton University Press, Princeton*, New Jersey, 1984.
[15] A. T. Gwathmey, R. E. Cunningham, *Adv. Catal*., 10 (1958) 57.
[16] G. A. Somorjai, *Surface Chemistry and Catalysis*, Wiley, New York, 1994.
[17] H. S. Taylor, *Proc. R. Soc*. London, Ser. A, 108 (1925) 105.
[18] J. K. Nørskov, T. Bligaard, B. Hvolbæk, F. Abild-Pedersen, I. Chorkendorffc, C. H. Christensen, *Chem. Soc. Rev*., 37 (2008) 2163.
[19] J. T. Yates Jr., *J. Vac. Sci. Technol*., A, 13 (1995) 1359.
[20] T. Zubkov, G. A. Morgan Jr., J. T. Yates Jr., O. Kuhlert, M. Lisowski, R. Schillinger, D. Fick, H. J. Jänsch, *Surf. Sci*., 526 (2002) 57.
[21] T. Zambelli, J. Wintterlin, J. Trost, G. Ertl, *Science*, 273 (1996) 1688.
[22] S. Dahl, A. Logadottir, R. C. Egeberg, J. H. Larsen, I. Chorkendorff, E. J. K. Nørskov, *Phys. Rev. Lett*., 83 (1499) 1814.
[23] H. S. Bengaard, J. K. Nørskov, J. Sehested, B. S. Clausen, L. P. Nielsen, A. M. Molenbroek, J. R. Rostrup-Nielsen, *J. Catal*., 209 (2002) 365.
[24] R. T. Vang, K. Honkala, S. Dahl, E. K. Vestergaard, J. Schnadt, E. Lægsgaard, B. S. Clausen, J. K. Nørskov and F. Besenbacher, *Nat. Mater*., 4 (2005) 160.
[25] D. W. Blakeley, G. A. Somorjai, *J. Catal*., 42 (1976) 181.
[26] G. A. Somorjai, R. W. Joyner, B. Lang, *Proc. R. Soc*.,London, Ser.A, (1972) 331.
[27] H. Jonsson, *Proc. Natl. Acad. Sci*, 108 (2010) 944.
[28] Y. A. Ono, *Catal. Today*, 81 (2003) 3.
[29] J. G. Santiesteban, J. C. Vartuli, S. Han, R. D. Bastian, C. D. Chang, *J. Catal*., 168 (1997) 431.
[30] S. Kuba, P. Lukinskas, R. Ahmad, F. C. Jentoft, R. K. Grasselli, B. C.Gates, H. Knözinger, *J. Catal*., 219 (2003) 376.
[31] M. Hino, K. J. Arata, *Chem. Soc., Chem. Commun*.,18 (1980) 851.
[32] A. Christensen, E. A. Carter, *Phys. Rev*. B, 58 (1998) 8050.

[33] S. E. Redfern, R. W. Grimes, R. D. Rawlings, *J. Mater. Chem*., 11, (2001) 449.

[34] G. W. Watson, E. T. Kelsey, N. H. De Leeuw, D. J. Harris, S. C. Parker, *J. Chem.Soc. Faraday. Trans*., 92 (1996) 433.
[35] P. W. Tasker, *Philos. Mag*. A, 39 (1979) 119.
[36] E. Süli, D. Mayers, *An Introduction to Numerical Analysis*, Cambridge University Press, 2003.
[37] W. Smith, T.R. Forester, *J. Mol. Graphics*, 14 (1996) 136.
[38] L. Verlet, *Phys. Rev*., 159 (1967) 98.
[39] R. W. Hockney, *The Potential Calculation and Some Applications*; Academic Press: New York/London, 1970; Vol. 9.
[40] S. Nosé, *J. Chem. Phys*., 81 (1984) 511.
[41] W. G. Hoover, Phys. Rev. A, 31 (1985) 1695.
[42] W. Humphrey, A. Dalke, K. Schulten, *J. Mol. Graph*., 14 (1996) 33.
[43] J. Aarik, A. Aidla, H. Mandar, T. Uustrate, V. Sammelselg, *Thin Solid Films*, 408 (2002) 97.
[44] M. Benaissa, J.G. Santiesteban, G. Díaz, C.D. Chang, M. José-Yacamán, *J. Catal*. 161 (1996) 694.
[45] R. Añez, A. Sierraalta, G. Martorell, P. Sautet, *Surf. Sci*., 603 (2009) 2526.
[46] Y. Hu, L. Dong, J. Wang, Y. Chen, C.Li, M. Li, Z. Feng, P. Ying, *Chem. Lett*., (2000) 904.
[47] Z. Liu, W. Ji, L. Dong, Y. Chen, *J. Solid State Chem*, 138 (1998) 41.
[48] C. Morterra, G. Cerrato, L. Ferroni,L. Montanara, *Mat. Chem. and Phys*., 37 (1994) 243.
[49] W. Piskorz, J. Grybos, F. Zasada, P. Zapała, S. Cristol,J. Paul, Z. Sojka, *J.Phys. Chem.C*, 116 (2012) 19307.

Chapter 6 Defect chemistry of t-ZrO_2 on Bulk and Surfaces

"Certain defects are necessary for the existence of individuality."

— *Johann Wolfgang von Goethe*

6.1 Introduction

Any crystal to be known as an ideal crystal would display an exact stoichiometric ratio between its constituents. In such a case each ion within the structure would occupy the exact lattice site, such a state is called an equilibrium state. In a real crystal the ions are not fixed into their lattice sites but vibrate around their lattice positions. When the ions have acquired enough energy due to their vibrational energy or an increase in temperature, a movement of ions could cause the formation of either vacancies or interstitials. Defects occur in a crystal during material processing or it could be artificially induced by bombardment with high energy particles like neutrons or protons. Since most of the important properties of crystals are due to the defects present, it is important to know what types of defect would dominate in a crystal structure. [1] The types of defects would depend on the type material being considered, however looking at the various types of low index surfaces in a crystal the affinity for a certain type of defect species could be predicted. In 1926 Frenkel introduced the notion of point defects in crystalline solids to elucidate the phenomenon of diffusion. [2] It is well known today that not only diffusion but almost all important properties of crystalline solids are affected by

defects and in particular, by point defects.[3] Zirconia (ZrO_2) belongs to the list of the most important metal oxides due to its wide usage in different technological applications. [4] In fuel cells it is used as an electrolyte and gas sensors, as a thermal barrier coating, and as a protective natively grown layer against nuclear fuel cladding corrosion in light water nuclear reactors. [5-10] ZrO_2 has been widely used in the reaction of CO hydrogenation to light hydrocarbons, especially in the reaction of F-T synthesis, for its acidity/basicity, and oxidation/reduction properties. [11, 12] Different ZrO_2 phases have different catalytic performances for CO hydrogenation to hydrocarbons, oxygenates and olefins respectively. [13] For ZrO_2 to be used in all these applications, it has been stabilised by the addition of different types of dopants depending on its application. For example in order to be used as a solid electrolyte like in oxygen sensors, ZrO_2 is stabilised with yittria (Y_2O_3) or Calcia (CaO).[14, 15] The addition of these stabilisers results in the increase of intrinsic oxygen vacancies resulting in a material with high ionic conductivity.

The aim of this chapter is to first look at the point defects occuring in t-ZrO_2. Defects mainly fall in to two main categories intrinsic and extrinsic. Intrinsic defects are of two types Schottky and Frenkel defects. Extrinsic defects occur when a foreign atom like WO_3 is inserted into the lattice. This chapter will see how a defect is formed within the tetragonal zirconia crystals and also monitor the role of various dopants introduced within it.

The migration of defects within the crystal is yet another important aspect which we consider in this chapter; this also has a profound influence in its catalytic properties. These migrations can be viewed as millions of tiny hops, where there is a migration energy associated with each hop. This chapter will also look at the migration of oxygen defects in the presence of dopants. Whether a dopant helps in reducing the activation barrier for oxygen transport is also discussed here.

6.2 Simulation Methods and Point Defects

By employing atomistic simulation techniques the details of defect chemistry of t-ZrO_2 are evaluated. Initially defects are introduced within the bulk of t-ZrO_2, treating them as isolated defects, where a perfect crystal would contain only one single defect. This is done by two approaches for comparison 1) Mott-Littleton 2) Supercell. [16, 17] The calculation of isolated defects on the various low index surfaces of t-ZrO_2 were then carried out using the CHAOS program which is a modification of the Mott-Littleton method. The perfect crystal was relaxed using energy minimization at constant pressure. The energies of formation of single defects were calculated using both Mott-Littleton and supercell method and the results are summarized in Table 6.1. A 5x5x5 supercell was utilised for the supercell approach and region sizes of (15, 25) were used for Mott-Littleton both are a result of convergence tests.

From the results it follows that there is a good possibility for an anion vacancy due to the lower formation energy compared to a cation vacancy. The single defect formation energy values from Table 6.1 compares well with the values estimated between tetragonal and earlier reported values of cubic forms. [18] Earlier studies have indicated that the formation energies of intrinsic vacancies in cubic, tetragonal and monoclinic zirconia polymorphs are close to each other. [19] Hence the formations of Schottky and Frenkel defects too are discussed in this chapter.

The cations for substitutional defects were chosen in order to obtain greater insight into the mechanism of diffusion by selecting ions with different charge and size with respect to the host cation Zr^{4+}. The energy of substituting ZrO_2 with dopants as shown in Table 6.2 indicated that as the dopant size increases the defect energies values tended to be more positive. Thus it could be inferred that the smaller the size of the cation the better is its substitutional capability. Tungsten (W^{6+}) with the highest positive charge and the lowest ionic radius had a better preference to all the other cations introduced in to the bulk of t-ZrO_2 framework. The order of stability for substitutional defects here is: W^{6+} > Nb^{5+} > Ce^{4+} > Y^{3+} > Ca^{2+}. The Figures 6.1, 6.2 and 6.3 indicate the convergence of defects energy values using both supercell and Mott-Littleton Approaches. A good convergence was brought by the increase in region sizes for the Mott-Littleton approach.

Table 6.1 Calculated Single-Defect Formation Energies in pure t-ZrO_2

Single Defect in Bulk t-ZrO_2	**Energy (eV) by Mott-Littleton method**	**Energy (eV) by Supercell method**	**Energy (eV) for Cubic ZrO_2** (Reference [18])
$O_i^{//}$	-8.25	-9.26	-9.21
$V_O^{\bullet\bullet}$	15.52	16.20	14.87
$Zr_i^{4\bullet}$	-64.09	-66.77	-65.22
$V_{Zr}^{4/}$	90.41	88.83	85.66
$W_{Zr}^{\bullet\bullet}$	-79.21	-81.07	------
$Ca_{Zr}^{//}$	62.11	61.73	59.16
$Ce_{Zr}^{\times}$	5.94	5.75	3.37
$Nb_{Zr}^{\bullet}$	-54.33	-54.18	-57.98
$Y_{Zr}^{/}$	35.95	35.45	33.03

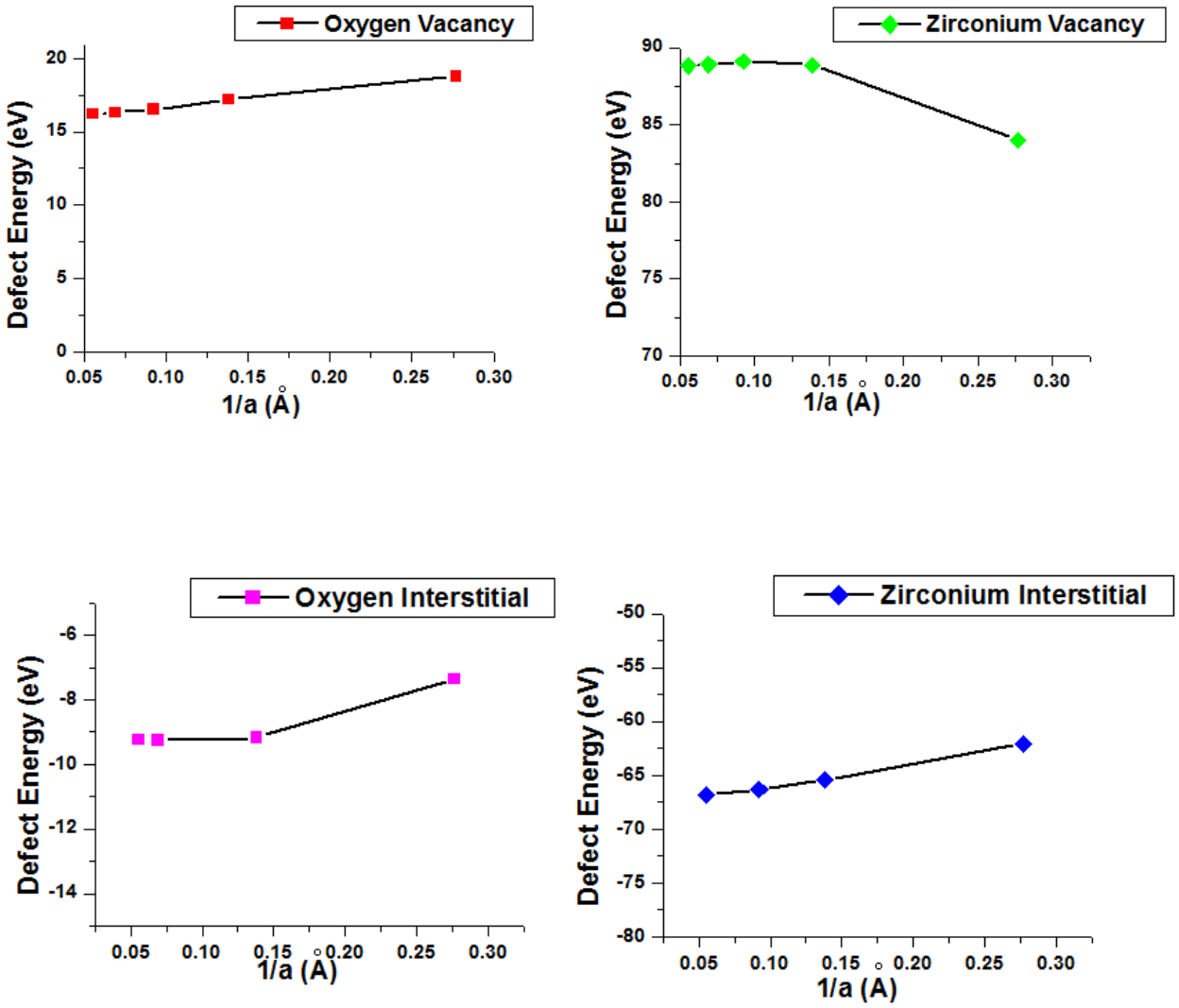

Figure 6.1 The convergence of the defect formation energy is shown in for oxygen vacancy, oxygen interstitial, zirconium vacancy and zirconium interstitial using supercell approach.

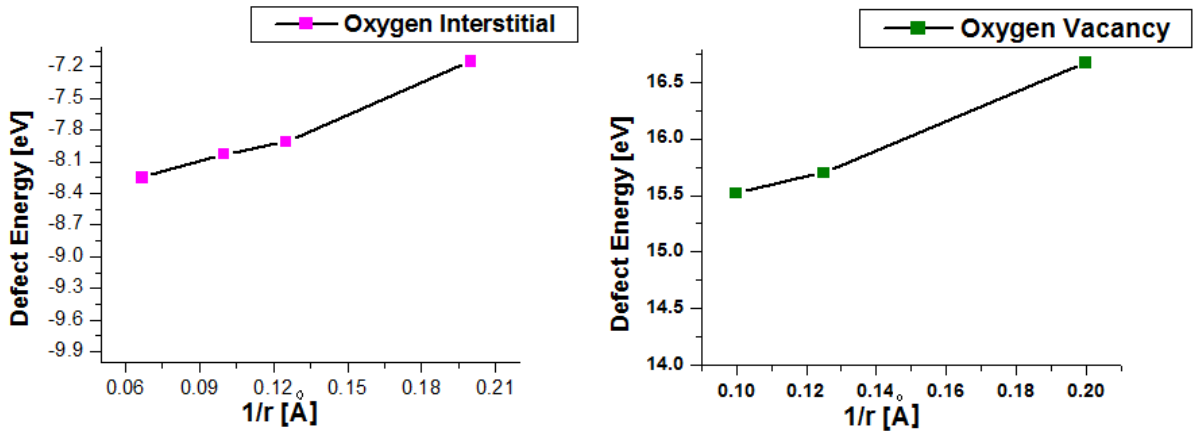

Figure 6.2 The convergence of the defect formation energy with increasing inner radius is shown in for oxygen vacancy, oxygen interstitial using the Mott-Littleton approach.

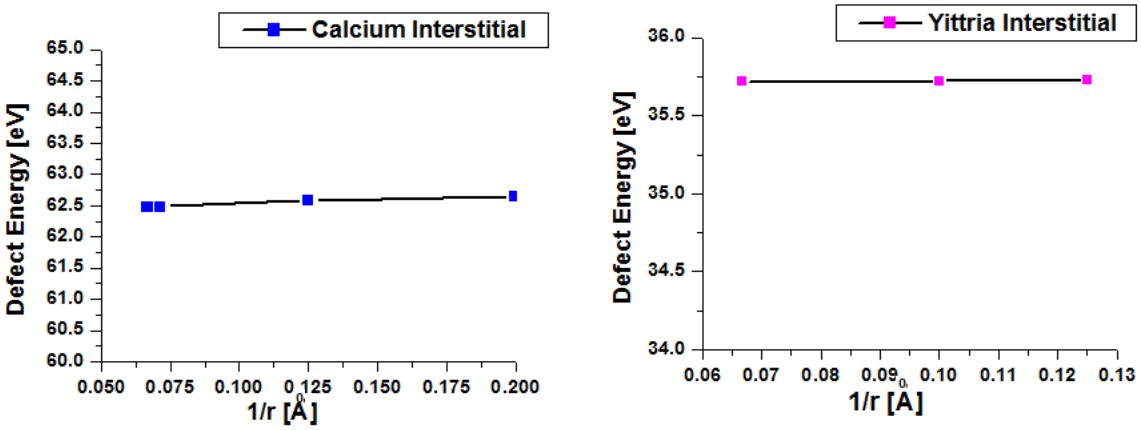

Figure 6.3 The convergence of the defect formation energy with increasing inner radius is shown in for Ca^{2+}, W^{6+}, Ce^{4+}, Nb^{5+}, Y^{3+} substitution using the Mott-Littleton approach.

6.3 Schottky and Frenkel Defects

There are distinct defect equilibria associated with the formation of intrinsic defects in t-ZrO_2; the equation for these are shown in Table 6.2. With respect to the energies the most favourable mechanism is to form a vacancy in the bulk of a metal oxide is the so-called Schottky and Frenkel mechanism (see section 2.3.6 of Chapter 2). Schematic representations of both the mechanisms in t-ZrO_2 are shown in Figure 6.4 (a) and (b). The results from Table 6.3 indicate that the values of both Schottky and anion Frenkel defects are similar. However, there exists a good possibility for the formation of a Schottky defect in bulk t-ZrO_2. The energy of a cation Frenkel is 13.16 eV which is approximately 10 eV more than its Schottky trio energy of 3.45 eV and hence the formation of a cation Frenkel is less likely to occur. The values of these defects energy follow a similar trend with their corresponding c-ZrO_2 defect energies. The relative preference for a Schottky defect is in conjunction with the earlier experimental evidence suggesting of Schottky's dominations in t-ZrO_2 crystal. [41] The presence of a high level of ionic coordination environment in t-ZrO_2 crystal could be the cause for the existence of this defect.

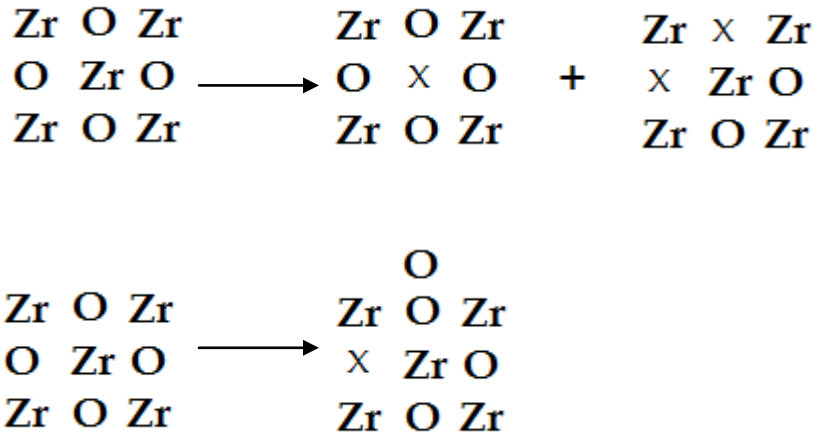

Figure 6.4 (a) Representation of Schottky snd Frenkel Mechanism in t-ZrO_2.

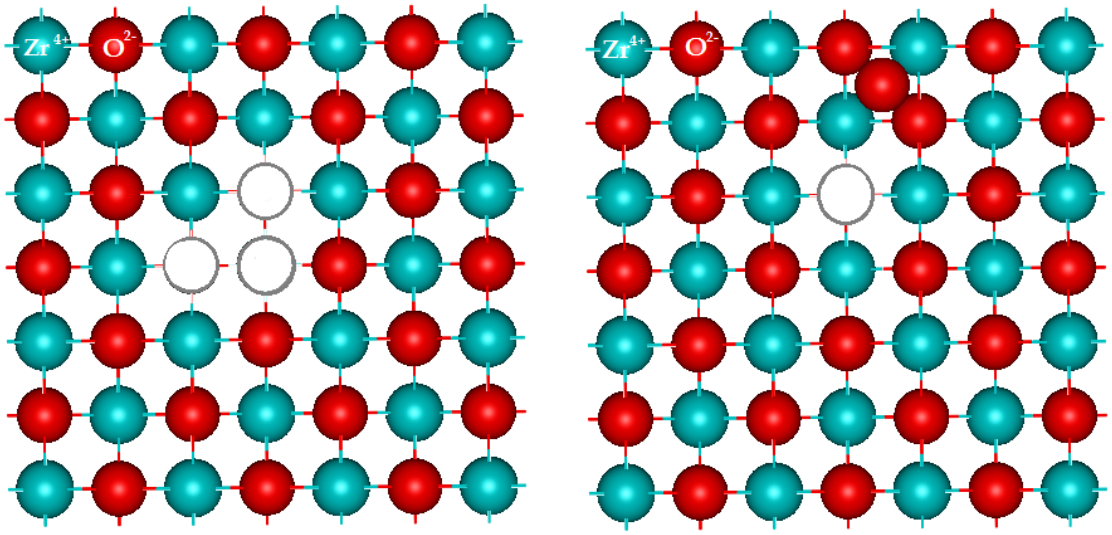

Figure 6.4 (b) Schematic representations of Schottky and oxygen Frenkel Mechanisms in t-ZrO_2.

Table 6.2 Calculated Energies of Schottky and Frenkel

Defect Reactions for t-ZrO_2			
Process Defect equation energy	Energy (eV)	Energy per ion in t-ZrO_2 (eV)	Energy per ion in c-ZrO_2 (eV) [*Ref (18)*]
Schottky $Zr + 2O = V_{Zr}^{////} + 2V_O^{\bullet\bullet} + ZrO_2$	10.36	3.45	3.21
Cation Frenkel $Zr = Zr_i^{4\bullet} + V_{Zr}^{////}$	26.32	13.16	15.55
Anion Frenkel $O = O_i^{//} + V_O^{\bullet\bullet}$	7.27	3.63	4.44

A logical extension is to consider the behaviour of these defects in the low Miller index surfaces of t-ZrO_2. Since the anion Frenkel energy value on bulk is only 5 % greater than the Schottky defects on bulk, it is important to check the relative preference for both type of defects when checking for surfaces. To study the formation of these defects on the different surfaces of t-ZrO_2 the CHAOS code was used. This code allows to calculate

single defect energies on different surfaces using various optimisation techniques (see section 2.3.8 of Chaper 2). [20] A Newton Raphson optimisation technique was utilised in these calculations. The converged values were obtained by increasing the size of region from 100 to 400 and then plotting the corresponding energy values against the inverse of the region size. The plot which is a straightline is then extrapolated to the Y axis and the intercept gives the converged values. The results from CHAOS calculations on different surfaces are summarised in the Table 6.3.

The values from the Table 6.3 suggest that the {101} surface has the lowest Frenkel energies while the {110} surface has the lowest Schottky energies compared to all the other surfaces. The Frenkel formation energy for all surfaces except the {001} surface lowered in comparison with its corresponding bulk structure. The percentage of lowering varied between 22 % and 87 %. Unlike the nature of the defect reactions that occurred in the bulk, the Schottky's on surfaces depicted higher values in comparison to the anion Frenkel defects on all the surfaces except the {110} surface. Generally for Frenkel defects to occur within the crystal lattice, the coordination number must be low. The lower coordination of atoms found on surfaces compared to the bulk might be the reason why the Frenkel defects dominate on surfaces. Thus it can be concluded that a good chance for the migration of oxygen atoms from a vacant site to an interstitial site exist for all surfaces of t-ZrO_2. This kind of oxygen mobility has important applications which are discussed in the next section.

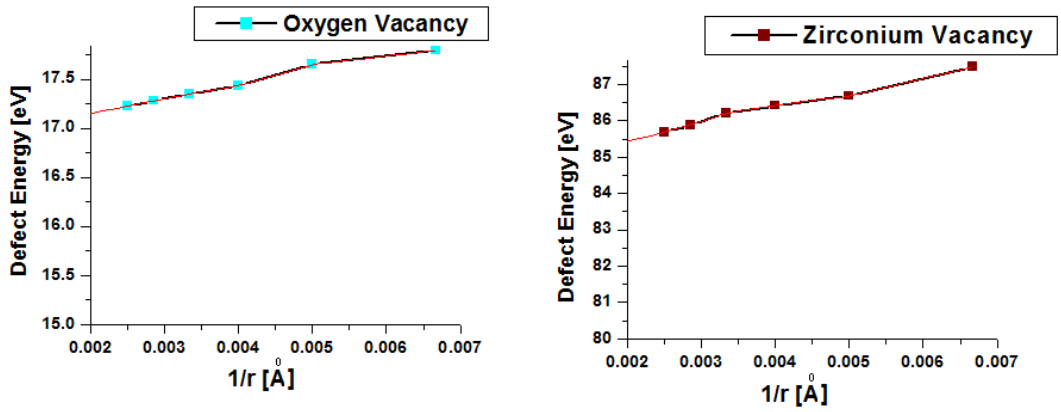

Figure 6.5 The convergence of the defect formation energy using Chaos method is shown in for Oxygen vacancy, Zirconium vacancy on {100} surface..

Table 6.3 Calculated Energies of Schottky and anion Frenkel on various surfaces of t-ZrO_2

Surfaces- *(Chaos-Method)*	$V_O^{\bullet\bullet}$	$O_i^{//}$	$V_{Zr}^{////}$	**Schottky per ion**	**Anion Frenkel Per ion**
{001}	36.33	-30.66	57.27	6.28	2.83
{101}	24.32	-23.43	66.88	1.48	0.44
{110}	35.35	-33.29	39.26	-1.12	2.06
{100}	17.15	-12.36	85.42	2.88	2.39
{111}	22.04	-17.73	78.33	4.70	2.85

6.4 Oxygen Migration

ZrO_2 is considered as an important material for application in high-temperature electrolysis, [27] gas sensors, [28] solid oxide fuel cells- (SOFCs), [29-33]. For example the solid solutions of ZrO_2–CeO_2 as well as yttria doped zirconia are one of the most promising electrolyte for fuel cells. [34, 35] Since defects such as oxygen vacancies have a major impact on the type of application, a lot of experimental as well as computational investigations have been carried out to study their effects. In recent years, increased attention has been given to the role of oxygen mobility in improving the catalytic stability of ZrO_2. [36] The enhanced oxygen mobility could reduce the oxygen deficiency at the surface, which could be utilised to design a better catalyst. The migration of an oxygen atom from an interstitial site to the nearest vacancy site needs to overcome certain barrier energy which could be referred to as its activation energy. The additions of certain dopants help to lower this energy barrier while other dopants would make it even more difficult.

The present study utilises the CHAOS program for studying the migration of oxygen atom from an interstitial site to a vacant site both in the presence and absence of dopants. The {110} surface of t-ZrO_2 constructed earlier was utilised to study the oxygen vacancy migration. The Figure 6.7 indicates the effects on the activation energy profile by various

dopants used in this study on {110} surface. It is clear that cations like Ca^{2+}, Y^{3+} and Ce^{4+} increase the activation energy barrier while Nb^{5+} and W^{6+} help to decrease the activation energy barrier. Thus incorporating Nb^{5+} and W^{6+} within the ZrO_2 framework will result ease of oxygen migration. The addition of W^{6+} resulted in reducing the activation energy barrier from 0.31 eV to 0.08 eV, which was found to be the lowest in all cases as shown in Table 6.5. It could be also deduced from these results that the addition of tungsten (W^{6+}) atoms to t-ZrO_2 might result in improvement of the catalytic properties of t-ZrO_2.

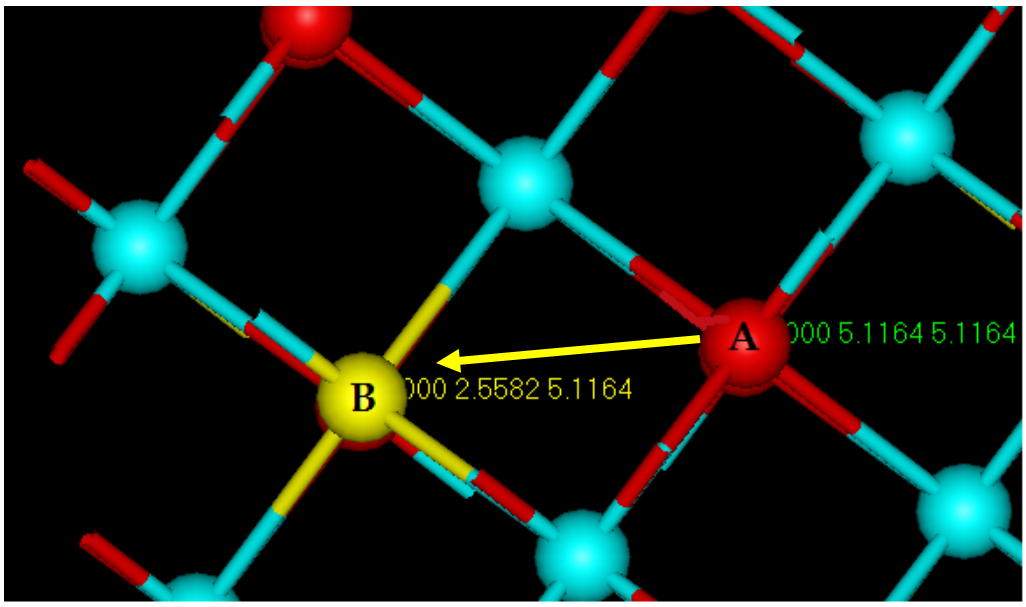

Figure 6.6 The migration of oxygen atom from an interstitial site (A) to the nearest vacancy site (B).

Table 6.4 Calculated Activation Energies in the presence of dopants

Species	Activation Energy E_a (eV)	Ionic Radius (pm)
Pure ZrO_2	0.31	86
W^{6+}	0.08	74
Nb^{5+}	0.11	78
Ce^{4+}	0.5	101
Y^{3+}	0.79	104
Ca^{2+}	1.53	114

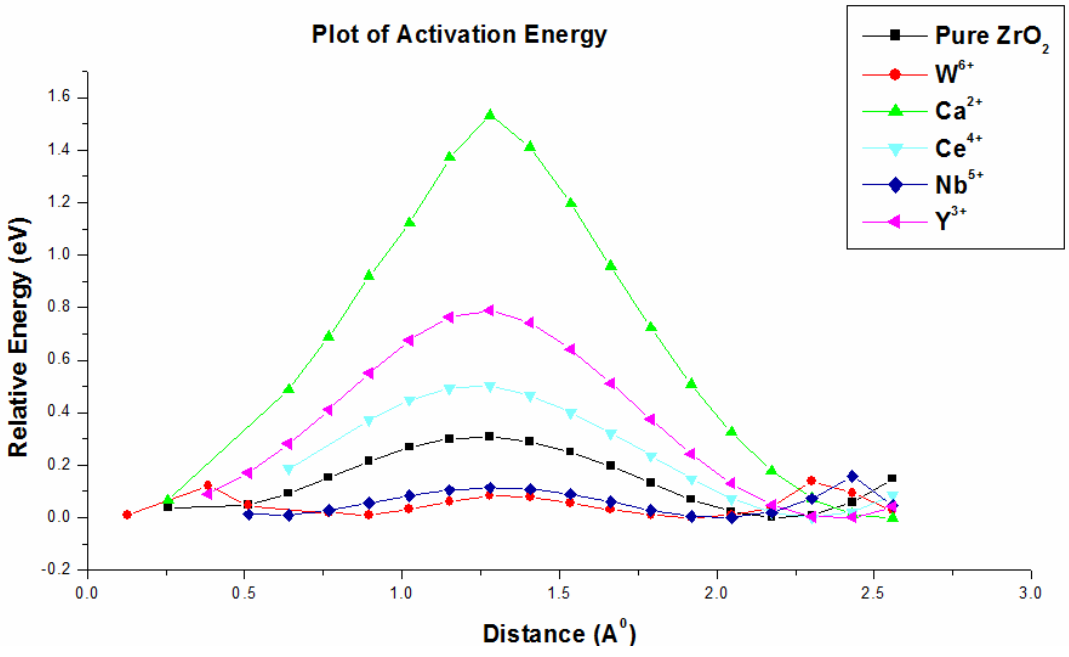

Figure 6.7 A plot of activation energy profile for t-ZrO_2 in the presence of various dopants.

6.5 Tungsten on Bulk Zirconia

Since tungsten is capable of lowering the activation energy of oxygen migration, its role as a dopant in bulk t-ZrO_2 is analysed here. The existing theories of substituting ions in to the zirconia framework for stabilising the tetragonal form of zirconia are still not fully understood. It was proposed earlier by Chen *et al.* [37-39], that aliovalent cation dopants are generally believed to substitute for zirconium ion in the cation network creates oxygen vacancies for charge compensation. The stabilisation here postulates that the dopant cation tends to reduce the average zirconium coordination number for stabilising the higher polymorphic tetragonal phase. Thus this mechanism of stabilisation could be due to two effects 1) the creation of oxygen vacancies and 2) due to the reduction of average coordination number of zirconium atoms in order to facilitate relaxation to form the tetragonal phase. We begin our simulations with the pure zirconia system modelled previously and obtain three routes for introducing tungsten (W^{6+}) into the bulk supercells. The bulk supercells were increased in size till convergence was reached. Three types of possible mechanisms for tungsten introduction in to bulk t-ZrO_2 is as follows:

1) **Type I** introducing a single tungsten atom by replacing two zirconia and one oxygen atom in the bulk.

2) **Type II** introducing two tungsten atoms within the bulk by replacing three zirconia atoms.

3) **Type III** introducing a single tungsten atom by creating an oxygen interstitial and removing a single zirconia atom.

$$Type-I = WO_3 + 2Zr_{Zr}^{\times} + O_o^{\times} \rightarrow W_{Zr}^{\bullet\bullet} + V_{Zr}^{////} + V_O^{\bullet\bullet} + 2ZrO_2 \qquad (6.1)$$

$$Type-II = 2WO_3 + 3Zr_{Zr}^{\times} \rightarrow 2W_{Zr}^{\bullet\bullet} + V_{Zr}^{////} + 3ZrO_2 \qquad (6.2)$$

$$Type-III = WO_3 + Zr_{Zr}^{\times} \rightarrow W_{Zr}^{\bullet\bullet} + O_i^{//} + ZrO_2 \qquad (6.3)$$

To calculate the defect energies of the systems, different configurations of defect clusters were created by locating the cationic defects near or away from the oxygen vacancy. For Type I, two pairs were created, 1) Tungsten as the nearest neighbour defect (NN) to oxygen vacancy and 2) Tungsten as the next nearest neighbour (NNN) to oxygen vacancy as shown in Figure 6.8. For Type II defects, the three different configurations proposed were two tungsten atoms next to each other, while two tungsten atoms away from each other. For Type III the configuration included placing a tungsten atom on the NN and NNN positions to the oxygen interstitial. The isolated defect energies of vacancy, interstitial and substitution were also calculated in the bulk. The computed defect energies are shown in the Table 6.5 below. It was found that the values converged for Type –I and II- NN type defects using a 4x4x4 supercell but in all other cases the convergence occurred

after growing the supercells to 5x5x5 size. The convergence plot of defects energies for Type-I defects is shown in Figure 6.9.

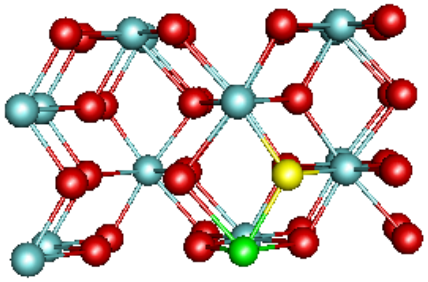

(a) Nearest Neighbouring position

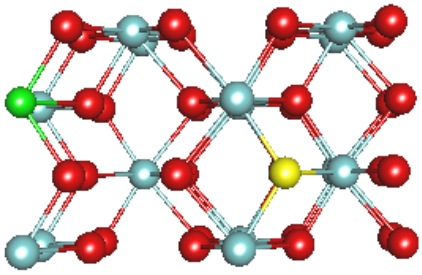

(b) Next Nearest Neighbouring position

Figure 6.8 Schematic diagrams for the NN and NNN sites of tungsten with respect to the oxygen vacancy. (Zirconia ; Oxygen ; Tungsten ; Oxygen vacancy)

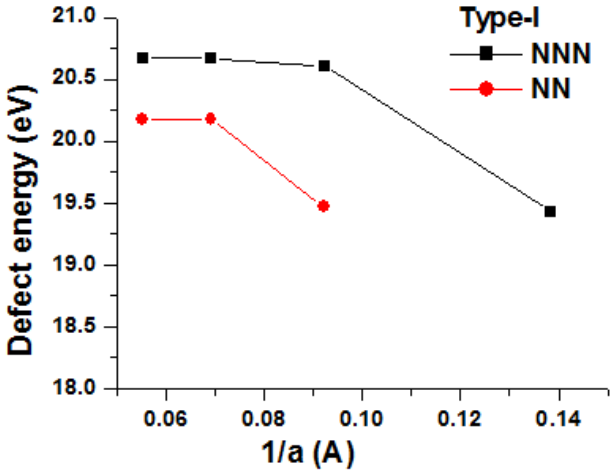

Figure 6.9 The defect convergence plot for Type I defect on t-ZrO_2.

The lowest energy configuration will favour the formations most likely to occur in the bulk. In the Type I configuration it was observed that the NN site to the oxygen vacancy was the most preferred location for the tungsten defect. In Type II also the most stable was found to be NN with respect to the zirconia vacancy. In Type III however the most stable was NNN configuration with respect to oxygen interstitial. From the table the Type III defect is the least preferred type of defect to exist within the crystal structure. According to the data the lowest value of defect energy per defect is found for Type I (NN). Earlier studies too have already confirmed the presence of oxygen vacancies in ZrO_2. [40] Thus it could be concluded that Type I (NN) would be the most preferred location for a tungsten addition in the bulk zirconia.

Table 6.5 Calculated defect energies for bulk t-ZrO_2

Defect Configurations	Total energy gained/lost in the reaction in NN types in eV	Total energy gained/lost in the reaction in NN types in eV per defect	Total energy gained/lost in the reaction in NNN types in eV	Total energy gained/lost in the reaction in NNN types in eV per defect
Type I	-6.51	-1.62	-6.05	-1.51
Type II	-7.82	-1.56	-7.57	-1.51
Type III	-2.29	-0.76	-3.53	-1.17

Table 6.6 Calculated Solution energies for bulk t-ZrO_2

Defect Configurations	Solution energy in NN types in eV.	Solution energy per defect in NN types in eV.
Type I	8.45	2.11
Type II	11.62	2.32
Type III	7.65	2.55

Although Type I (NN) is shown to be favourable, the formation of such defect in bulk could be checked by calculating the solution energy in bulk as shown in Eq (6.4). These values will indicate the ease of substituting this defect within the lattice matrix of bulk t-ZrO_2. Depending on the defect type, the equation also needs to be balanced. This balance is done for Type I and II defects as shown the Eq (6.5) and (6.6), for Type III it is the same as Eq (6.4).

$$E_{Sol} = [E_{def.surf} + E_{latt.energy\ of\ bulk-ZrO_2}] - [E_{pure.surf} + E_{latt.energy\ of\ bulk-WO_3}] \quad (6.4)$$

For Type-I

$$E_{Sol} = [E_{def.surf} + 2xE_{latt.energy of\ bulk-ZrO_2}] - [E_{pure.surf} + E_{latt.energy of\ bulk-WO_3}] \quad (6.5)$$

For Type-II

$$E_{Sol} = [E_{def.surf} + 3xE_{latt.energy of\ bulk-ZrO_2}] - [E_{pure.surf} + E_{2xlatt.energy\ of\ bulk-WO_3}] \quad (6.6)$$

The calculated solution energy values as shown in Table 6.7, indicates that the lowest energy values per defects were obtained for the Type I (NN). However in all cases the positive values of solution energies obtained indicates the less favourability for these defects to get substituted with in the lattice of bulk t-ZrO_2. Now to check whether these defects would to prefer to stay in bulk or will migrate to a surface; the segregation energies were estimated. For doing this, the Type I defect was placed on the different surfaces of t-ZrO_2 and the segregation energy was evaluated. The segregation energies were calculated as described in section 2.3.9.1 of Chapter 2. Since the Type I (NN) defect was found to be the most preferable one in bulk, this same defect was placed on the various surfaces of t-ZrO_2.

Table 6.8 Segregation and solution energies of Type-I (NN) defects on surfaces

Surface	**Segregation Energy per Defect (E_{seg}) eV**	**Solution Energy (E_{sol}) eV**
{101}	-0.42	6.74
{001}	-0.77	5.36
{100}	-1.71	1.6
{110}	-2.29	-0.72
{111}	-4.79	-1.64

The values from Table 6.8 concludes that the segregation towards all surfaces were favourable due to the negative values of segregation energies obtained for all surfaces. Even though these values indicate the preference of these defects to segregate to the surface from bulk, the solution energy values obtained for this indicate the relative preference for a particular surface over the others for the defects to segregate. It could be deduced that the segregation could be in the following order : {111} > {110} > {100} > {001} > {101}. Using the Type I defect configuration, the tungsten atom was also moved away from the surface towards the bulk in increasing depth, keeping the other defects at the same position. This will also give a relative idea about the effects of moving defects towards the bulk from the surface. A graph was plotted with the segregation energy versus the defect depth on the {110} surface as shown in Figure 6.10. It was noted that moving the tungsten atom away from the surface resulted in more unstable energy values. This indicates tungsten's preference to stay on the surface of t-ZrO_2 rather than in the bulk.

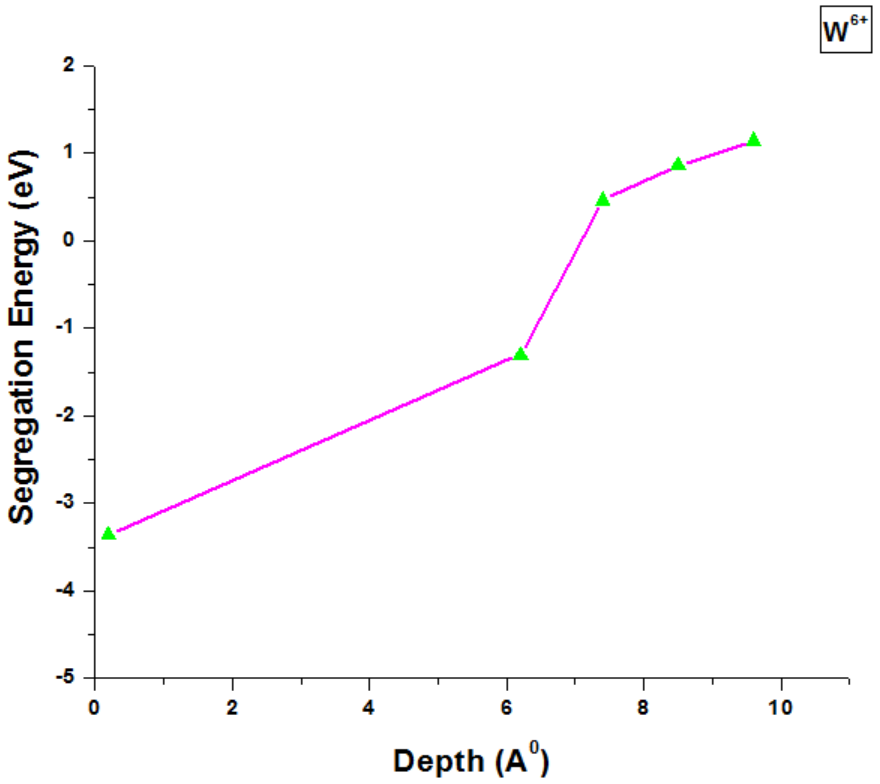

Figure 6.10 Segregation energy of W^{6+} as a function of defect depth.

6.6 Conclusion

This chapter successfully provided some basic concepts of defect reactions for both bulk and surfaces of t-ZrO_2. The study clearly indicates that the natures of the defect reactions are different on surface from the bulk. In the bulk t-ZrO_2 a Schottky mechanism is the most preferable, however on the surface this entirely depended on the type of the surface considered. The addition of different cations to the surface {110} of t-ZrO_2 noted its capability to either increase on decrease the activation energy barrier for oxygen migration. It was concluded here that, the smaller the cation size the higher will be its

capability to reduce the oxygen migration barrier. W^{6+} was found to be the best one capable of reducing the barrier among all the other cations studied here. These results prompted us to look further in to the mechanism of tungsten addition to the bulk and surfaces of zirconia. It was inferred that tungsten atom will segregate to the surface and not stay in the bulk. This motivates us to explore the next chapter were the different types of WO_3 species are investigated on the surfaces of t-ZrO_2.

6.5 References

[1] J.H.J. Crawford, L.M.Slifkin, *Point Defects in Solids*, Plenum, New York and London, 1972.
[2] J. Frenkel, *Z.Phys.* 35 (1926) 625.
[3] H.T.A.S. Bishop, *Annu. Rev. Mater. Res.* . 41 (2011) 269.
[4] M. Youssef, B. Yildiz, *Physical Review B*. 86 (2012).
[5] B.Y. A. Cheroneos, A. Tarancon, D. Parfitt, and J. Kilner, *Energy and Environ. Sci.*, 4 (2011) 2774.
[6] W.C. Maskell, *Solid State Ionics*. 134 (2000) 43.
[7] C.L. U. Schulz, K. Fritscher, M. Peters, B. Saruhan-brings,, J.M.D. O. Lavigne, M. Poulain, R. Merval, and M. Caliez, *Aeroscpace Sci. Technol*. 7 (2003) 73.
[8] E. B. A. Yilmazbayhan, A. T. Motta, and R. J. Comstock, *J.Nuc. Mat.* 349 (2006) 265.
[9] D.D.M.a.G. Engelhardt, *ECS Trans*., 28 (2010) 123.
[10] M. U.-M. Y. Chen, D. D. Macdonald, *J. Nucl.Mater*. 348 (2006) 133.
[11] E. J .G. Jackson N B, *J.Catal*. 126 (1990) 31.
[12] F.W. Keim W, *Catal Lett.* 3 (1989) 59.
[13] A. K. Qingjie Ge, A. C. Roger, Wenzhao Li, Hengyong Xu, Journal of Natural Gas Chemistry. 13 (2004) 41.
[14] G.R. M. Dudek, W. Bogusz, A. Kozlowska-Rog, M. Bucko, Ł. Zych, *Materials Science-Poland*. 24 (2006).
[15] A.J.M. J. Van Herle, K. R. Thampi, *J. Mat. Sci*., 29 (1994) 3691.
[16] J. D. Gale, *J. Chem. Soc., Faraday Trans*., 93 (1997) 629.
[17] G.W. Watson, Kelsey, E.T., de Leeuw, N.H., Harris, D.J. and Parker, S.C., *J. Chem. Soc., Faraday Trans*., 92 (1996) 433.
[18] M. Kilo, R. Jackson, G. Borchard, *Philos. Mag*., 83 (2003) 3309.
[19] P.W. Oleksandr I. Malyi, Vadym V. Kulish, Kewu Bai, Zhong Chen, *Solid State Ionics*. 212 (2012) 117.
[20] D. M. Duffy, P. W. Tasker, AERE Report No. Rl105(1983).
[21] S. E. Redfern, R. W. Grimes, R. D. Rawlings, *J. Mater. Chem*., 11 (2001) 449.
[22] C. Pirovano, M. S. Islam, R. Vannier, G. Nowogrocki, G. Mairesse, *Solid State Ionics*, 140 (2001) 115.
[23] A. Dwivedi, A., A. N. Cormack, A. N., *Philos. Mag. A*, 61 (1990) 1.
[24] L. Minervini, M. O. Zacate, R. W. Grimes, *Solid St. Ionics*, 116 (1999) 339.
[25] G. V. Lewis, G. V., C. R. A. Catlow, *J. Phys., C*, 18 (1985) 1149.
[26] S. M. Woodley, P. D. Battle, J. D. Gale, C. R. A. Catlow, *Phys. Chem.Chem. Phys*., 1 (1999) 2535.
[27] J. Kim, S. Lee, K.H. Kang, H.S. Hong, *Int. J. Energy Res*., 34 (2010) 438.
[28] J. J. Zhu, S. Albertsma, J. G. van Ommen, L. Lefferts, *J. Phys. Chem. B*, 109 (2005) 9550.
[29] X. Q. Cao, R. Vassen, D. Stoever, *J. Eur. Ceram. Soc*. 24 (2004) 1.
[30] N. Q. Minh, *J. Am. Ceram. Soc*. 76 (1993) 563.
[31] A. Atkinson, S. Barnett, R. J. Gorte, J. T. S. Irvine, A. J. McEvoy, M. Mogensen, S. C. Singhal, J. Vohs, *Nat. Mater*., 3 (2004) 17.

[32] R.M. Ormerod, *Chem. Soc. Rev*., 32 (2003) 17.
[33] S. P. Jiang, S. H. Chan, *J. Mater. Sci*., 39 (2004) 4405.
[34] D. G. Lamas, M. F. Bianchetti, M. D. Cabezas, N. E. W. de Reca, *J. Alloys Compd*., 495 (2010) 548.
[35] H. Kim, C. Lu, W. L. Worrell, J. M. Vohs, R. J. Gorte, *J. Electrochem. Soc*., 149 (2002) A247.
[36] S. Menad, P.Ferreira-Aparicio, O. Cherifi, A. Guerrero-Ruiz, T. Rodriguez-Ramos, *Catal.Lett*., 89 (2003) 63.
[37] P. Li, I-W. Chen, *J. Am. Ceram.Soc*, 77 (1994) 118.
[38] P. Li, I-W. Chen, J. E. Penner-Hahn, *Phys. Rev. R*, 48 (1993) 10074.
[39] P. Li, I-W. Chen, J. E. Penner-Hahn, *J. Am. Ceram.Soc*, 77 (1994) 118.
[40] G. Stefanic, S. Music, *Croat. Chem. Acta*, 75 (2002) 727.
[41] P. D. L. Mercera, J. G. Ommen, E. B. M. Doesburg, A. J. Burggraaf, J. R. H. Ross, Applied Catalysis, 78 (1991) 79-96

Chapter 7 Tungstated Zirconia

"The meeting of two personalities is like the contact of two chemical substances: if there is any reaction, both are transformed."

— C.G. Jung

7.1 Introduction

Tungstated zirconia (WO_3-$ZrO_{2)}$ is one of the robust catalysts used by experimentalists for its application in isomerisation of light alkanes (C4-C8). [1-7] Hino and Arata were the first to discover the unique properties of the WO_3-ZrO_2 catalyst, which were tested for propane and butane reactions. [8, 9] Although less active than sulfated zirconia [10, 11] catalysts, the enhanced thermal stability and resistance in hydrogen, oxygen and water atmospheres of WO_3-ZrO_2 materials offer an alternative catalyst for many practical industrial applications. [12, 13] Extensive experimental studies have been devoted in the past to the preparation and structural characterization of WO_3-ZrO_2 catalysts. [14, 15] However, its higher thermal stability compared to its sulphated forms, is still much debated because of the several different types of surface species that co-exist. [16, 17] Since this catalyst serves as an alternate catalyst for many industrial applications, it is worth looking in detail at this existing species and the role of the structure-property relationships of the catalyst. Depending on the synthesis method adopted, the surface

species on WO_3-ZrO_2 have been found to exist in different forms. [18-24] Electron microscopy studies [25] suggested the presence of four types of species, a) mono tungstate species b) polytungstate species c) well ordered WO_3 nanocrystals and d) WO_x distorted clusters containing zirconia atoms. It was postulated that the formation of polytungstate and WO_3 clusters as well the Zr-WO_3 distorted clusters play an important role in catalysis. Here, we report the results of a the molecular dynamics study of WO_3-ZrO_2 systems to look if these key species could be detected using simulation.

To date no computer modelling techniques have been applied to look into all the possible mechanism of adsorption of WO_3 species on ZrO_2 surfaces. Hence we attempt to study the distribution of WO_3 species on to the different surfaces of t-ZrO_2. This kind of understanding provides a tool for improving the performance of the catalyst. We begin our studies on the pure low miller index surfaces.

7.3 WO_3 loading on the t-ZrO_2 Surfaces

Since catalytic reactions occur on surfaces, [26-30] monitoring the role of WO_3 on various surfaces of zirconia will give us an idea of its preference to a particular surface. The earlier spin polarized DFT studies done on cubic zirconia supports predicted its catalytic properties by studying the adsorption energy values of Cu, Ag and Au atoms on the {111} surface. The highest adsorption energy values were obtained for Cu on this surface. [31]

Similarly the hydroxylation energies on the surfaces of t-ZrO_2, were analysed by calculating its adsorption energy at various low index surfaces. [32] Both these studies calculated the adsorption energy as the difference between the energy of the slab with the dopant atom adsorbed and the sum of the energies of the clean oxide surface and the isolated dopant atom. Thus it is clear that the preference of the dopant to a particular surface can be analysed by considering the adsorption energies associated with attaching WO_3 species on to zirconia surface. A negative adsorption energy indicates an exothermic reaction. However, the presence of negative adsorption energy doesn't normally indicate that the reaction of adding the dopant is favourable. It is also important to check if the surface energies of the adsorbed surface have lowered in comparison with the pure surface, or else the possibility of such a surface existing is reduced. Hence, in this study we are considering both parameters in order to determine the most favourable mechanism.

This is the first attempt to study the adsorption of WO_3 on t-ZrO_2 surfaces using molecular dynamics. Slabs of different loadings of WO_3 on the low index oxygen terminated surfaces of zirconia were set up. Oxygen terminated surfaces were chosen as it has been shown in Chapter 5 that they are more than stable and also because it provides a simple method for adding WO_3 units to the surface. The WO_3 groups were added such that the tungsten atoms from the WO_3 groups were kept at least 2 Å above the surface oxygens of t-ZrO_2. This study focuses mainly on 20% and 50% monolayer coverages of WO_3 groups on t-ZrO_2 surfaces. 20% coverage results in addition of 10 atoms of tungsten

and corresponding 30 atoms of oxygen on to the surfaces of t-ZrO_2. A 50% monolayer coverage results in the addition of 32 atoms of tungsten and 96 atoms of oxygen on the surface. Both 20% and 50% coverage are defined here based on the maximum number of tungsten (W^{6+}) atoms that could be added on to the surface which is 64 which represents 100% coverage. The addition of WO_3 groups was done in such a way that the WO_3 species were positioned nearest neighbours to each other or positioned far away from each other. This was done to determine if the nearest WO_3 species showed any signs of polytungstate or cluster formation and if this was observed it was a genuine effect and not on the effect of the simulation starting configuration. A vacuum separation of 60 Å thick was set between the two periodically repeated slabs and each slab was symmetrical to avoid dipole-dipole interactions. The structure was run at various temperatures from 300 K and 2500 K for 1 million steps with 0.1 fs (femto second) timestep using an NVT ensemble. In all simulations, the temperature is kept constant using the Nosé-Hoover thermostat [33, 34], and the Verlet-Leapfrog algorithm [35] was used to generate the trajectories. The simulation was monitored using the VMD analysis software, [36] from which the structural changes occurring at different timesteps could be recorded. A comparison of the adsorption energy and surface energy of all surfaces with WO_3 at temperatures between 300 K till 2500 K were made with the pure surfaces to check their relative stability. Adsorption energies are denoted as E_{ad} and surface energies as γ.

The surface energies have been calculated using the following formulae:

$$\gamma = \frac{E_{Surf} - E_{Equiv-bulk} - nE(WO_3)}{2A} \qquad (7.1)$$

The adsorption energies of tungstated surfaces were calculated as follows:

$$E_{ad} = \frac{E_{Surf}(WO_3) - E_{Surf}(pure) - nE(WO_3)}{n} \qquad (7.2)$$

Here E_{surf} is the total energy of the surface slab and $E_{equiv\ bulk}$ is the total energy of the bulk zirconia with equivalent number of atoms.The surface area is denoted as A and γ is divided by two because each slab has two equivalent surfaces and n is the number of tungsten atoms added on to the surface.

7.3.1 *{101} Surface*

In Chapter 5 it was concluded that this surface is the most stable surface of t-ZrO_2. The 20% monolayer structures were set up on this surface as discussed earlier. Analysing the structural rearrangements on the 20% coverage after running the simulation, it showed that the WO_3 groups which began as NN moved away from each other. These WO_3 groups began with the W-W distance to be about 3.6 Å, but in the optimized structure this separation increased to 4.34 Å. There was also no evidence of polymerisation occurring between any pair of WO_3 groups at this coverage. It can also be noted that the WO_3 species distorted during the relaxation, resulting in an increase in bond angles between O-W-O which varied between 30º to 35º for O-W-O atoms as shown in Figure 7.1. This

relaxation resulted in the shortening of the bond distance between the WO_3 species and the surface atoms of zirconia. The surface relaxations for atoms below the surface was found to be in the range of 0.1-0.2 Å from their equilibrium positions. Increasing the temperatures resulted in the displacements of surface atoms even as high as 10-15 Å.

We then studied the behaviour of {101} surface with a 50% monolayer coverage. These were setup by introducing a polymerised WO_3 species on to the surface. The polymerised WO_3 species were kept parallel to each other and each layer was separated from the other to check if any polymersation will occur between adjacent layers as shown in the Figure 7.2. After structural relaxation during the MD simulation, it was noted that three of the polymerised chains broke up giving rise to several dimers and monotungstate species, while one of the WO_3 chain remained as a tetramer; however no polymerization occurred between the adjacent WO_3 chains. The distance between the adjacent W atoms of the WO_3 groups increased from 1 Å to 2 Å. The tilting of WO_3 species was also observed here and this was similar to the 20% monolayered surface. The increase in bond angle varied between O-W-O from 18º and 35º.

The breaking up of polymer chains resulting in dimers, trimers and monomers were also observed at temperatures up to 1500 K. However, at 2000 K it was observed that surface zirconia atoms moved away from the surface forming a bridge between two WO_3 groups. The breaking up of the polymer chains up to 1500 K is indicative of instabilities occurring with in the adsorbed structure, which means that addition of WO_3 species may not be favourable.

This was investigated further by calculating the surface and adsorption energies after the MD run. Table 7.1 gives the adsorption and surface energies for both coverages. The calculated values indicate that the addition of WO_3 species both at 20% and 50 % monolayer coverages resulted in an increase of surface energies at 300 K compared to the pure surface values. The surface energies of their pristine surface were found to be much lower than both coverages, which would mean this surface will be unstable to the addition of WO_3 species. The percentage of rise in surface energies from their pristine surface was estimated around 8 % for the 20 % coverages and around 28 % for the 50 % coverages.This result was further strengthened by the positive values of adsorption energies obtained on both coverages. Negative adsorption energy values were obtained for 20% coverages along with a slight decrease in surface energies at relatively higher temperatures around 2000 K and above. This could mean that getting closer to the pre-melting temperatures, the presence of WO_3 groups helps to stabilise this surface and retain its tetragonal form. However, the increase in WO_3 coverages is not favourable even at higher temperatures. Therefore it could be concluded here that the relative stability of the pure {101} surface at low temperatures makes the additions of the WO_3 species unfavourable.

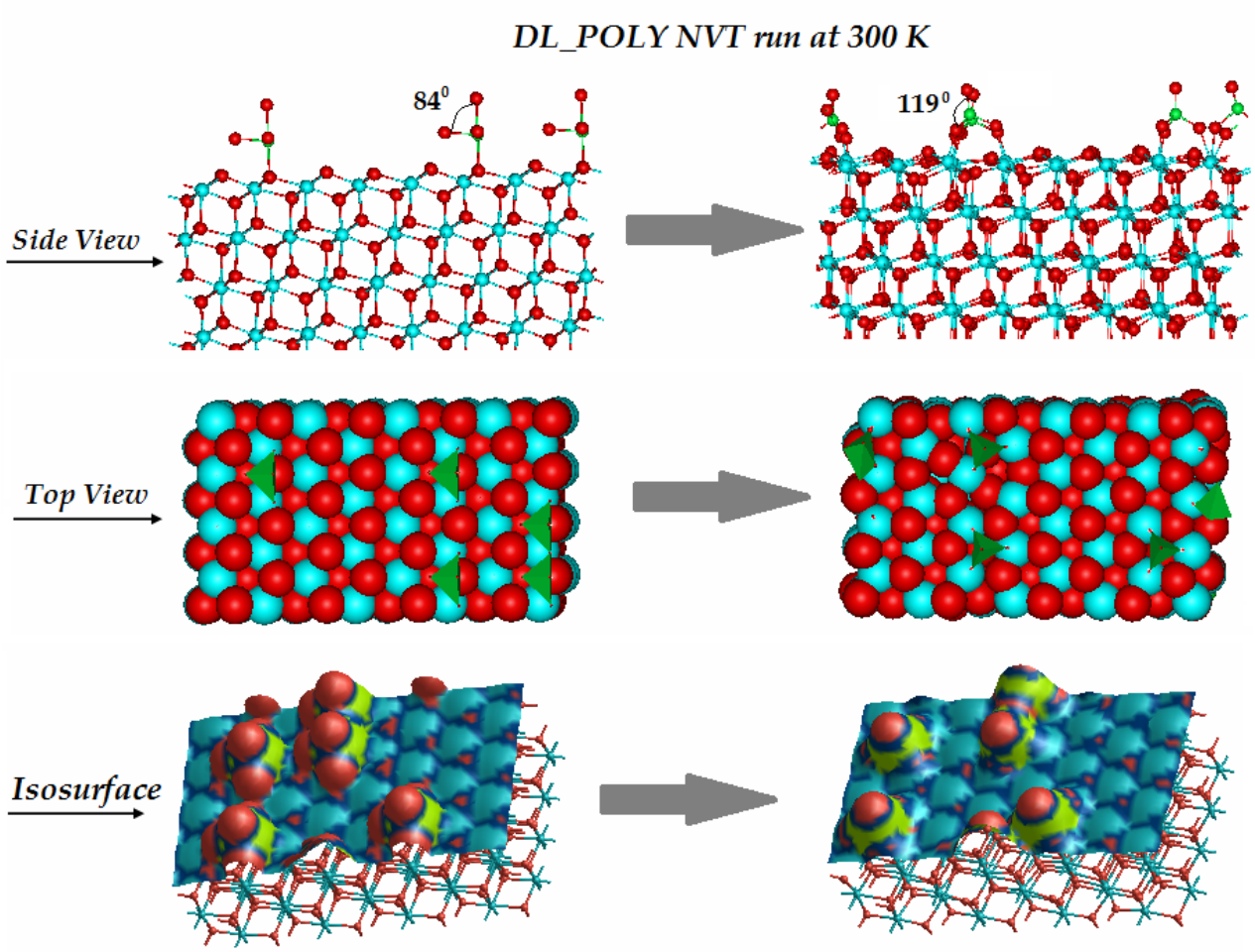

Figure 7.1 The structural changes occurring on the 20% monolayered tungstated {101} surface after a MD run at 300 K.

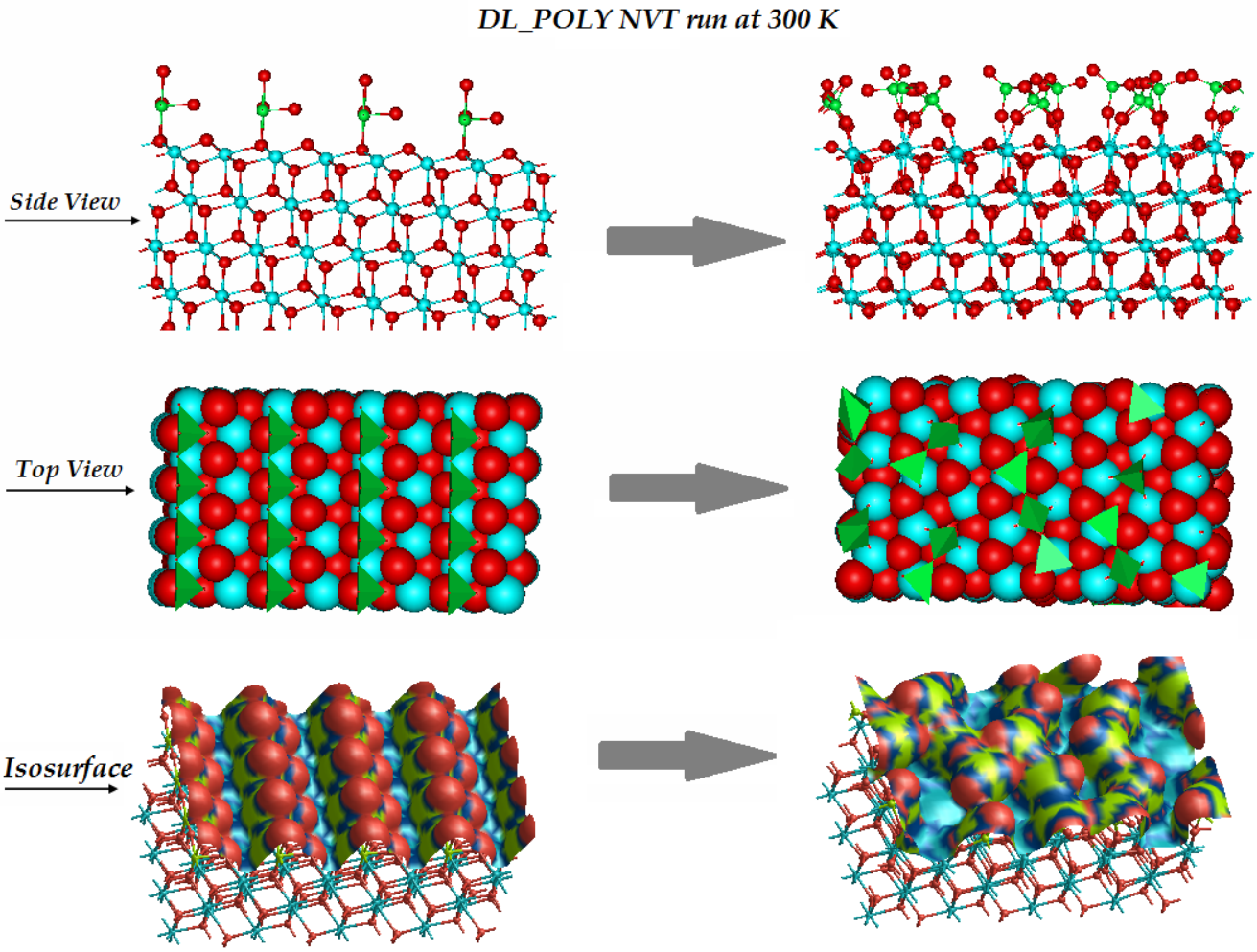

Figure 7.2 The structural changes occurring on the 50% monolayered tungstated {101} surface after a MD run at 300 K.

Table 7.1 Adsorption and Surface Energies on {101} Surface

Surface {101}	Pure	20 % Coverage		50 % Coverage	
Temperature	γ (J/m^2)	γ(J/m^2)	E_{ad} (eV)	γ(J/m^2)	E_{ad} (eV)
300 K	1.79	1.94	0.7	2.26	0.66
700 K	1.78	1.81	0.12	2.26	0.68
1000 K	1.77	1.86	0.41	2.19	0.59
1200 K	1.76	1.88	0.54	2.18	0.60
1500 K	1.76	1.79	0.14	2.16	0.57
2000 K	1.75	1.66	-0.39	2.15	0.58
2500 K	1.73	1.57	-0.74	2.14	0.58

7.3.2 *{001} Surface*

The WO_3 groups added at 20 % and 50 % coverages on this surface were evaluated at various temperatures and compared with the pure surface. Just as in the case of the {101} surface, for the 20 % coverages the WO_3 groups moved apart from each other and remained as monotungstate species. The distance between the tungsten atoms of adjacent WO_3 groups increased from 3.6 Å to 5 Å after the simulation. The distortion of the WO_3 groups were also noted here, the increase in bond angles for O-W-O are between 10º and 20º see Figure 7.3. It was also noted that after the surface relaxations at 300 K, one of the WO_3 group moved atleast 2 Å away from the surface. The reconstructions within the bulk where around 0.1 to 0.2 Å.

For the 50% coverages although the polymerised WO_3 layer retained much of its initial character after the simulation, it was noted that few of WO_3 groups moved away from the surface and formed W-O-W-O linkages (see Figure 7.4). At these stage the WO_3 groups resembled like that of a WO_3 bulk structure on zirconia and the distance between the W-O-W linkages were around 3.8 Å. This value is equal to the W-O-W bond distance of WO_3 bulk structure obtained by carrying out a NPT simulation using Mairesse *et al*. potential (See Table 3.2 of Chapter 3). The atoms within the bulk t-ZrO_2 showed a relaxation of around 0.02 Å from their equilibrium positions after simulation. On increasing the temperature it was observed that more WO_3 groups move further away from the surface forming three dimensional WO_3 bulk like networks. From the values in

Table 7.2 all the adsorption energies are positive for both coverages at all temperatures. The surface energies also increased with the increase in WO_3 coverage. For the pure surface the surface energy values were 2.34 J/m^2, while this increased to 2.61 J/m^2 and 3.36 J/m^2 for 20 % and 50 % coverages at 300 K respectively. Thus an approximate rise in surface energies after tungstating are estimated to be 11 % for 20 % coverages and 48 % for 50% coverages compared to the pure surface. Thus both these values indicate that the addition of WO_3 to this surface reduces its stability when compared to its pure surface.

The effect of increase in temperature resulted in a drop of surface as well as adsorption energies for tungstated surfaces of both coverages. For 20 % coverages the drop in surface energies were noted at 1000 K and above and the varied in 1 % and 8 % from their respective surface energy values at 300 K. In the case of 50 % coverages the drop in surface energies were noted from 1500 K and above. The surface energies in this case dropped between 1 % and 4 % of its values at 300 K. However, in all cases the surface energies of the tungstated surface always remained higher than that of its pure surface. Although the formation of three dimensional bulk like networks were found on this surface, the adsorption and surface energies were not in favour of WO_3 addition. This leads us to conclude that such a surface will not be capable of accommodating any WO_3 groups and hence this surface is not favourable to WO_3 addition.

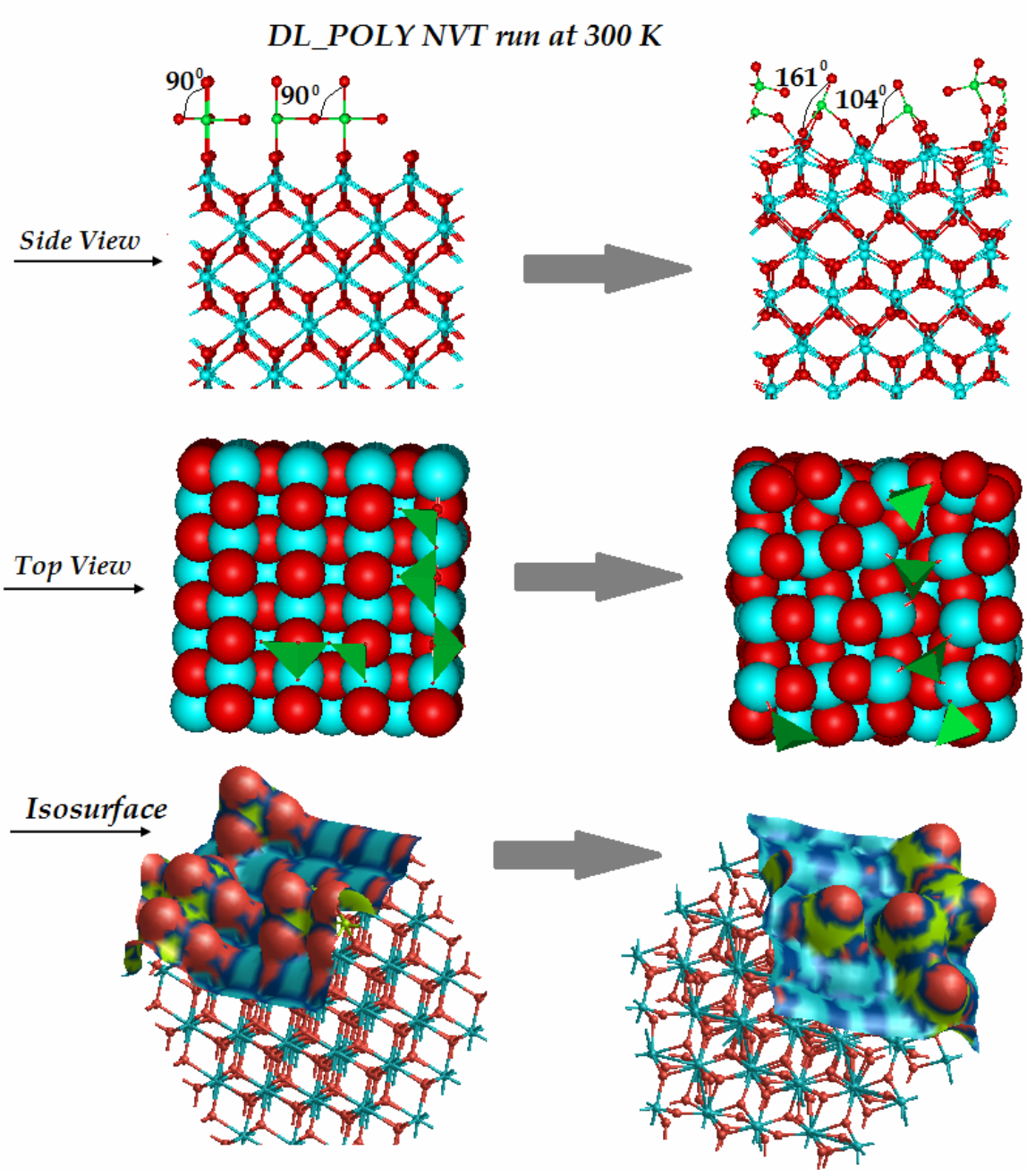

Figure 7.3 The structural changes occurring on the 20% monolayered tungstated {001} surface after a MD run at 300 K.

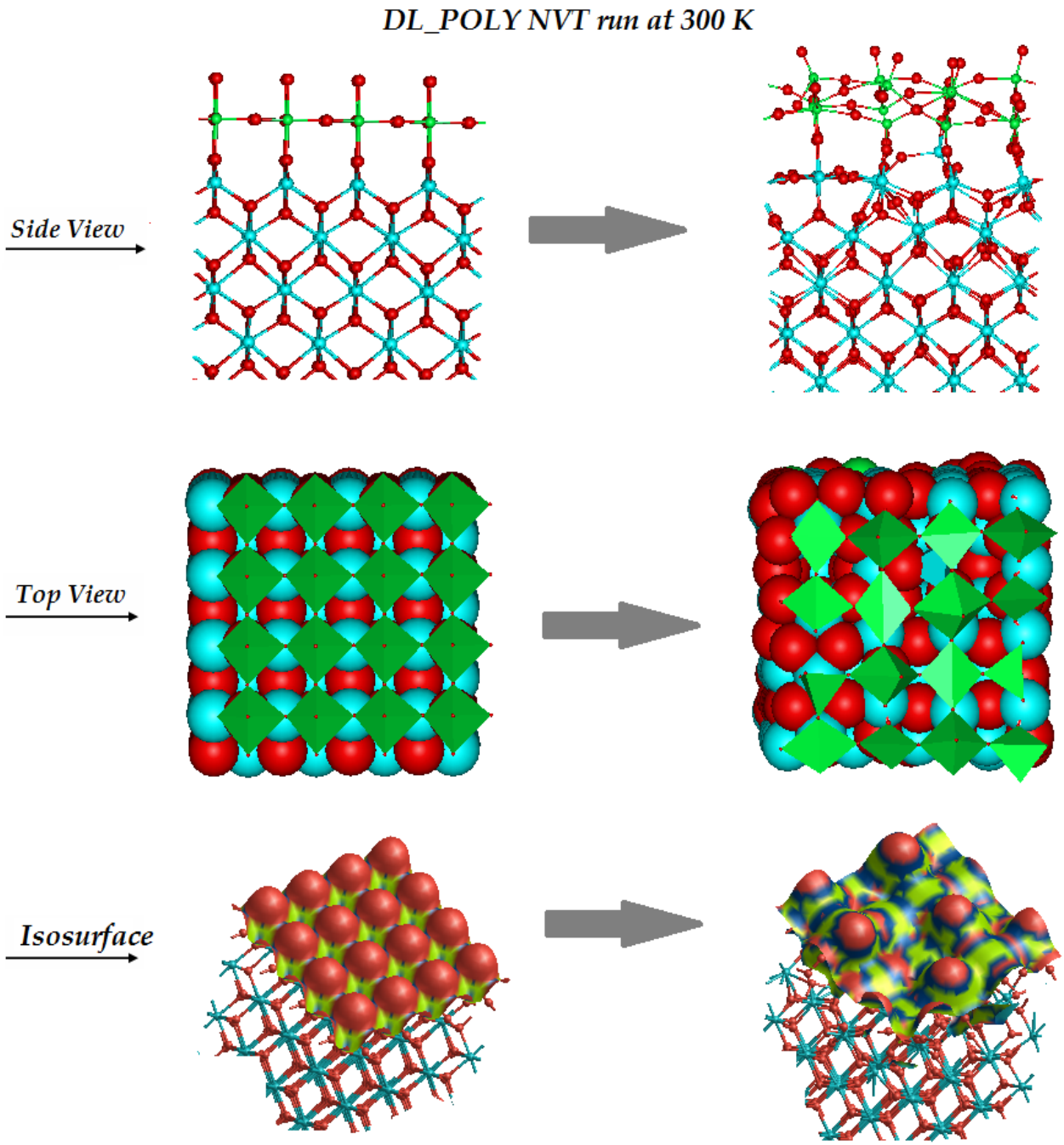

Figure 7.4 The structural changes occurring on the 50% monolayered tungstated {001} surface after a MD run at 300 K.

Table 7.2 Adsorption and Surface Energies on {001} Surface

Surface {001}	Pure	20% Coverage		50% Coverage	
Temperature	γ (J/m^2)	γ(J/m^2)	E_{ad} (eV)	γ(J/m^2)	E_{ad} (eV)
300 K	2.34	2.61	0.78	3.36	0.83
700 K	2.33	2.71	0.99	3.51	0.96
1000 K	2.35	2.58	0.59	3.75	1.14
1200 K	2.19	2.56	0.96	3.48	1.05
1500 K	2.18	2.42	0.61	3.28	1.09
2000 K	2.29	2.49	0.54	3.33	1.04
2500 K	2.28	2.39	0.27	3.23	0.77

7.3.3 *{100} Surface*

After the MD run for the 20 % monolayered slab on the {100} surface, it was noted that the three adjacent WO_3 groups that began as NN moved away from each other forming three monotungstate species. This movement resulted in the distance of adjacent tungsten atoms between the WO_3 groups which were 3.6 Å apart before the reconstruction to be separated between 5.5 Å and 7.9 Å. However, it was also noted that two of WO_3 groups formed a dimer and the W-O-W bond lengths for this was ~ 4 Å. A distortion of WO_3 groups was also observed here and the increase in O-W-O bond angles varied between 11º and 17º see Figure 7.5.

For the 50% monolayered slab it was noted that after relaxation most of the WO_3 polymerised chain didn't break up, only two WO_3 groups remained as monotungstate, the rest all retained their polymerized structure. Even the adjacent chains polymerised with each other giving rise to a polytungstate network, see Figure 7.6. One of the WO_3 groups on the surface moved 3 Å away from its initial position to form a cluster. It was noted that increase in the temperature favoured the formation of more of these kind of species. The surface rexalations also resulted in the zirconium atoms below the surface layer moving inward by 0.01 – 0.3 Å from their equilibrium positions.

The surface energy values from the Table 7.3 indicate that there was a drop in surface energies for both the coverages after the addition of WO_3 groups. This drop is approximately 15 % for 20 % coverages and 22 % for 50 % coverages at 300 K. The 50% coverages showed the lowest surface energies at 300 K, however increasing temperatures resulted in instability at this coverages. The preference of WO_3 addition on to this surface at lower temperature is further supported by the negative adsorption energy values obtained for both coverages. The adsorption energy values were found to be more negative for 20 % than for 50 % coverages. For the 20 % monolayer coverages the adsorption energies were negative throughout the temperature range. For 50 % coverages, the values of adsorption energies continued to remain negative until 1500 K after which they become slightly positive. This means that if there are sufficient WO_3 groups present the possibility to form 50 % coverages at and below 1500 K is possible for this surface but at higher temperatures it becomes unfavourable. At higher temperatures since the surface energies become more unstable for the 50% monolayered slabs, the possibility for a stable surface will be the one with 20% coverages. Thus we can conclude that this surface can be stabilised by the addition of WO_3 groups. However, the stability of this surface will depend upon the amount of WO_3 groups added as well as the selected temperature for synthesis.

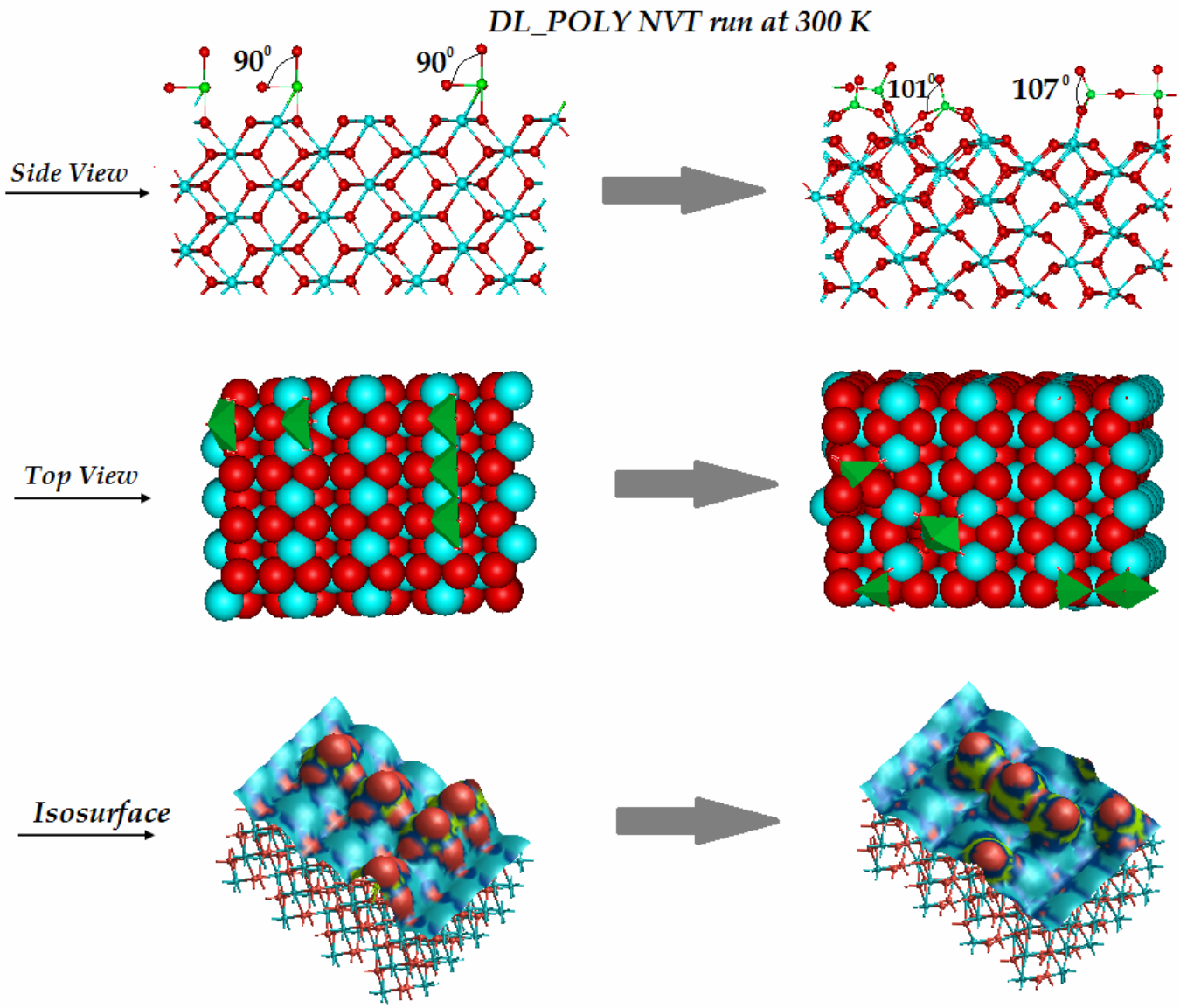

Figure 7.5 The structural changes occurring on the 20% monolayered tungstated {100} surface after a MD run at 300 K.

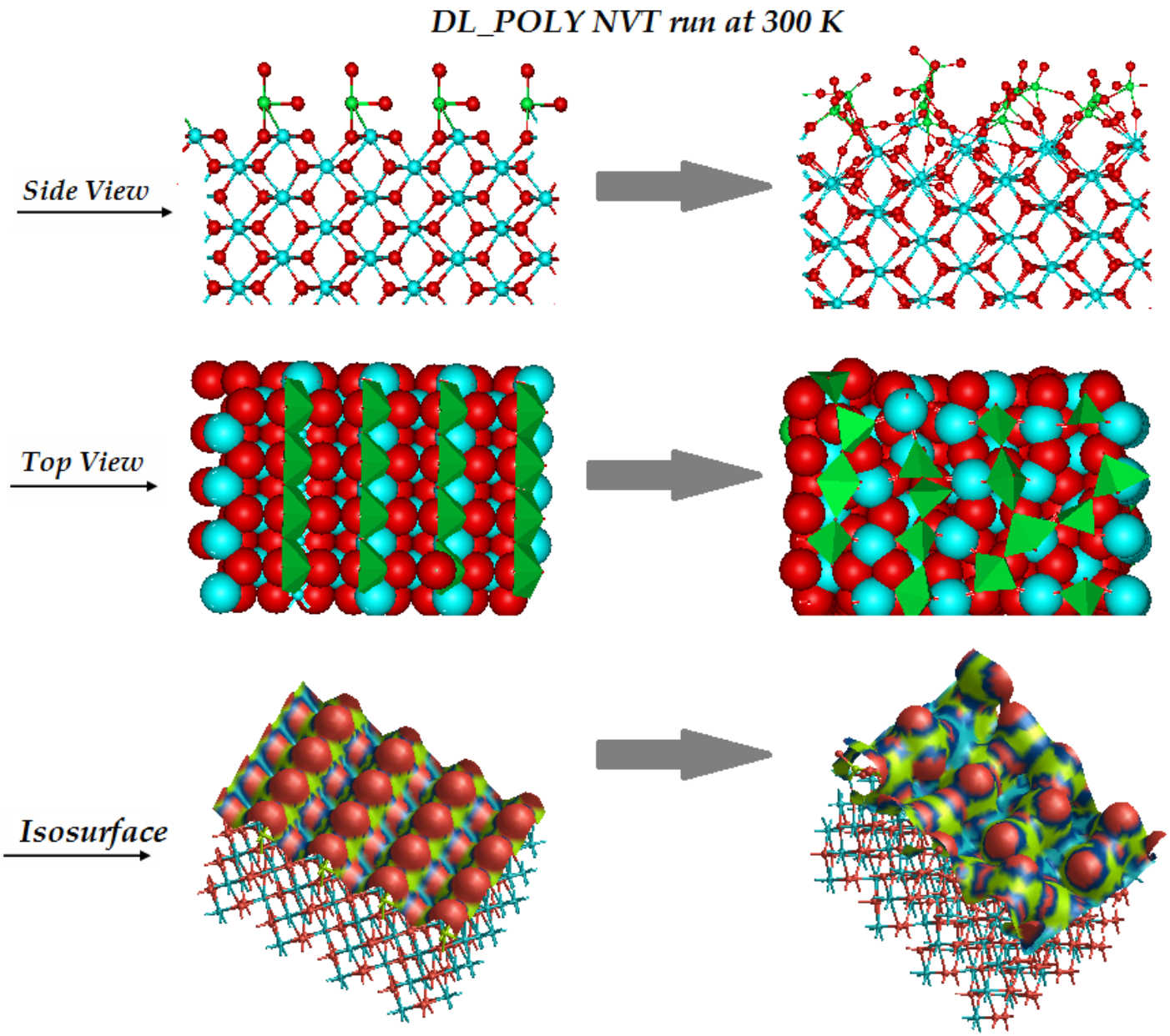

Figure 7.6 The structural changes occurring on the 50% monolayered tungstated {100} surface after a MD run at 300 K.

Table 7.3 Adsorption and Surface Energies on {100} Surface

Surface {100}	Pure	20% Coverage		50% Coverage	
Temperature	γ (J/m^2)	γ(J/m^2)	E_{ad} (eV)	γ(J/m^2)	E_{ad} (eV)
300 K	2.95	2.49	-1.73	2.29	-0.77
700 K	2.94	2.52	-1.56	2.51	-0.50
1000 K	2.93	2.49	-1.66	2.51	-0.49
1200 K	2.93	2.55	-1.43	2.60	-0.39
1500 K	2.93	2.39	-2.01	2.84	-0.10
2000 K	2.95	2.31	-2.39	2.95	0.002
2500 K	2.75	2.37	-1.45	2.48	-0.32

7.3.4 *{110} Surface*

At 20% monolayer coverages it was observed that three of the WO_3 groups stayed as monotungstate species, while two adjacent WO_3 groups polymerised with each other forming a dimer at 300 K see Figure 7.7. The distorting of WO_3 groups observed here resulted in an increase of the O-W-O bond angles which varied between 16º and 31º. As the temperature was increased certain tungsten atoms from the WO_3 groups, moved further away from the surface forming clusters. We also observe that at higher temperatures, some of the surface zirconia atoms moved at least 0.1 Å away from their initial position to form bonds with the oxygens from the WO_3 groups. This resulted in the formation of a Zr-WO_3 cluster type species. Further increase in temperature favoured the formation of more Zr-WO_3 cluster-type species.

Unlike the previous surfaces, it was not possible to add a polymerized chain to the initial configuration of the 50 % monolayer structure because unlike the other surfaces the adjacent atoms were not sufficiently close to each other to form W-O-W linkages. Thus it was not possible to investigate whether a polymerised chain would break up or be retained. However; it is still interesting to investigate any chances of polymerisation taking place between the adjacent WO_3 groups which were added as monomeric species. After the simulation it was noted that the polymerization of WO_3 groups took place on this surface. The formation of a Zr-WO_3 species was also observed at 300 K see Figure 7.8. The increase in temperature resulted in more zirconium atoms from the surface

participating to form Zr-WO_3 species, as well as polytungstate species. This amount of zirconium participation was temperature specific.

From the values in Table 7.4 it was noted that the addition of WO_3 groups to this surface is favourable for both coverages due to the decrease in surface energies and the negative adsorption values obtained on this surface. The drop in surface energy values from their pure surface values were around 4 % for 20 % coverages and 3.6 % for 50 % coverages. For both the monolayer coverages it was noted that the increase in temperatures favoured the decrease in surface energies thus stabilizing the surface on addition of WO_3 species. However it is noticeable that the surface energies of 20 % monolayer coverages were always less than the 50 % values, indicating the higher stability of this surface to lower coverages.

In order to increase our understanding of the stabilization process, the structural changes occurring at various temperature ranges were monitored. Figure 7.9 represents the structural changes occurring with the increase of temperature for both the coverages. For the 20 % monolayer coverage it was noted that at 300 K, there is no formation of Zr-WO_3 species. When the temperature is increased to 700 K, one of the zirconium atoms from the surface forms a bridge between two WO_3 groups, to give rise to zirconium bridged polytungstate species. At 1000 K this zirconium atom moves further away from the surface resulting in a distorted Zr-WO_3 species. Here the W-O-W bond length is found to be in the range of 3.4 Å to 3.8 Å and Zr-O-W length also 3.4 Å to 3.8 Å. These computed bond lengths were also consistent with the experimentally observed values which

indicated the W-O-W bond lengths to be 3.5 Å. [25] At 1000 K there is a 10% decrease in surface energies along with highly negative adsorption energies.

For 50% monolayer coverage we calculated all temperature ranges and the overall surface energies were less stable that the 20 % ones. The values of W-O-W bond length and W-O-Zr bond lengths obtained were similar to these observed at for the 20 % coverage. At 1000 K the adsorption energy became positive and the coverage in surface energy increased. Figure 7.9, a snapshot from the 700 K MD simulation showed a large polytungstate species incorporating bridged zirconium atoms from the surface below. This network of polytungstate species was broken up at 1000 K explaining the less stable energies obtained at this temperature. Further increasing the temperatures to 2000 K showed that more zirconium atoms from surface participated within the WO_3 cluster as well as the polytungstate species. At 2000 K a 6.5 % drop in surface energy with their corresponding values at 300 K have been calculated along with the negative adsorption energy.

Another important aspect to be noted here was that, although no polymerised WO_3 layer was added here, a significant amount of polymeric species were observed after the simulation. It could be concluded that the formation of three dimensional cluster and polytungstate chains along with the participation of zirconium atoms might play a role in the stabilization of this surface. Thus this surface is favourable for the addition of WO_3 species. Although the amount of WO_3 that this surface can accommodate will be temperature dependent.

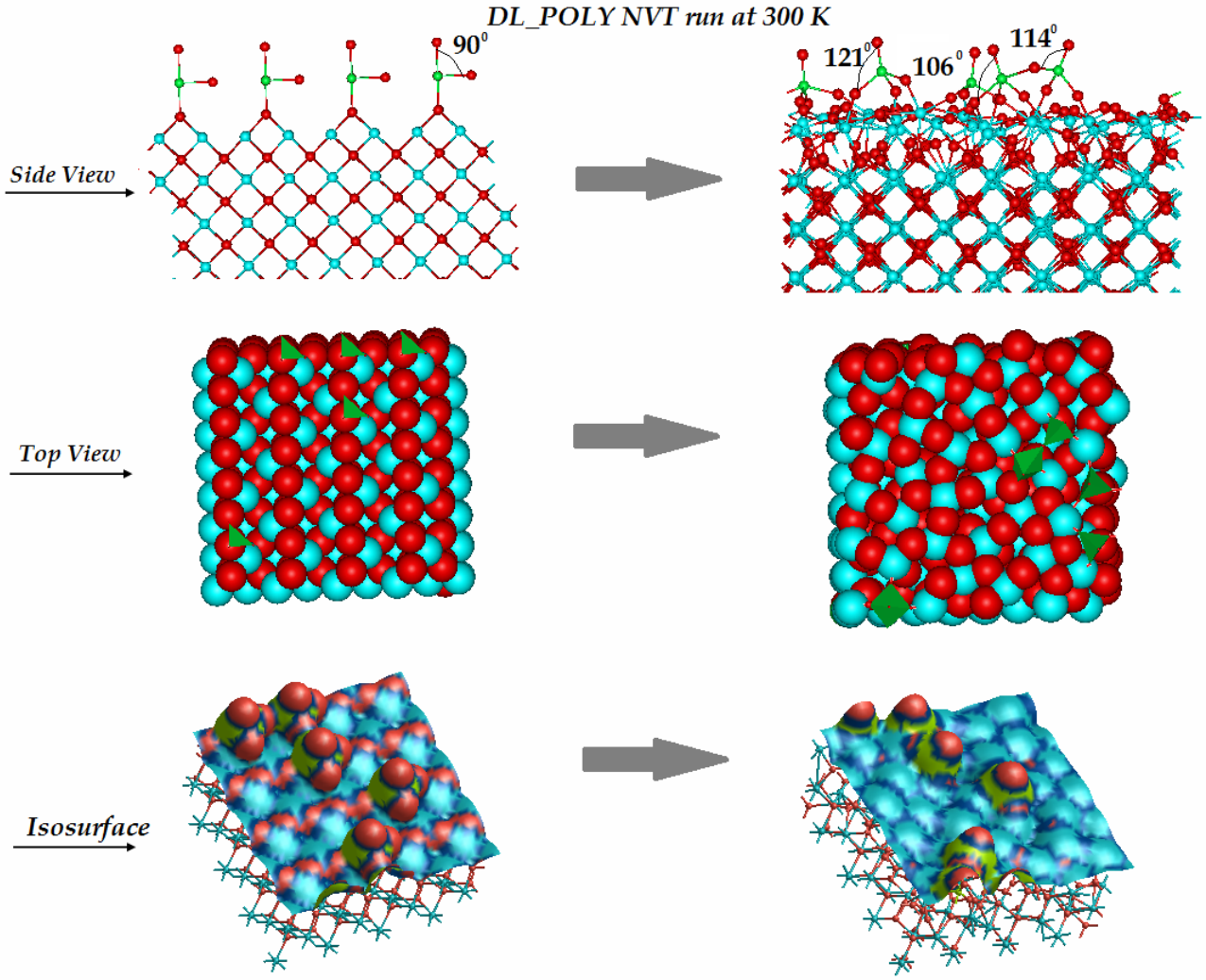

Figure 7.7 The structural changes occurring on the 20% monolayered tungstated {110} surface after a MD run at 300 K.

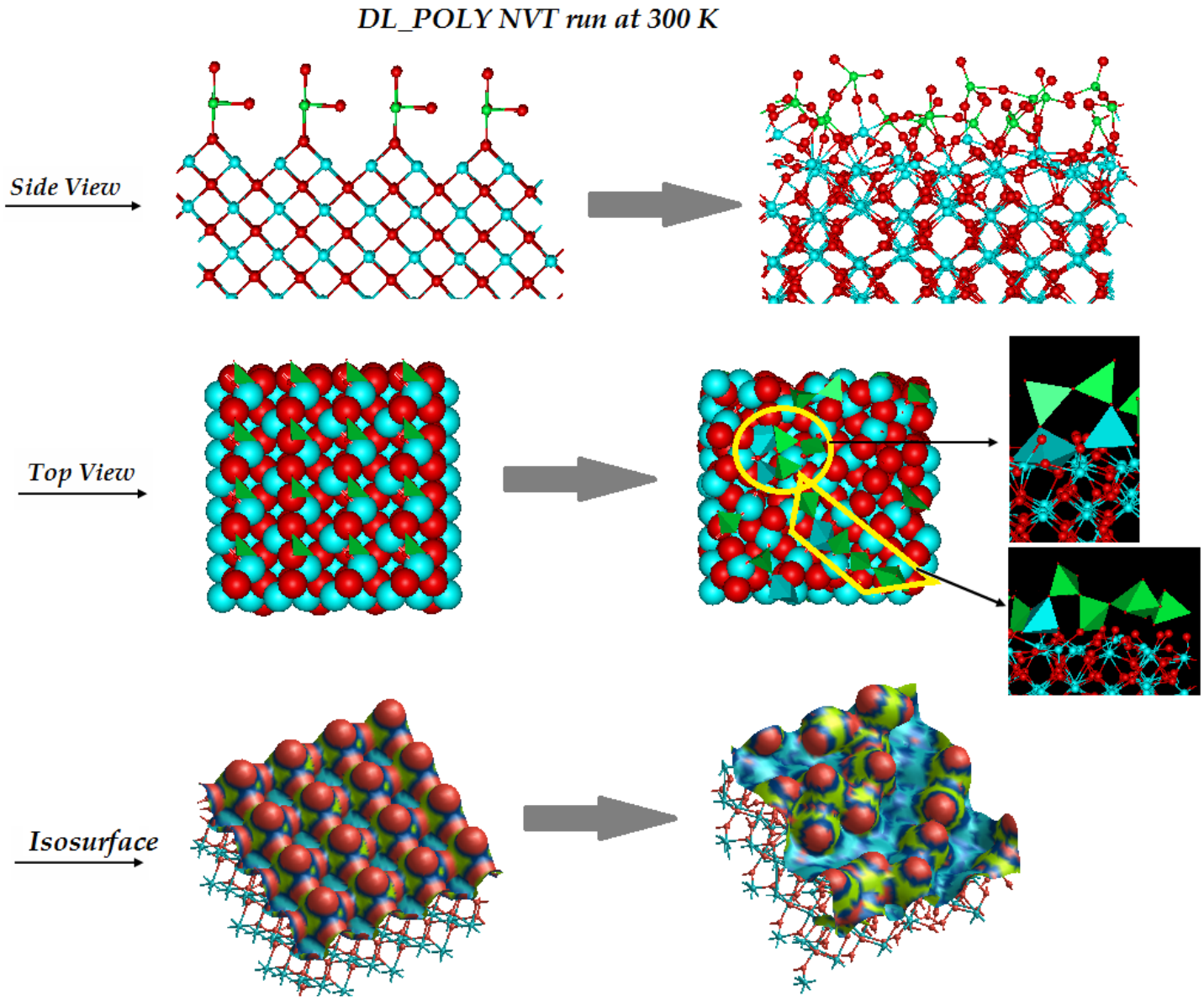

Figure 7.8 The structural changes occurring on the 50% monolayered tungstated {110} surface after a MD run at 300 K.

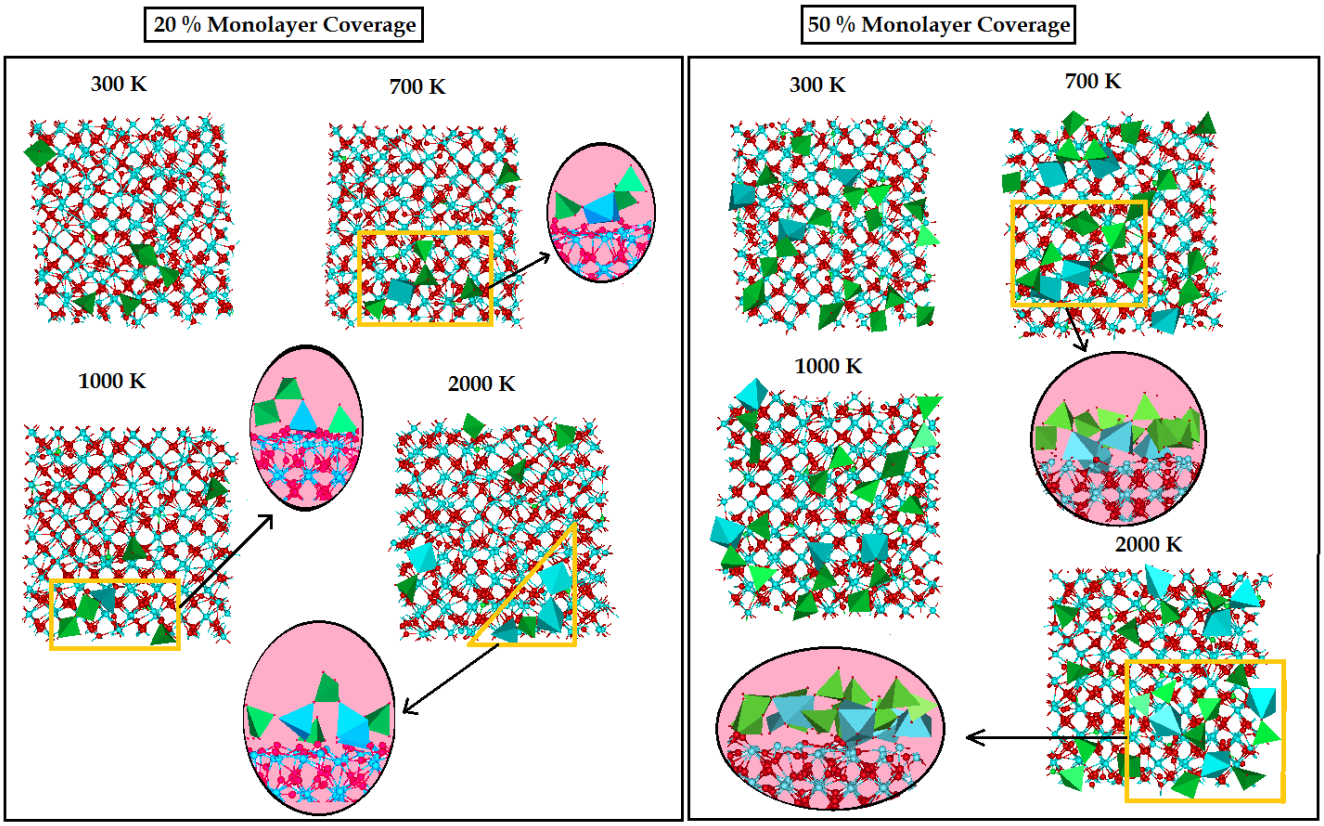

Figure 7.9 The structural changes occurring on 20% and 50% monolayered tungstated {110} surface after the MD run.

Table 7.4 Adsorption and Surface Energies on {110} Surface

Surface {110}	Pure	20% Coverage		50% Coverage	
	γ (J/m^2)	γ(J/m^2)	E_{ad} (eV)	γ(J/m^2)	E_{ad} (eV)
300 K	2.74	2.62	-0.66	2.64	-0.16
700 K	2.73	2.63	-0.52	2.72	-0.02
1000 K	2.65	2.40	-1.36	2.83	0.29
1200 K	2.67	2.50	-0.90	2.66	-0.016
1500 K	2.67	2.49	-0.99	2.57	-0.17
2000 K	2.58	2.44	-0.78	2.47	-0.194
2500 K	2.62	2.26	-1.91	2.54	-0.135

7.3.5 *{111} Surface*

At 20 % coverages on this surface it was noted that all the WO_3 groups after the simulation remained as monomeric species. The distorting WO_3 groups resulted in an increase of O-W-O bond angles by 30º. Increasing the temperatures here didn't show any change on surface and WO_3 groups still remained as monotungstate see Figure 7.10 .

The addition of polymerised WO_3 species using the 50 % coverage system was not possible because just like the {110} surface the larger distance between the adjacent atoms didn't facilitate the addition of a polymerized WO_3 chains. For this reason, the WO_3 atoms were added as monomeric groups. After the MD run for this coverage, it was also noted that although the WO_3 groups still retained as monotungstate, at certain points the zirconium atoms from the surface interconnected to two WO_3 groups on the surface as shown in Figure 7.11. As the temperatures were increased more surface zirconium atoms moved away from the surface forming a bridge connecting two monotungstate species resulting in WO_3-Zr-WO_3. The W-O-W and W-O-Zr bond lengths were also found to be in the range of 3.5 to 3.9 Å, almost similar to the values obtained on {110} surface.

To understand if this surface was stable to the addition of WO_3 the values from the Table 7.5 were evaluated. It was noted that the addition of WO_3 resulted in a drastic lowering of surface energies of 2.63 J/m^2 for pure surface to 2.29 J/m^2 and 2.04 J/m^2 for 20 % and 50 % coverages respectively. Thus the estimated drops were around 13 % for 20 %

coverage and 22 % for 50 % coverages at 300 K. Infact the surface energies obtained on this surface were the lowest compared to all the other surfaces evaluated. Unlike the other surfaces the increase in coverage on this surface only resulted in further lowering of surface energies. The negative values of adsorption energies obtained for this surface are the highest compared to all the other surfaces, implying that if sufficient WO_3 species are present, this surface is capable of forming a 50% monolayer coverage. The earlier experimental studies have already proposed that higher-activity catalysts, showed spectroscopic evidence of Zr-stabilized WO_x species which were postulated to be responsible for the enhanced catalytic performance. [25] It could be probable that the peculiar type of polymerization on this surface assisted by zirconium atoms resulting in - WO_3 –Zr- WO_3 - species might have a role to play for the stabilisation of the surface as well as increased catalytic activity. Finally, this surface can be considered as one of the most suitable surfaces for WO_3 addition.

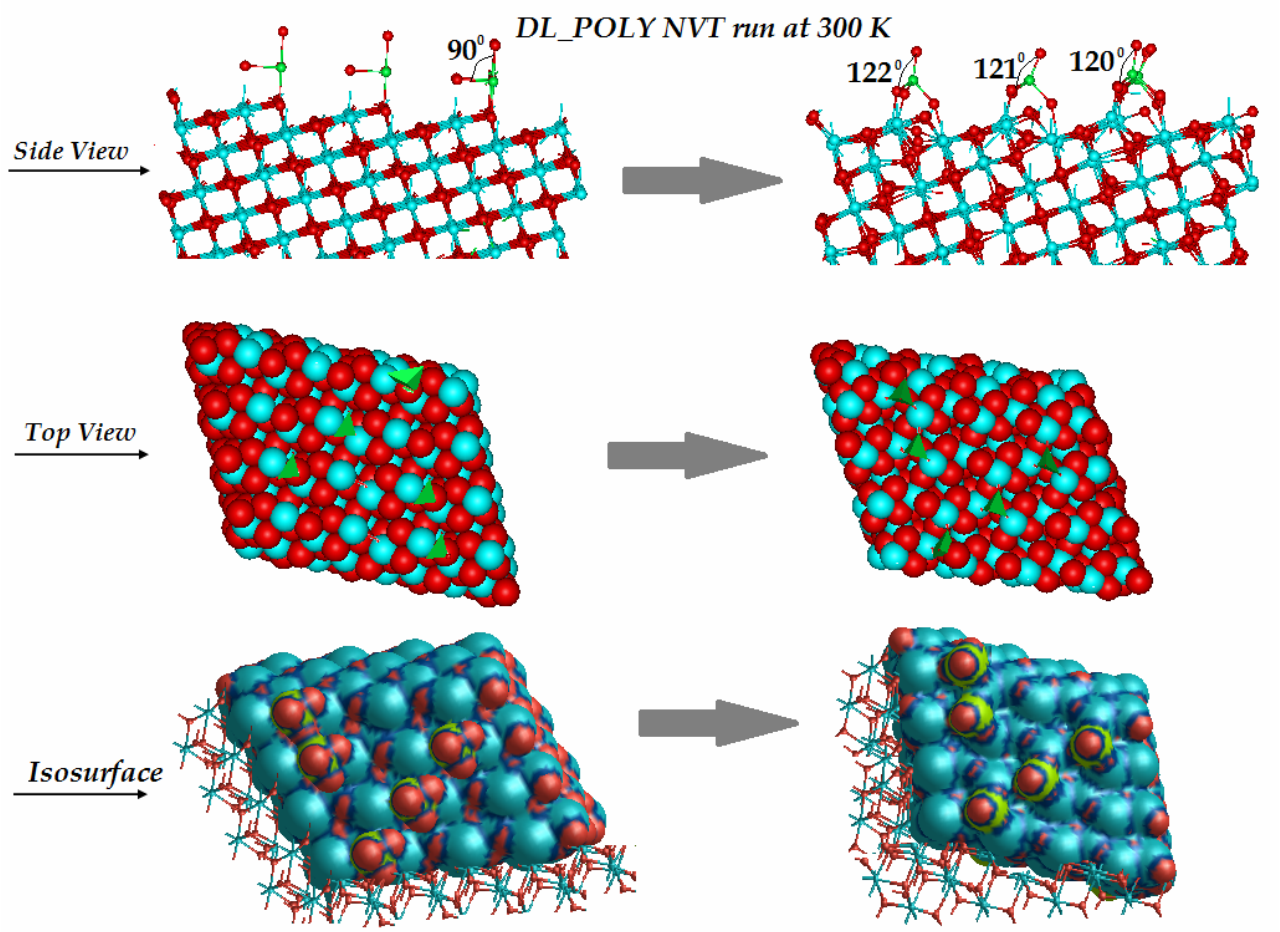

Figure 7.10 The structural changes occurring on the 20% monolayered tungstated {111} surface after a MD run at 300 K.

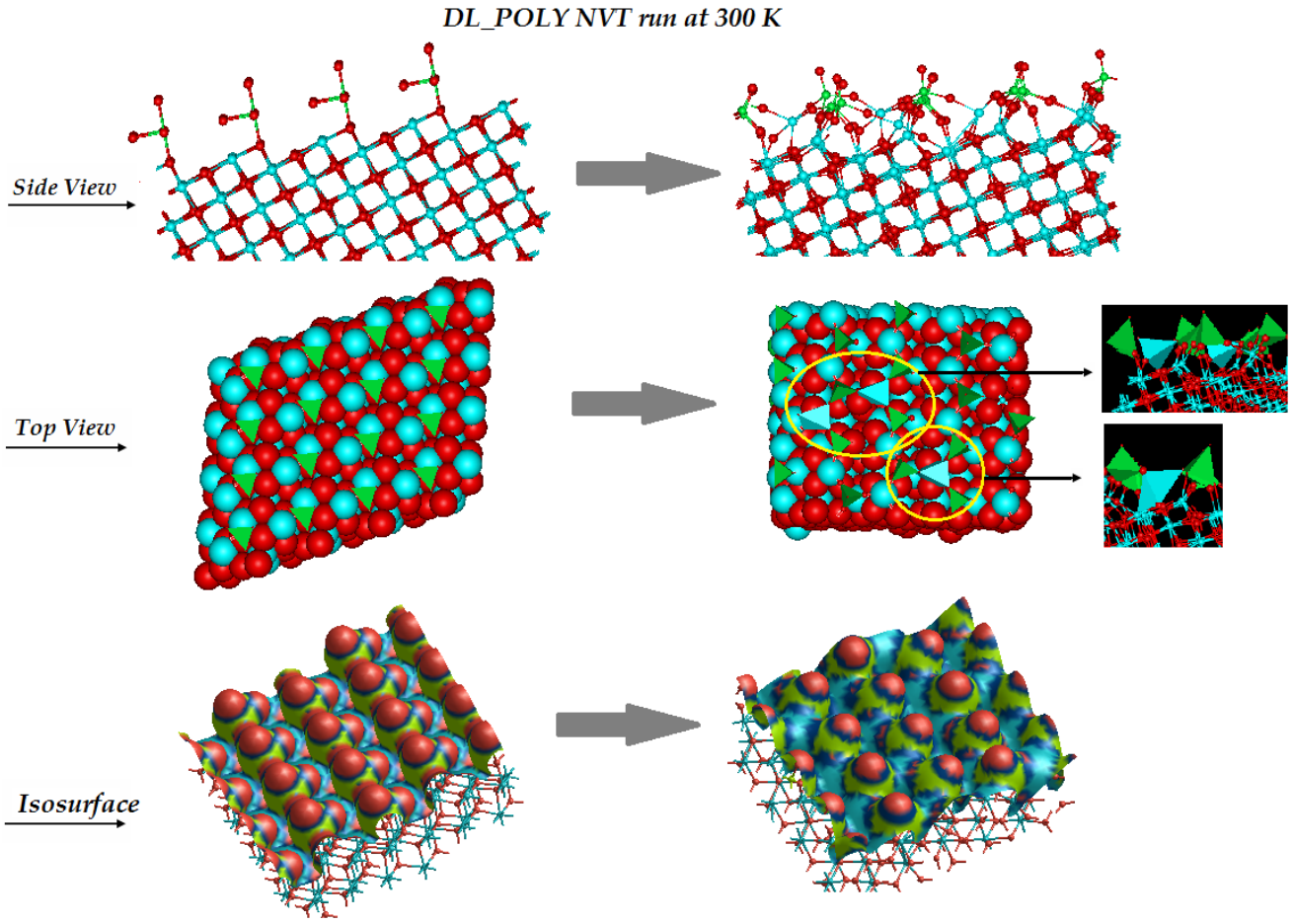

Figure 7.11 The structural changes occurring on the 50% monolayered tungstated {111} surface after a MD run at 300 K.

Table 7.5 Adsorption and Surface Energies on {111} Surface

Surface {111}	Pure	20% Coverage		50% Coverage	
	γ (J/m^2)	γ(J/m^2)	E_{ad} (eV)	γ(J/m^2)	E_{ad} (eV)
300 K	2.63	2.29	-2.01	2.04	-1.18
700 K	2.63	2.31	-1.92	2.07	-1.03
1000 K	2.62	2.29	-1.96	2.10	-0.97
1200 K	2.50	2.28	-1.33	2.22	-0.53
1500 K	2.58	2.26	-1.87	2.26	-0.60
2000 K	2.59	2.22	-2.22	2.19	-0.74
2500 K	2.59	2.21	-2.24	2.13	-0.84

7.4.6 Conclusion

The results in this chapter justifies that the preference for the addition of WO_3 species depended on the type of the surface of t-ZrO_2. It could be concluded that the addition of WO_3 species had a profound impact on the stabilisation of t-ZrO_2 surfaces. The already stable surfaces of pure of t-ZrO_2 showed instability, while the unstable surfaces became more stable on addition of WO_3 species. The addition of WO_3 species at 50% monolayer coverages resulted in a change in order of stability at 300 K {111} > {101} > {100} > {110} > {001}. For 20% monolayer coverages at 300 K, the stability was as follows: {101} > {111} > {100} > {001} > {110}. The surfaces {101} and {001} are not favourable to WO_3 addition. It was generally observed that increasing the WO_3 monolayer coverage causes instability in all types of surfaces except for the {111} surface and {100} surface. For the {111} surface, a 50% coverage resulted in more stabilisation of this surface for all the temperature ranges considered here. For the {100} surface the 50% ones were more stable than the 20% ones only at 300 K, above this temperature it became unstable. The adsorption energy of WO_3 groups on a bare {111} surface is highly exothermic followed by {100} surface. The relative decrease in surface energy values for the {111} surface after WO_3 additions at 50% coverages were estimated to be about 20% lower than its pure surface energy values up to 1000 K. Above 1000 K, the decrease was around 12%. For 20% monolayer coverages on {111} surface, there was only 12% decrease in surface energy values until 1000 K, after which it reduces further to about 8% . For the {100} surface the reduction of surface energies for

50% coverages was around 22% at 300 K. Above this temperature there is a drastic shift to around to 15% indicating the lower thermal stability of this surface for higher loading of WO_3 species. For 20% monolayer coverages on this surface, the decreases in surface energies were observed from 17% at 300 K to 14% at 700 K and above. For {110} surface, both 50% and 20% monolayer coverages resulted in the reduction of surface energies between 1 to 3%. Thus it could be suggested that the probability for the growth of {111} surface after WO_3 addition is much higher than all the other surfaces considered here. This is due to the relative stability of this surface confirmed by lowest decrease in surface energies and favourable adsorption energies. This study has also identified the formation of polytungstate, WO_3 cluster and Zr- WO_3 type species formed on the surfaces of t-ZrO_2 as suggested earlier by Keily *et al*. [25] For the {111} surface no direct polymerization of WO_3 groups was noted, however zirconium aided linkages were noted at the 50% coverages resulting in -WO_3 –Zr- WO_3- type species. For the {001} surface, it was noted that the WO_3 groups polymerises despite the fact that unfavourable values of surface and adsorption energies were obtained on this surface. It could be possible that the nature of the WO_3 species might also have an association with the available surface areas on this surface rather than just the type of surface and temperature. Earlier experimental studies have already confirmed that, higher surface areas leads to the preferable stabilisation of mono atomically bound W (tungsten) atoms on zirconia. [37] This takes us to the next chapter, where we explore the changes on the surface areas and the nature of interaction of WO_3 groups with the zirconia surfaces.

7.5 References

[1] T.N. Vu, J. van Gestel, J.P. Gilson, C. Collet, J.P. Dath, J.C. Duchet, *J. Catal*., 231 (2005) 468.
[2] D.G. Barton, S.L. Soled, G.D. Meitzner, G.A. Fuentes, E. Iglesia,, *J. Catal*., 181 (1999) 57.
[3] S.V. Filimonova, A.V. Nosov, M. Scheithauer, H. Knözinger, *J. Catal*., 198 (2001) 89.
[4] J.M. Grau, J.C. Yori, J.M. Parera, *Appl. Catal. A*, 213 (2001) 247.
[5] E. Iglesia, D.G. Barton, S.L. Soled, S. Miseo, J.E. Baumgartner, W.E. Gates, G.A. Fuentes, G.D. Meitzner, *Stud. Surf. Sci. Catal*., 101 (1996) 533.
[6] S. Kuba, P. Lukinskas, R.K. Grasselli, B.C. Gates, H. Knözinger, *J. Catal*., 216 (2003) 553.
[7] S. Kuba, P. Lukinskas, R. Ahmad, F.C. Jentoft, R.K. Grasselli, B.C.Gates, H. Knözinger, *J. Catal*., 219 (2003) 376.
[8] M. Hino, K. Arata, *J. Chem. Soc., Chem. Commun*., 18 (1980) 851.
[9] M. Hino, K. Arata, *J. Chem. Soc., Chem. Commun*., 18 (1988) 1259.
[10] X. Song, A. Sayari, *Catal.Rev.-Sci.Eng*., 38 (1996) 329.
[11] F. Babou, B. Bigot, P. Sautet, *J. Phys.Chem*., 97 (1993) 11501.
[12] Y. A. Ono, *Catal. Today*, 81 (2003) 3.
[13] J.G. Santiesteban, J. C. Vartuli, S. Han, R.D. Bastian, C.D. Chang, *J. Catal*., 168 (1997) 431.
[14] M. Scheithauer, R. K. Grasselli, H. Knözinger, *Langmuir*, 14 (1998) 3019.
[15] M. Scheithauer, T. K. Cheung, R.E. Jentoft, R. K. Grasselli, B.C. Gates, H. Knözinger, *J. Catal*., 180 (1998) 1.
[16] E. Iglesia, D. G. Barton, S. L. Soled, S. Miseo, J. E. Baumgartner, W. E. Gates, G. A. Fuentes, G. D. Meitzner, *In Proc. 11th Int. Congr. Catal.*, 1996, 533.
[17] G. Larsen, E. Lotero, R. D. Parra, *In Proc. 11th Int. Congr. Catal*., 1996, 543.
[18] C. D. Baertsch, S. L. Soled, E. Iglesia, *J. Phys. Chem. B*, 105 (2001) 1320.
[19] C. D. Baertsch, K. T. Komala, Y. H. Chua, E. J. Iglesia, *J. Catal*. 205 (2002) 44.
[20] J. Macht, *J. Catal*., 227 (2004) 479.
[21] I. E. Wachs, T. Kim, E. I. Ross, *Catal. Today*, 116 (2006) 162.
[22] T. Kim, A. Burrows, C. J. Kiely, I. E. Wachs, *J. Catal*. 246 (2007) 370.
[23] E. I. Ross-Medgaarden, I. E. Wachs, *J. Phys. Chem. C*, 111 (2007) 15089.
[24] E. I. Ross-Medgaarden, W. V. Knowles, T. Kim, M. S. Wong, W. Zhou, C. J. Kiely, I. E. Wachs, *J. Catal*., 256 (2008) 108.
[25] W. Zhou, E. I. Ross-Medgaarden, W. V. Knowles, M. S. Wong, I. E. Wachs, C. J. Kiely, *Nat. Mater*., 1 (2009) 723.
[26] M. Boudart, *J. Mol. Catal*., 30 (1985) 27.
[27] G. A. Somorjai, *J. Mol. Struct*. (THEOCHEM), 424 (1998) 101.
[28] G. A. Somorjai, *Introduction to Surface Chemistry And Catalysis*; John Wiley & Sons Inc.: New York, 1994.
[28] T. P. Beebe, D. W. Goodman, B. D. Kay, J. T. Yates, *J. Chem. Phys*., 87 (1987) 2305.
[29] M. B. Lee, Q. Y. Yang, S. L. Tong, S. T. Ceyer, *J. Chem. Phys*.,87 (1987) 2724.

[30] K. Klier, J. S. Hess, R. G. Herman, *J. Chem. Phys*., 107 (1997) 10.
[31] R. Grau-Crespo, N. C. Hernandez, J. F. Sanz, N. H. de Leeuw, *J. Phys. Chem. C*, 111 (2007) 10448.
[32] S. E. Redfern, R. W. Grimes, R. D. Rawlings, *J. Mater. Chem*., 11 (2001) 449.
[33] S. Nosé, *J. Chem. Phys*., 81 (1984) 511.
[34] W.G. Hoover, *Phys. Rev. A*, 31 (1985) 1695.
[35] L. Verlet, *Phys. Rev*., 156 (1967) 98.
[36] W. Humphrey, A. Dalke, K. Schulten, *J. Mol. Graph*., 14 (1996) 33.
[37] D. Kaucký, B. Wichterlová, J. Dedecek, Z. Sobalik, I. Jakubec, *Appl.Catal. A*: *Gen*., 397 (2011) 82.

Chapter 8: Investigation of RDF, Surface topology and Crystal Morphology studies on t-ZrO_2 and the effect of WO_3 addition

"Nothing has such power to broaden the mind as the ability to investigate systematically and truly all that comes under thy observation in life".

— Marcus Antoninus Aurelius

8.1 Introduction

In chapter 7 we found that, the surface of zirconia undergoes reconstruction when WO_3 groups were adsorbed on to it. The nature of the reconstruction depended on the type of surface and the temperature used for the simulation. The nature of the WO_3 species too varied depending on the surface type and the temperature. The WO_3 species is existed either as monotungstate, polytungstate or clusters. We also detected that the WO_3 species on the {111} surface existed mainly as monotungstate at lower temperatures. This surface showed the highest stability to accommodate WO_3 species compared to all the other surfaces. The formation of the polytungstate species on this surface was observed only at higher temperatures. Earlier studies have proposed multiple catalytic active sites for WO_3 – ZrO_2 catalysts [1-4], but supporting information for the nature of the true catalytic active phase is still lacking. It has however been indicated that the increase in polytungstate or cluster networks results in the increase in acidity for the WO_3 – ZrO_2 catalyst. [3-8] These previous studies used a wide variety of characterization techniques such as XRD, FT-IR, UV- visible spectroscopy and catalytic testing such as BET, TPO,

Microcalorimetry to describe the composition, oxidation state, coordination and nature of the acidity (Brønsted vs Lewis) of the WO_3 species participating as the catalytic active sites. [5, 9-12] Experimental studies by Jongsomjit and co-workers [13, 14] reported that the formation of monotungstate species on zirconia increases the acidity of WO_3-ZrO_2 catalyst. They found that the monotungstate species is capable of inducing the presence of F-centers (electrons stabilized in oxygen vacancy) in zirconia which enhances the catalytic activity. Although the type of species responsible for the enhanced acidity is not clearly understood, it is a known fact that WO_3 – ZrO_2 with enhanced acidity serves as an efficient catalyst for many reactions. [6-9]

Catalysts with strongly acidic properties are of interest in many catalytic processes such as reduction of NO_x to N_2, xylene formation from toluene and methanol , oligomerization of $<C_{20}$ alkanes to gasoline, diesel and lubricants etc. [15-20] This is because strongly acidic catalysts are capable of delocalizing the electrons and donating the protons needed for the catalytic reaction. [21-23] For this delocalization effect to take place, there should be a strong interactions between the atom pairs. In the case of WO_3-ZrO_2, the strong interactions should happen between W, O and Zr atoms which will results in weaker O-H bonds under experimental conditions. This will result in the easy release of the protons (H^+) needed for catalytic reactions. Thus, it is clear that the nature of interaction of adsorbed species with the zirconia matrix plays an important role in determining the

catalyst performance. Hence, it is important to monitor the strength of the interaction between atom pairs after the addition of WO_3 species.

From a computational perspective, one way to study these interactions is to calculate the radial distribution functions (RDF). [24-29] RDF's serve as finger prints to identify the relationships between various atom pairs; this provides us with an insight into the adsorbate-adsorbent interactions. The persistence of strong or weak interactions can be easily detected by comparing the amplitudes of RDF peaks. RDF also provides a useful way of describing the structure of a system by extracting the pair distribution function *g(r)* from the molecular dynamics runs. This function gives us the probability of finding an atom at a distance *r* from another atom on the adsorbed layer. In this chapter, we provide an atomic scale picture of the complex interplay between the surface atom species with the help of computational modeling techniques. The nature of coordination of atoms from WO_3 species to the surface of zirconia and the strength of atom-atom interactions are studied using RDF analysis. The preference of WO_3 species to exist as monotungstate or polytungstate is analysed using surface area measurements. Finally, the changes in the crystal morphology resulting from the addition of WO_3 to t-ZrO_2 using Wulff construction plots were also analysed.

8.2 Comparison of RDF plots

8.2.1 RDF of Pure Surfaces

The comparison of RDF plots between Zr-O atom pairs for all pure surfaces of t-ZrO_2 (Figure 8.1) indicates that the RDF peaks are most intense for the {101} surface. The highest intensity indicates extremely good packing density, which means stronger interactions and higher compactness in the structure.[30] This is in agreement with the earlier studies (section 5.3 of chapter 5) which revealed the presence of high compactness of atoms on the most stable {101} surface. For {101},{111}, {100} and{110} surfaces, the most intense peak, which corresponds to the first coordination shell around zirconium, is at 2 Å. This is followed by less intense peaks at 4 Å, 5.5 Å and 6.5 Å corresponding to the coordination shells further away (see Figure 8.1).

The peaks from {001} surface were lowest in intensity. Moreover, the peaks, except the first one, were not well defined indicating structural disorder at long ranges. Apart from this surface, all the other surfaces depicted a similar pattern of peaks even though their relative intensities varied from each other. The effect of increasing the temperatures resulted in broadening of peaks for all surfaces except the {001} surface. Figure 8.2 shows the broadening of the RDF peaks for Zr-O atom pairs on the {101} surface with increasing temperatures. A similar trend with the effect of temperature was also noted on

other surfaces except the {001} surface. For the {001} surface, however, there was a broadening of the first peak along with a sudden increase in the intensity of the next neighbouring peaks at 1000 K see Figure 8.3. The enhanced intensity suggests the appearance of long range order at 1000 K, which in turn, suggests that this surface might undergo reconstruction around this temperature.

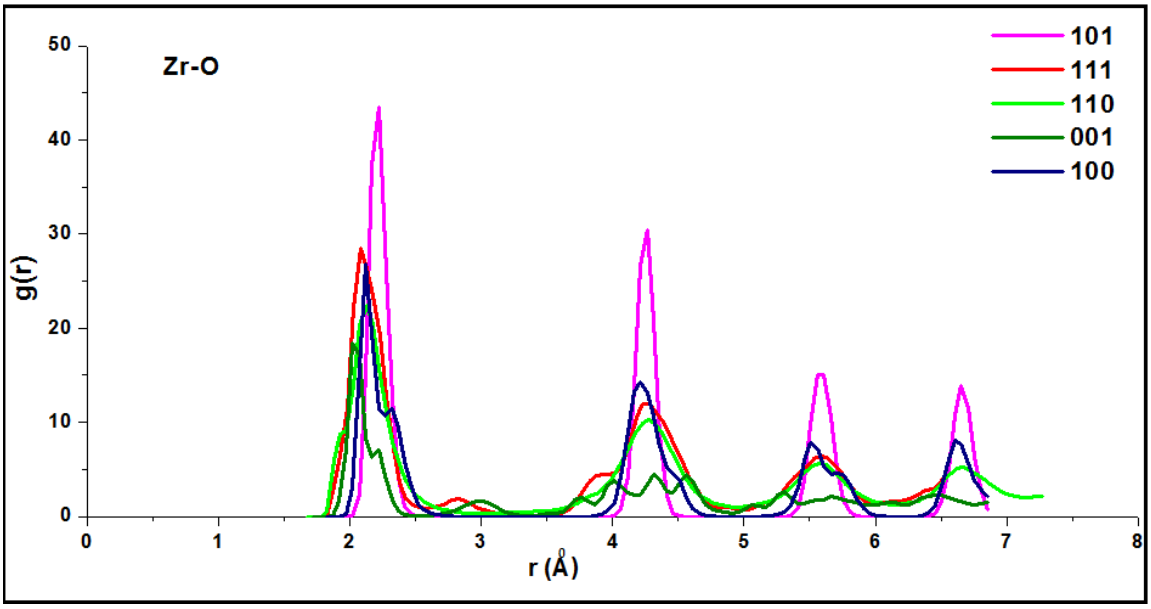

Figure 8.1. The comparison of RDF's between Zr-O atom pairs between all low index pure surfaces of t-ZrO_2 at 300 K.

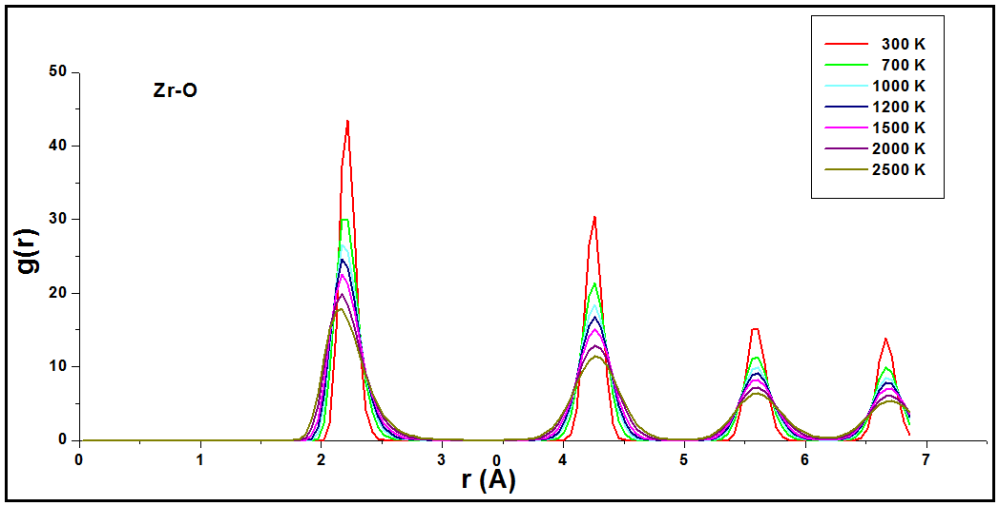

Figure 8.2 The RDF's between Zr-O atom pairs on {101} surface of t-ZrO_2 with increasing temperatures.

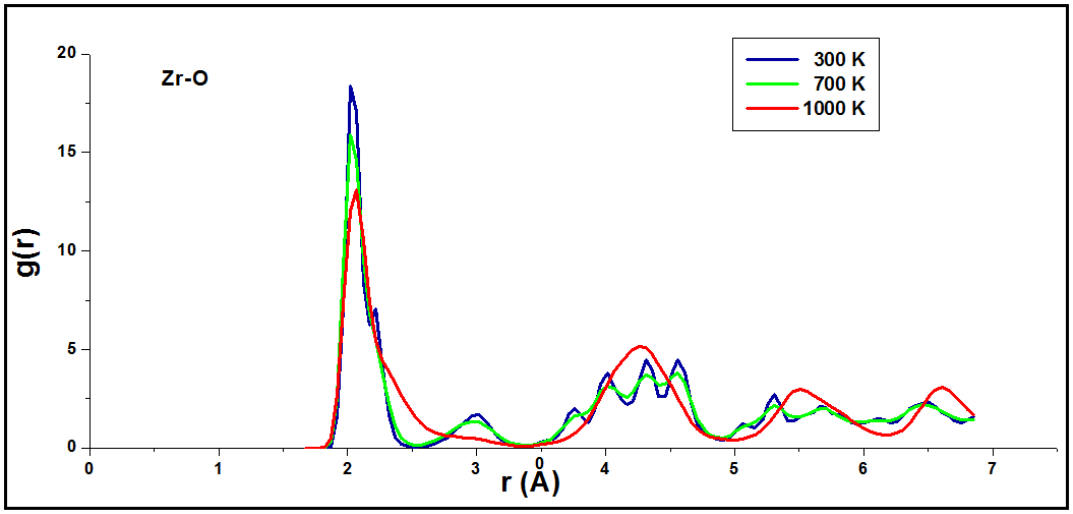

Figure 8.3 The RDF's between Zr-O atom pairs on {001} surface of t-ZrO_2 with increasing temperature.

8. 2. 2 RDF of WO_3 –ZrO_2 surface

8.2.2.1 Zr-O Atom Pair

After tungstating with WO_3 species, we observed that, the RDF of Zr-O atom pairs for bulk atoms on both 20 % and 50 % coverages revealed an overlapping of the peaks for the {111} and {101} surface see Figure 8.4 (a) This overlapping occurred due to the decrease in total intensity of RDF peaks for Zr-O atom pairs on {101} surface after tungstating it. The pattern of peaks obtained for the {110} and {100} surface were similar to each other, however these peaks were broader than those on the {101} and {111} surfaces. A comparison of the {101} and {111} surface before and after tungstating it, is shown in Figure 8.4 (b) and (c). The intensity values for the {101} surface become almost half after tungstating the surface see Figure 8.4 (b). This suggests that the addition of WO_3 groups resulted in more structural disorder to the {101} surface and is agreeable with the results obtained from Chapter 7. For the {111}, {110} and {100} surfaces, the change in intensity of Zr-O atom pair after tungstating it remained close to the pure surface values. Finally, it could be concluded from the Figure 8.4 (a) that the addition of WO_3 resulted in the total intensity of all Zr-O peaks getting somewhat close to each other for the {101}, {111}, {110} and {100} surfaces. No peak shifting was noted after tungstating it. Since the surface atoms are of primary importance here, because of their active participation in catalytic reactions, the coordination environment of surface atoms were also monitored. This was done by choosing the surface atoms on the slab and

plotting their RDF peaks. The surface atoms (Zr, O) on the {101} surface depicted strong interactions which were noted by the large intensities obtained for both coverages see Figure 8.5 (a) and (b). This larger value of intensity for Zr-O atom pairs, is due to the additional interactions prevailing between the oxygen atoms from the WO_3 species with the surface zirconium atoms.

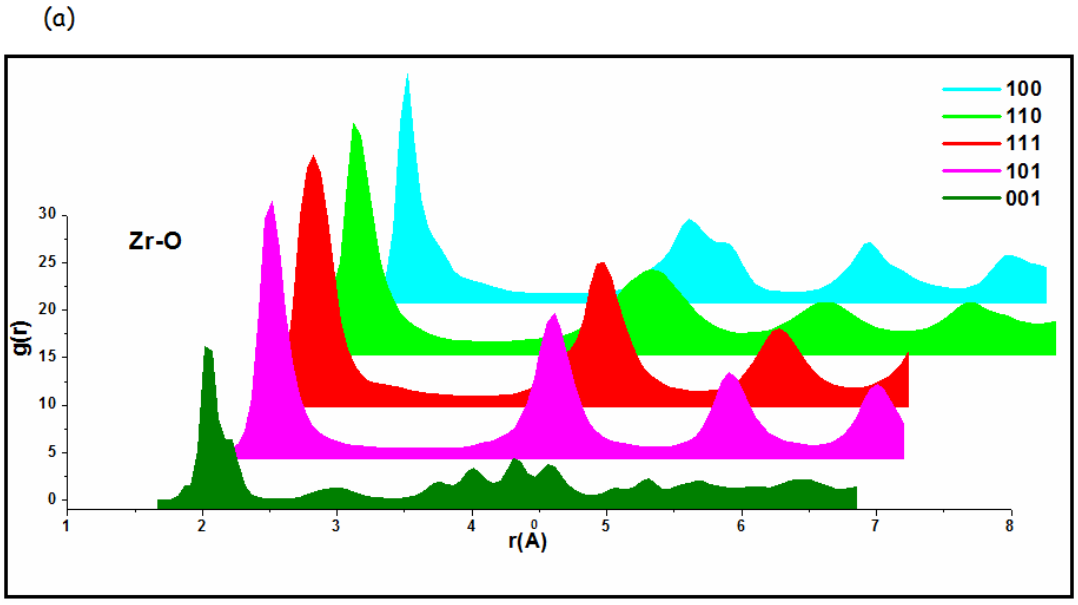

Figure 8.4 (a) The RDF's between Zr-O atom pairs at 300 K on different surfaces of t-ZrO_2 with 20 % monolayer coverages.

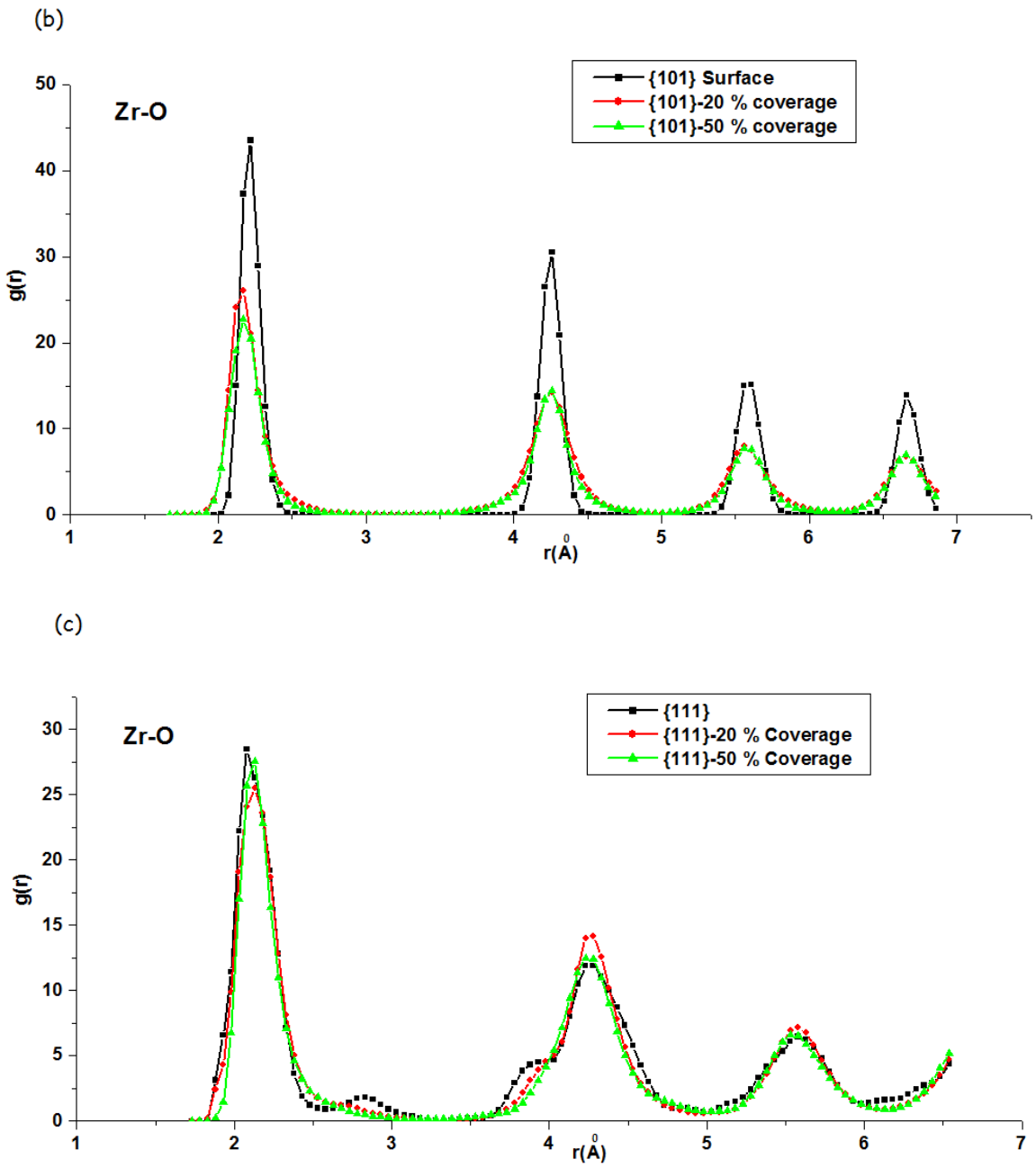

Figure 8.4 (b) The RDF's between Zr-O atom pairs at 300 K on {101} surface before and after tungstating. (c) The RDF's between Zr-O atom pairs at 300 K on {111} surface before and after tungstating.

(a)

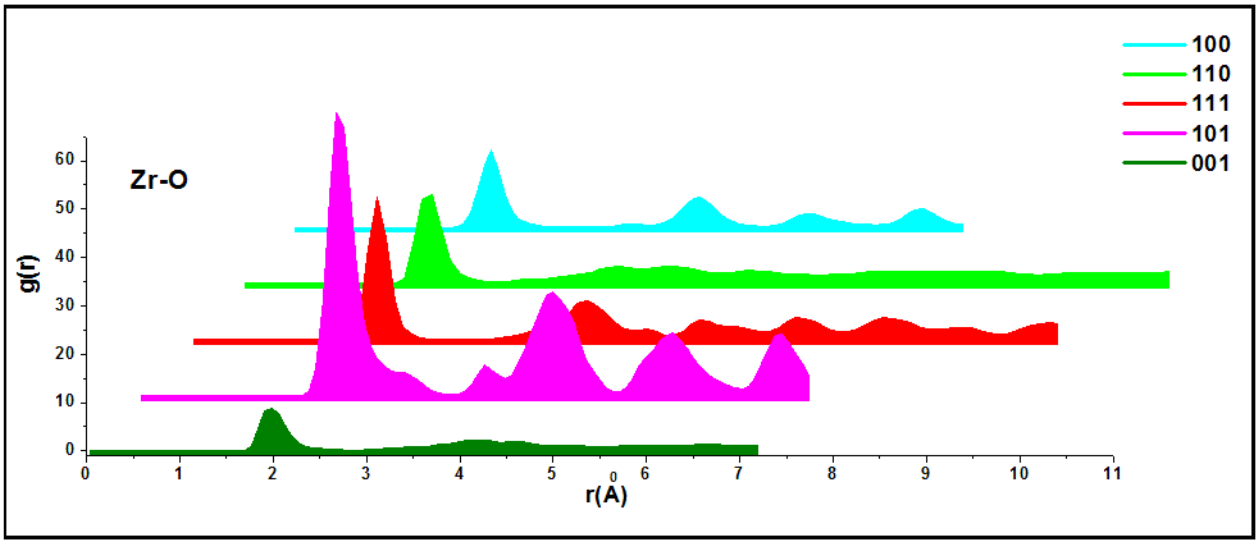

(b)

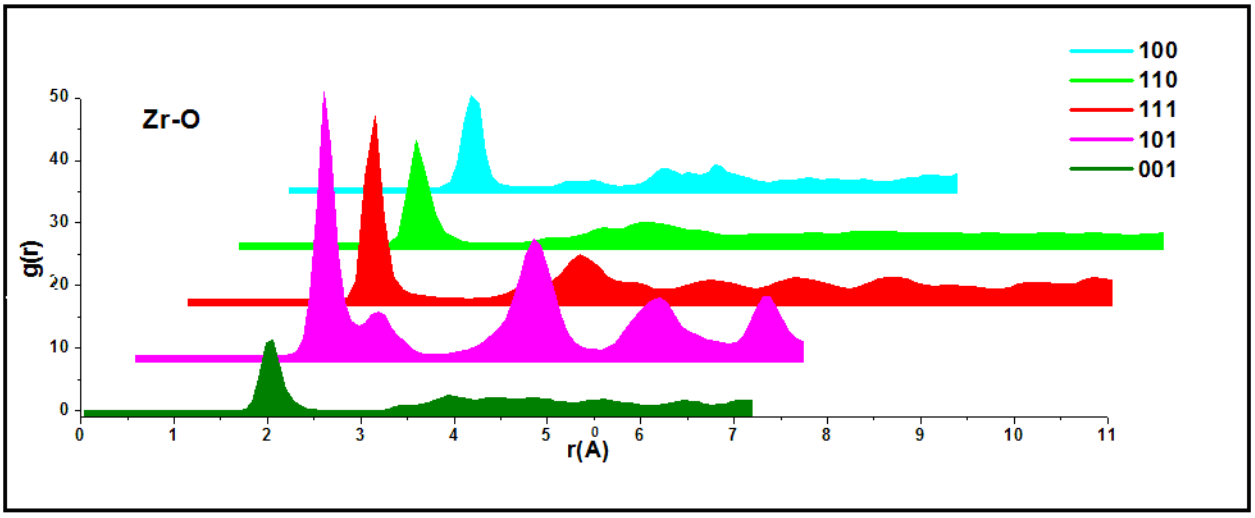

Figure 8.5 The comparison of RDF's of surface atoms between Zr-O atom pairs between all low index surfaces at 300 K (a) 20 % coverages of WO_3 (b) 50 % coverages of WO_3 .

8.2.2.2 W-O Atom pair

The RDF's of W-O atom pairs revealed the highest intensity for the {111} surface for both coverages see Figure 8.7. The intensity values of W-O atom pairs were in the following order for both coverages: {111} > {110} > {101} > {100} > {001}. The interactions of tungsten with the oxygen atoms lying on the surface of zirconia matrix were compared with the WO_3 bulk intensities. For 50 % coverages, the value of intensities were approximately three times the values obtained on WO_3 bulk for {111} surface and almost 1.5 times for the {110} surface. For the {101} and {100} surface these values were roughly the same as that of WO_3 bulk. For the {001} surface the intensity value was the lowest. The higher intensity on {111} surface indicates the uniform interactions of WO_3 groups with the zirconia matrix which could be the drving force in the stabilization of this surface as observed in section 7.3.5 of chapter 7.

To investigate the origin of such strong interactions, the changes in W-O bond lengths were monitored before and after the MD runs. The W-O bond distances, were initially set at approximately 2 Å before the simulation (see section 7.3 of chapter 7). However, the RDF analysis reveals the reduction of W-O bond lengths after the simulation. A closer look at the Figure 8.6 (a) shows that, the W-O atom pairs reveals two types of peaks occurring on all surfaces after the addition of WO_3 species. The first peaks correspond to a bond lengths of around 1.5 Å while the second one was around 1.8 Å. In order to understand the nature of the bonds, the final optimized structure from the MD run was

analysed as shown in Figure 8.6 (b). The first peak with the shortest bond lengths (~1.5 Å) were observed on W-O bonds exposed on the surface with oxygen atoms facing upwards. These shortened bond lengths would suggest its application in several reactions capable of forming weaker O-H bonds. [31, 32] The second peak was observed for WO_3 atoms bonded to the oxygen atoms from the zirconia surface. The higher intensity of the second peak suggests it imparts stronger interaction with the surface of zirconia. The highest intensity of the second peak was observed on the {111} surface suggesting stronger interactions of WO_3 species with the zirconia matrix. The least intense peaks were noted on the {001} surface indicating its instability to WO_3 addition as a regular adsorption pattern is not formed, which is in agreement with the surface energy values reported in Chapter 7.

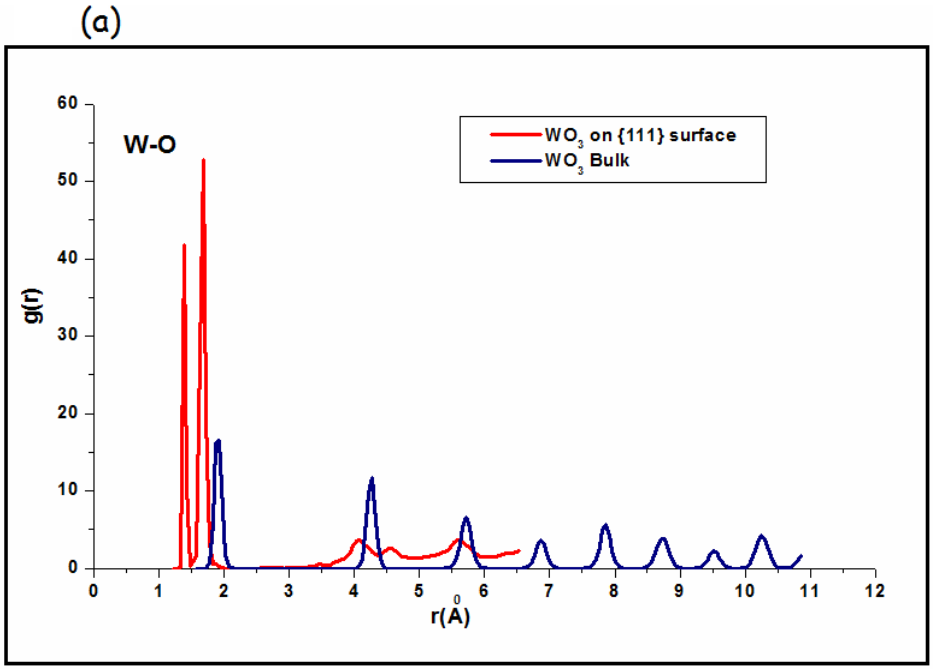

(b)

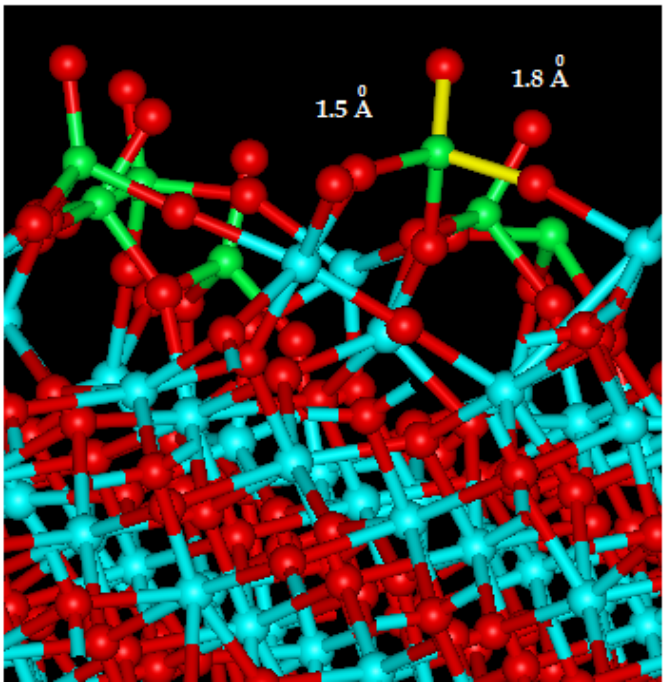

Figure 8.6 (a) Comparison of RDF's between W-O atom pairs of bulk atoms and surface atoms for 50 % coverages on {111} surface. (b) The two types of W-O bonds on t-ZrO_2 surface.

Figure 8.6 (a) shows the comparison of the RDF of W-O atom pairs supported on zirconia with that of bulk WO_3. The intensities of peaks for W-O bonds were higher for the supported WO_3 than that observed for bulk WO_3. This could be due to the shortening of lengths (~1.5 Å and 1.8 Å) of W-O bond on zirconia surface, compared to the W-O bond lengths of ~ 1.9 Å in bulk WO_3. The W-O bond lengths on zirconia surface depicted a typical double bond character. The Figure 8.6 (a) also indicates that a significant

shifting in the peaks occurs on the surface compared to WO_3 bulk. This peak shifting could be attributed to the strong interaction between WO_3 and the zirconia surface and is in agreement with the earlier experimental studies.[34] The intensity of the peaks varied with the amount of WO_3 coverage.

For the 20 % coverages, the first peaks were always less intense than the second peaks except for the {001} surface see Figure 8.7 (a). This higher intensity for the second peaks is due to the higher interaction of tungsten atoms with the oxygen atoms from the zirconia surface. For 50 % coverages, the second peaks were always less intense than the first ones for the {110} and {101} surface. This could be understood as higher interactions of tungsten with the neighbouring oxygens from the first coordination shell as shown in Figure 8.7 (b). This suggests more of dimer, trimer or polymeric interactions occurring on the surfaces which are in agreement with the results from Chapter 7. However, for the {111} surface, the second peaks were more intense than the first ones suggesting a lot of surface interactions occurring due to the monotungstate formation. For {100} surface, both the peaks had almost the same intensity. The {001} surface showed weak intensities for both peaks thus depicting its instability to WO_3 addition. It could thus be concluded that for the WO_3 favourable surfaces, the presence of zirconia enhances the value of *g(r)*, thereby making the W-O atom pairs to establish a strong interaction between them.

(a)

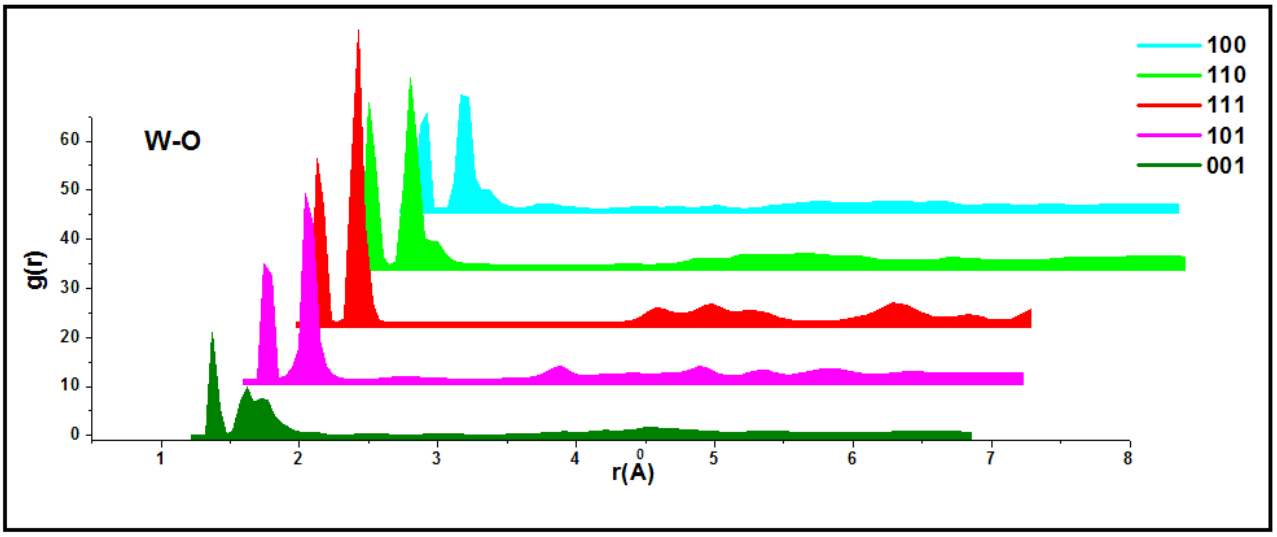

(b)

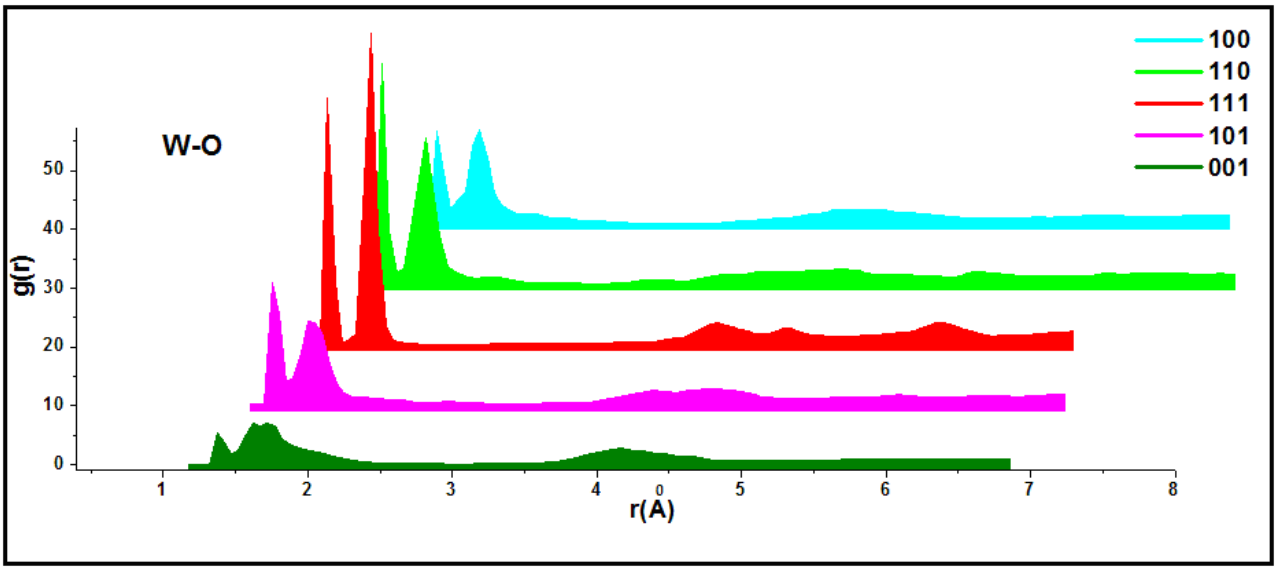

Figure 8.7 The comparison of RDF's between W--O atom pairs between all low index surfaces at 300 K (a) 20 % coverage of WO_3 (b) 50 % coverage of WO_3 .

8.2.2.3 Mechanism of Electron Delocalization

In order to understand the process of delocalization occurring on the various surfaces studied here, it is important to understand the nature of the interaction between the surface atoms namely (Zr-O) and (O-W) atom pairs. This interaction will give us an idea whether delocalization of electrons are likely to occur on a surface and secondly, if it exists, what type of a mechanism is likely to occur, whether it will occur via W-O-W network or Zr atoms will also participate in the network. Although quantum mechanical approaches are powerful to predict such electronic effects, the use of these techniques are computationally more expensive compared to the molecular dynamics.

In the earlier chapter 7 we saw the occurrence of polymerization of WO_3 groups on the {110}, {100} surfaces, however this did not happen on the {111} surface. The existence of montungstate species on {111} surface, questions if the effect of delocalization will take place on this surface or not. Even though WO_3 groups are capable of stabilizing this surface, the effect of delocalization of electrons depends on the strength of interaction between W-O-Zr bonds or W-O-W bonds. Earlier experimental evidence suggests that a polymerized WO_3 network will be more acidic due to its higher capability to delocalize the electrons. [3, 5] Barton *et al*. [3] reported that the higher acidity of the polytungstate appears to relate to their ability to form $W^{6-n}O_x$-(*n*-H^+) centers. A polytungstate species that form at intermediate WO_x surface densities can provide a compromise between reducibility and accessibility of WO_x centers. We strongly believe that for delocalization

to occur between the WO_3 networks, strong interactions must prevail between the surface atoms (Zr, O, W) accompanied by a weaker interaction of surface atoms with the zirconia matrix. A weaker interaction of surface atoms with the zirconia matrix will help the delocalized electrons to stay within the WO_3 network and not get distributed within the bulk. The combined relative strength of interaction between the W-O and Zr-O surface atom pairs, within the W-O-Zr network could be judged by looking at the RDF's for Zr-W atom pairs (see Figure 8.7 (a) and (b)). It was indicated that the highest intensities occurred on the {111} surface for both coverages.

The RDF intensities for Zr-W atom pairs, for 50 % coverages, follow the order: {111} > {110} > {101} > {100} > {001}. A very good long range order was also noted for both coverages on the {111} surface. This long range order was not that pronounced on any other surfaces studied here. The higher intensity of peaks and long range order between these pairs, indicates that the zirconium atoms on this surface interact strongly with the WO_3 network. These stronger interactions suggest the possibility for delocalization of electrons to occur between surface atoms. Since WO_3 groups do not polymerise here, the possibility for this mechanism occurring via -W-O-Zr-O-W- will be the most probable path. This is in agreement with the Zr bridged WO_3 network that we noted on this surface after the MD simulations (see section 7.3.5 of Chapter 7). The earlier section also gave the intensities of Zr-O atom pairs for all atoms on {111}, {110}, {100} and {101} surfaces in a similar range after tungstating. However, the intensity of peaks for Zr-O atoms lying on the surface for the {101} surface were much higher than

on any other surface see Figure 8.5 (a) and (b). Thus it could be proposed that the delocalization on {101} surface could also occur via -W-O-Zr-O-W- network. For the {110} and {100} surfaces, the delocalization of electrons can occur either by -W-O-W-O-W- network rather than the –W-O-Zr-O-W network. Since the WO_3 groups polymerise on these surfaces (see Chapter 7), the chances for delocalization via -W-O-W-O-W-exist here. A very lowest intensity of RDF peaks for all atom pairs were found on the {001} surface, where the effect of delocalization would be minimum. Finally it could be judged that when WO_3 species is adsorbed on to the surfaces of t-ZrO_2, the effect of delocalization will occur depending on the type of the surface.

Earlier experimental studies too have reported that decrease in bond length of W-O atoms causes stronger interactions and higher activity in WO_3 – ZrO_2 catalyst. Chung-Yuan Mou and coworkers [32] analysed the interactions occurring between Zr, W and O atoms for WO_3 -ZrO_2 catalyst in the presence of an iron promoter. They compared the bonds lengths using RDF plots obtained from EXAFS studies and postulated that a decrease in the bond length of W-O atom pairs occur for the WO_3 – ZrO_2 catalyst, compared to the bulk WO_3. It was postulated by them that the strong interactions between the W-O groups represent a delocalization of electrons. These experimental results support our computational study. Finally, it could be concluded that these interactions play an important role in the activity of the catalyst as well as the stabilization of these surfaces upon tungstating them.

(a)

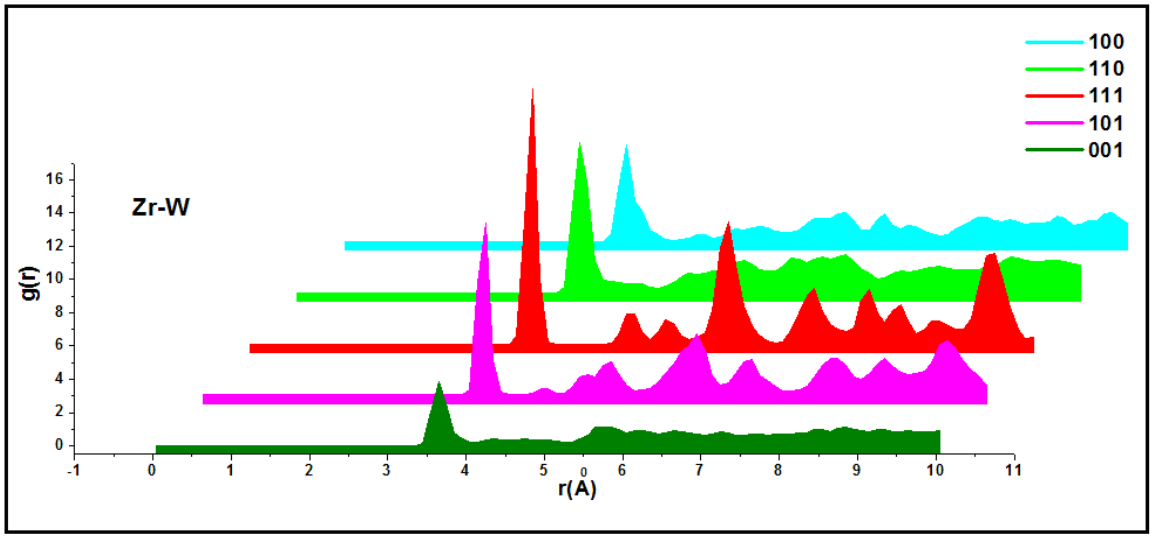

(b)

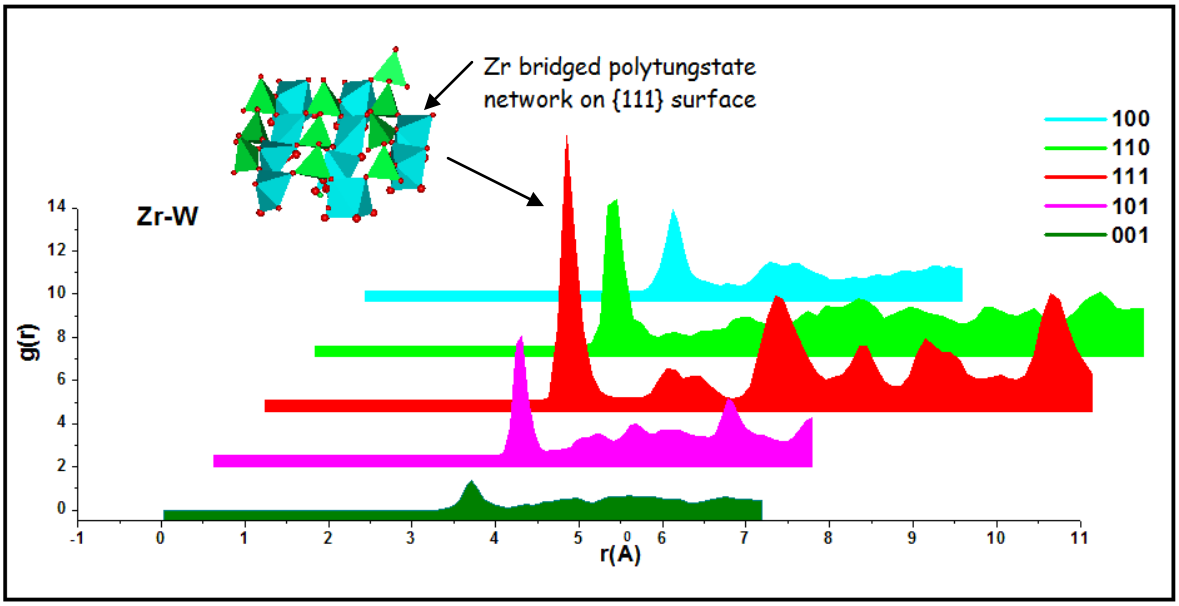

Figure 8.8 The comparison of RDF's between Zr-W atom pairs between all low index surfaces at 300 K (a) 20 % coverage of WO_3 (b) 50 % coverage of WO_3 (W atoms shown in green and Zr atoms in blue).

8.3 Surface Areas

Surface areas play an important role in catalysis. [33-35] In general, the larger the surface area, the higher the active sites available for a reaction. [36-38] This also means that, to design an efficient catalyst, we need to maximize the available surface area. One of the major drawbacks of commercially available t-ZrO_2 is its low surface area. [39] Recently in literature, several preparation methods were suggested to obtain high surface area zirconia. This includes, impregnation of high surface area active carbon with zirconyl nitrate [40], addition of other oxides such as lanthanum oxide, magnesium oxide, aluminum oxide or yttrium oxide, and the addition of sulfuric acid to zirconia. [41- 44] Chuah and Jaenicke [45] reported a method to prepare zirconia with high surface area and thermal stability using zirconium chloride and NaOH or KOH as precipitation agents. Although experimentally many such methods have been suggested, it is important to find an alternative approach using computational techniques to find a surface providing the largest surface area. Detecting the surface with the highest possible surface area will compliment experimentalist to grow such a surface artificially.

So far, the effects of WO_3 loading on to the different low index surfaces of t-ZrO_2 were investigated. The RDF plots suggested that the nature of the bonds play an important role in the stabilization of the surfaces. These studies have allowed us to identify the most stable surface after WO_3 addition along with the nature of the species formed. However,

it is still not very clearly understood as to why the WO_3 species chose to exist differently on different surfaces. It may be also possible that the adsorption of such species is dependent on the surface areas. Earlier experimental studies done by Sobalik *et al*. [46] reported the relationship of WO_3 nuclearity with surface areas. According to their study, the relative population of the individual WO_3 groups depended on the loading. It is controlled by the surface area of WO_3-ZrO_2 network and the particle size of parent zirconia matrix. They postulated that, generally, at comparable W^{6+} (tungsten) loading, high surface area leads to preferable stabilization of mono-atomically bound tungsten atoms on zirconia, while low surface area results in polytungstate and bulk-like WO_3 species. Thus it was concluded from their study that a monotungstate formation could be predicted for a surface having the highest surface areas. The formation of polytungstate or bulk WO_3 forms can be associated with lower surface areas.

Earlier in Chapter 7, it was noted that the addition of a polymerized WO_3 layer at 50 % coverages was not easily possible on the {110} and {111} surface of t-ZrO_2. This happened due to the larger distance between the two adjacent WO_3 groups exposed on the top surface of these slabs. Although the numbers of zirconium and oxygen atoms were kept the same for all surface slabs, it is evident that their atomistic environment varied resulting in different geometrical construction. Hence, it is worth investigating the surface areas available on the top surface for all individual pure slabs and also notices the changes occurring on these slabs after the addition of WO_3 groups.

In order to study this, the MD simulation of slabs with and without WO_3 groups was monitored using the GDIS-Software Package. [47] Table 8.1 shows the comparison of surface areas for both pure slabs at 300 K. From the values shown in Table 8.1 and Figure 8.9, it is clear that the {111} surface has the largest values of total surface areas, which is nearly double the surface area of {110} surface and almost four times the surface area of {001} surface. The total surface areas of pure t-ZrO_2 depicted the following trend, {111} > {110} > {101} > {100} > {001}.

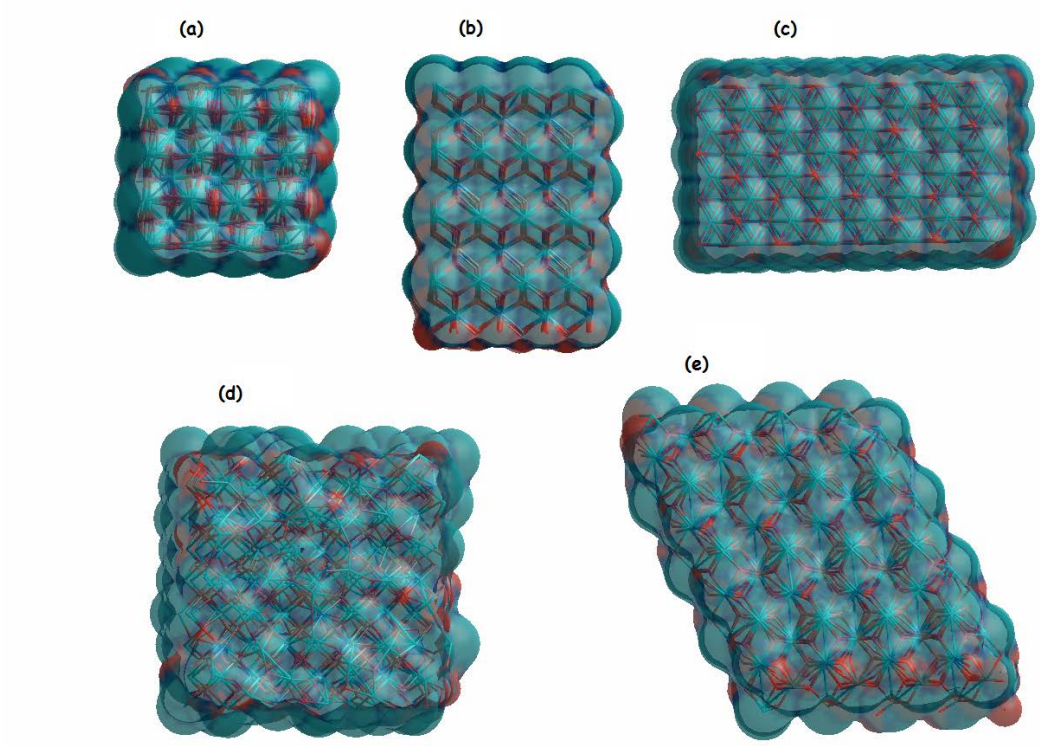

Figure 8.9 The available surface areas on the top of the slabs for all low index pure surfaces of t-ZrO_2 (a) {001} surface (b) {100} surface (c) {101} surface (d) {110} surface (e) {111} surface.

Although each slab of individual surfaces contained the same number of oxygen and zirconium atoms, the top surface of these slabs had different number of zirconia units. In the case of {111}, {110}, {101} and {100} surface the top surface consisted of 32 units of zirconia; however for {001} surface there was only 16 units of zirconia. In order to normalize the values of total surface area for the top surface of slabs, the values determined earlier were also calculated per unit of zirconia. These normalized values still indicated the largest surface areas for {111} surface which was almost double the values of surface area obtained on the {001} surface.

Although the surface area of {111} surface dominates for the pure surfaces, it is also important to note the changes in surface areas brought by the addition WO_3 groups. This will give us an indication for the relative growth of the WO_3 network. The changes brought forth by WO_3 addition is an important parameter to decide, which surface will be catalytically more active. Increase in surface areas will ease the contact of active sites with the reactants. The values shown in Table 8.2 clearly indicate that the addition of WO_3 species result in an increase in surface areas for all cases, and the magnitude of this increase is surface-specific. This is in agreement with earlier experimental work on the WO_3- ZrO_2 catalyst done by Valigi and co workers [48] who have reported the increase in surface area of t-ZrO_2 upon the addition of WO_3 groups. It was noted that for the 50 % coverages, the {001} surface undergoes the maximum increase in total surface area after WO_3 addition which was calculated to be 88

% from its pure surface values. This significant increase in surface areas for {001} surface is mainly due to the formation of dense network of WO_3 groups (see section 7.3.2 of Chapter 7). The WO_3 dense network on this surface resembled to the WO_3 bulk like structure, which were not observed on any other surfaces studies here. The reason for such formations is due the lowest values of total surface areas reported for this surface. For the {110} surface the rise in total surface area after the addition of WO_3 groups were approximately 60 %. This significant increase in total surface area is due the effect of polymerization resulting in polytungstate as well as WO_3 clusters (see section 7.3.4 of Chapter 7). For both {101} and {100} surfaces, a 46 % and 43 % rise in total surface areas were noted. For the {111} surface, however, the percentage of increase was only marginal, which was estimated to be 1.6 %. Since we hardly see any polytungstate or 3 d clusters on the {111} surface at 300 K, the total surface areas here showed only a slight increase after WO_3 addition. Although all the other surfaces had a higher percentage of increase in surface areas after WO_3 addition in comparison to {111} surface, their total values of surface areas are still lower than the surface area obtained for the {111} surface. The final total surface areas after WO_3 addition at 50 % coverages indicate the following trend {111} > {110} > {101} > {100} > {001}.

Thus it could be inferred that the increase in surface areas after WO_3 addition is mainly due to the formation of WO_3 clusters and polytungstate species, causing the growth in three dimensional patterns on the available surface. The space occupied by these species

will also add to the already existing space on the surface matrix thus maximizing the values of surface area. Similarly, for the 20 % coverages, the increase of surface areas for all surfaces except {111} indicates a percentage increase less than that on the 50 % ones. For the {111} surface, the total surface areas were 10 % higher their corresponding 50 % slabs. It could be justified that the addition of WO_3 at 20 % coverages maintained the stepped nature of this surface after the simulation resulting in a higher surface area, however, at 50 % coverages the reconstruction process results in a loss of this stepped nature (see section 7.3.5 of Chapter 7). The total surface areas after WO_3 addition at 20 % coverages indicates the following trend {111} > {110} > {100} > {101} > {001}. The only difference in this trend from the 50 % coverages is the dominance of {100} over {101} surface. For {100} surface at 20 % coverages, a polymerization between adjacent WO_3 groups resulted in the formation of dimers, however the {101} surface was not stable to polymerization (see Chapter 7). Thus a clear relationship between WO_3 nulcearity and surface areas could be drawn here.

This study gives us a clear insight, as to why WO_3 species chose to stay as monotungstate on {111} surface. Hence, we can conclude that, as we go from higher to lower values of surface areas the WO_3 nuclearity changes from monomer to dimer to trimer to polymeric spieces/ clusters and finally to bulk. Although {111} surface has the highest surface areas, catalytically the most interesting aspect would be a combination of increasing the surface areas of WO_3 network along with a high surface area zirconia matrix. The selection of such a high surface area surface also depends on the values of total surface

area per unit of zirconia and this trend for t-ZrO_2 estimated is as: {111} > {110} > {001} > {101} > {001}. Even though such a surface is selected, in practice, the possibility for the existence of such a surface will also depend on the growth rate of these surfaces. With a certain amount of WO_3 groups, the probability of WO_3 migration to a particular surface resulting in the growth of the surface might depend on various factors. How much a surface can grow in relation to the other is the next question and this could be answered by looking at the crystal morphology analysis discussed in the next section.

Table 8.1 The Calculated Surface areas of Pure Surfaces of t-ZrO_2

Surfaces	**Surface Area at 300 K (arbitrary unit)**	**Surface Area per unit of ZrO_2 at 300 K (arbitrary unit)**
{111}	1812.33	56.63
{110}	979.21	30.6
{101}	765.66	23.92
{100}	688.76	21.52
{001}	454.25	28.39

Table 8.2 The Calculated Surface areas of WO_3-ZrO_2 at both coverages

Surfaces	Surface Area for 50 % WO_3 coverages at 300 K (arbitrary unit)	Surface Area per unit of ZrO_2	% of Increase of total surface area at 300 K for 50 % WO_3 coverages	Surface areas for 20 % WO_3 coverages at 300 K (arbitrary unit)	Surface Area per unit of ZrO_2	% of Increase at 300 K of total surface area K for 20 % WO_3 coverages
{101}	1437.19	44.91	46.7	994.49	31.07	29.71
{001}	857.73	53.60	88.8	662.69	41.41	45.88
{100}	989.76	30.93	43.7	934.59	29.20	35.69
{111}	1841.55	57.54	1.6	2028.18	63.38	11.91
{110}	1571.45	49.10	60.4	1128.89	35.27	15.28

8.4 Crystal Morphology

The first theory on crystal growth was proposed in the early 1930's by W. Kossel [49] and I. N. Stranski [50], which stated that a crystal grows by two dimensional spreading of growth layers parallel to the interface. This theory served as a fundamental basis for predicting the crystal growth at an atomistic level. Once the growth process finishes, all crystals exhibit a defined morphology which depends on the individual surface energies. The crystal morphology can be determined by the Wulff's theorem as explained in Chapter 2. Wulff construction serves as a reliable tool for identifying the energetically most stable clusters in single-component systems.

The recent developments in materials science enabled the preparation of metal oxide crystals with preferentially exposed specific planes for enhancing the catalyst activity. Tian et al. [51] reported that higher catalytic activity can be obtained using Pt particles enclosed by high index planes like {730} and {210}. Recently, Shen and coworkers [52, 53] reported that Co_3O_4 nanorods with predominantly {110} planes exhibited surprisingly high catalytic activity at temperatures as low as -77° C. Well-defined m-$BiVO_4$ nanoplates with exposed {001} facets exhibit greatly enhanced activity in the visible-light photocatalytic degradation of organic contaminants and photocatalytic oxidation of water for O_2 generation. [54] Although the idea of adopting a morphology dependent catalysis makes an excellent choice for enhancing catalyst performance, the design of such a catalyst under realistic experimental conditions is a very difficult task. This

requires employing simulation techniques to understand the morphological changes under different conditions employed in a particular reaction. Earlier studies have already confirmed that the presence of sulfate groups and thermal effects play an important role in the formation of faceted shaped crystallites in sulfated zirconia. [55] The latter enhances the formation of the most stable faces, while the presence of sulfate favors the formation of small particles of the tetragonal zirconia phase. The faceted shaped crystallites contribute to the higher acidity of the catalyst promoting its activity for isomerization reactions. The present study will computationally detect the crystal morphology of pure t- ZrO_2 as well as look in detail of the changes brought by the addition of WO_3 species. The dependence of the growth process on the physical conditions such as temperature is also investigated.

8.4.1 Equilibrium Morphology of Pure t-ZrO_2

The surface energies of several low index tetragonal zirconium planes were calculated in Chapter 5 using the METADISE [56] code. Based on the energies of the relaxed surfaces, the order of surface energies depict the following trend {101} < {001} < {111} < {100} < {110} pure t-ZrO_2. A similar tendency has been reported in earlier studies done by Haase *et al*., [57] Christiansen *et al*., [58] Anez *et al*., [59] and Iskandrova *et al*. [60] The calculated surface energy values (γ) values were subsequently used to predict the equilibrium shape of the relaxed tetragonal ZrO_2 crystals. The resultant equilibrium

crystal morphology was derived using Wulff's construction. The morphology as shown in Figure 8.10 (a) indicates a truncated bipyramidal shape for pure t-ZrO_2 which has 14 faces with two big and four small square facets and eight irregular hexagons. This is also in agreement to the earlier computational study done by Christensen and Carter [58] who denoted the truncated bipyramidal morphology of t-ZrO_2 as the optimized morphology. The TEM images as shown in Figure 8.10 (d) adapted from Chraska *et al*. [62] along with the DFT studies by Sojka *et al*. [63] showed good agreement with our computed Wulff construction plot. The morphology from the TEM image [64] for t-ZrO_2 (shown on Figure 8.10 (c)) clearly indicated an irregular hexagonal pattern for {101} surface and square shaped {001} facets. This matches well with our Wulff construction plot in Figure 8.10 (a). We can easily denote here that the predominant plane is {101} on the crystal morphology. It was estimated that this plane occupies almost 96 % of the entire crystal volume. It has also the lowest energy as reported in Chapter 5 and is therefore expected to be the most stable plane and the Wulff's construction plot express this is in agreement.

Apart from this, the only two other planes expressed here are the {001} and {110} planes. The existence of {001} plane is also in agreement with the earlier reported work and is also in consistent with its surface energy values. [62] The volume occupied by the {001} plane is the around 2 %, while the {110} plane is only 1 % of the entire crystal volume. The formation of {110} plane appearing in this computed Wulff plot showed some discrepancy with the earlier work. In the TEM study there is an existence of {111} plane appearing as a green coloured triangle. These discrepancies might have been

caused by the influence of the nature of synthesis, which can act as a responsible factor to modify the energy of the facets. Apart from this single discrepancy the overall morphology seems to match quite well.

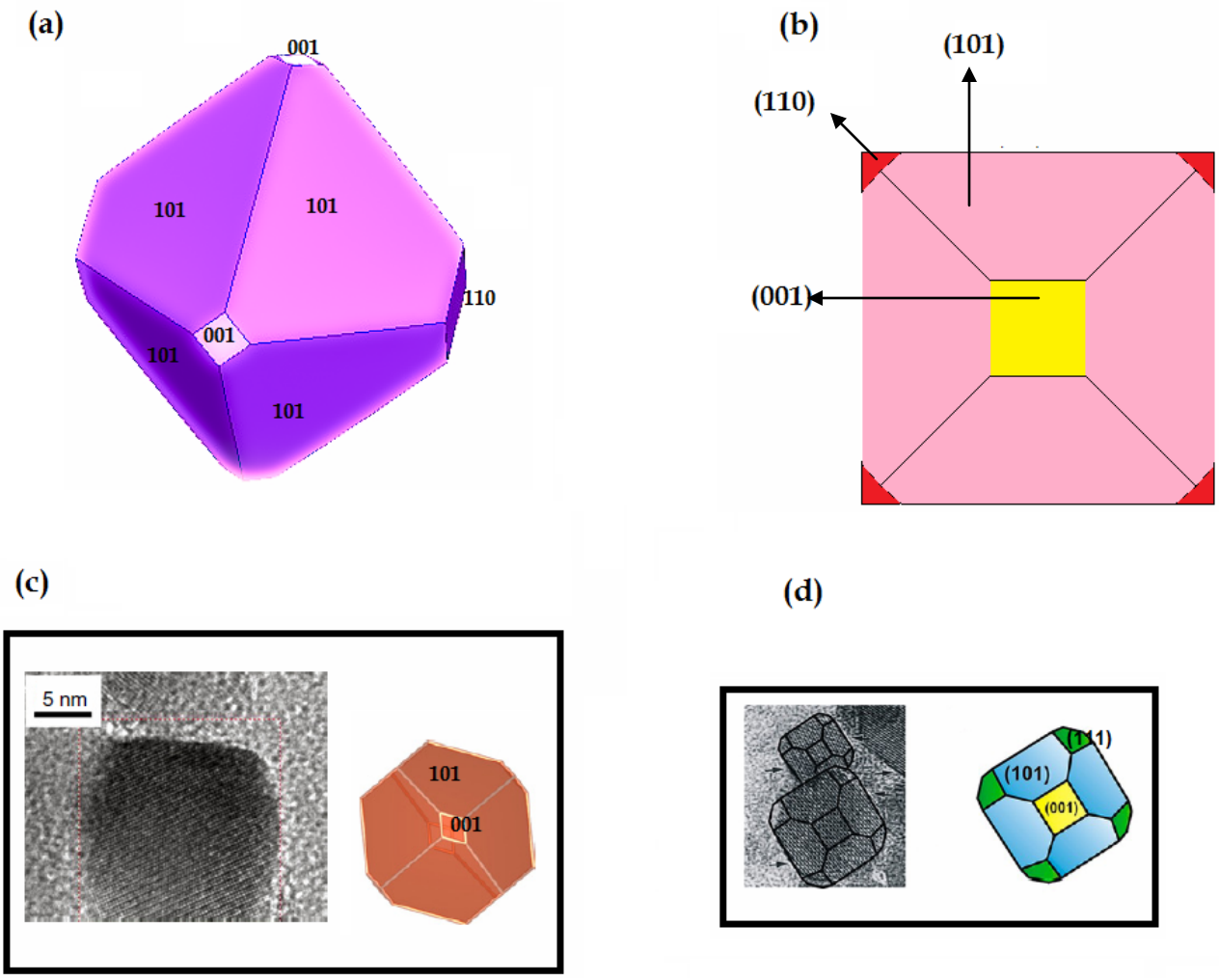

Figure 8.10 (a) Calculated crystal morphology in pure t-ZrO_2 using Wulff construction plots (a) side view (b) top plain view (c) The HRTEM image for the t-ZrO_2 along with the 'optimized' truncated tetragonal bipyramid adapted from reference [64] (d) TEM image of the morphology of t-ZrO_2 nano crystals adapted from reference [62]

8.4.2 Equilibrium Morphology of Tungstated Zirconia (WO_3-ZrO_2)

The changes brought about in the crystal morphology by the addition of WO_3 groups at 300 K to pure t-ZrO_2 are calculated. The addition at 20 % coverages resulted in the shrinking of the {101} plane where now its total share in the crystal volume accounts for only 79 %, this indicates a reduction of 17 % of the volume compared to its share in the pure phase of t-ZrO_2. This reduction in volume is expected because of the 8 % rise in the surface energy values at this coverage reported in Chapter 7. In the case of the {001} plane a 0.5 % reduction in its volume was noted at this coverage in comparison to its presence in the pure t-ZrO_2. The new plane appeared on the crystal morphology at this coverage was the {111} plane which assumed a triangular shape as shown in Figure 8.11 (a) and (b). The appearance of this plane is also in agreement to the drop on surface energy values for this surface reported in Chapter 7. It was calculated that this plane shared a volume of 25.7 % of the entire crystal morphology. The {110} plane which existed in minor amounts in pure t-ZrO_2 disappeared at this coverage.

The order of surface energies after WO_3 addition at 50 % coverages to t-ZrO_2 gives the following trend: {111} < {101} < {100} < {110} < {001} at 300 K. The Figure 8.11 (c) and (d) shows that the effect upon the addition of WO_3 species to t-ZrO_2 resulted in a significant transition from its pristine crystal morphology. The new surface facets produced here are at the expense of the abundance of {101} and {001} planes. After WO_3 addition, the hexagonally shaped {101} plane assumes a rectangle shape, while the {001} plane still continues to exist in square shape. There was a considerable shrinking

of the {101} plane, which loses its predominance over the crystal structure. This surface now occupies only 34 % of the entire crystal volume, indicating at loss of 64 % of its volume when compared to its share in the pure phase of t-ZrO_2. The {111} plane overtakes it to share its predominance in the morphology which assumes an irregular pentagon shape. This surface now almost occupies 54 % of the entire crystal volume, which has almost doubled in its volume at the 20 % coverage.

Similar to the 20 % coverages, the {110} surface also didn't appear for the 50 % ones, although a new plane {100} appeared at the 50 % coverages. The {100} plane which formed in small amounts, appeared as hexagonal shaped facets in the crystal structure. It could inferred that the {100} plane might have actually overtook the polar {110} plane. This dominance could be explained by the earlier study done in Chapter 7, where a significant drop in surface energies after the WO_3 addition was observed on {100} surface. The decrease in surface energy was almost 21 % for {100}, while for {110} it was only 3.6 %. Similarly, the WO_3 adsorption energies were also found to be more favourable for the {100} surface in comparison to {110} surface, which could be the driving force for the appearance of the {100} plane. This plane now occupies almost 9 % of the entire crystal volume.

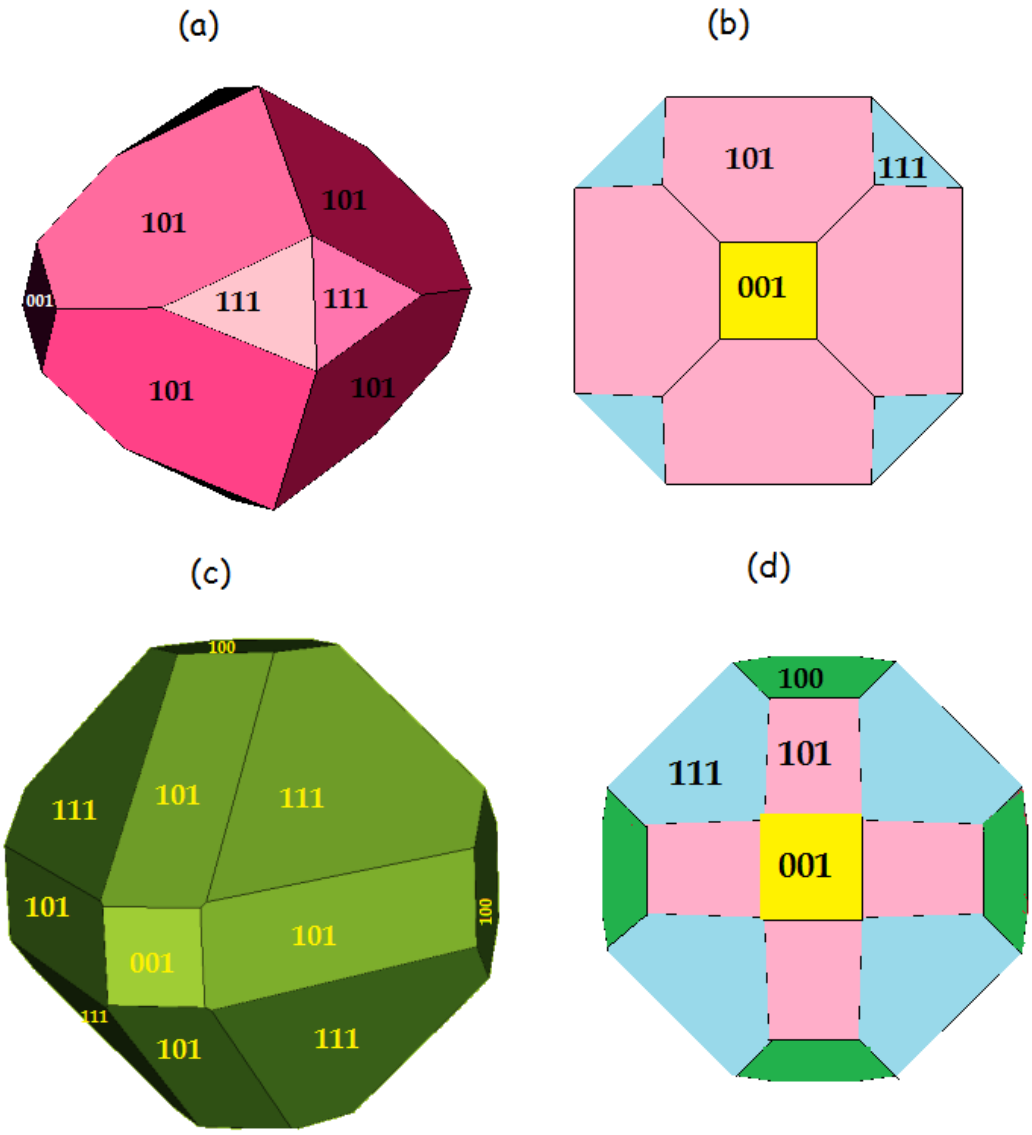

Figure 8.11 The resultant crystal morphology after the addition of WO_3 at 300 K (a) three dimensional side view for 20 % WO_3 coverage (b) top plain view for 20 % WO_3 coverage (c) three dimensional side view for 50 % WO_3 coverage (b) top plain view for 50 % WO_3 coverage.

The continued existence of {001} plane in the 50 % coverages as in pure zirconia, despite the fact that the {001) surface showed unfavorable adsorption and surface energies on WO_3 addition, indicates this surfaces higher stability. The volume of this plane in this coverage retained the same amounts as it was in pure t-ZrO_2 which was around 2 %. However, it could be concluded here that the existence of the {001} plane along with the {101} plane which contributes to a total of 36 % of the entire crystal volume will hinder the migration of WO_3 species on to these surfaces. This is because of the positive adsorption energies obtained for these surfaces indicating their less favourability to WO_3 addition as reported in Chapter 7. Thus the existence of these planes will result in lowering the activity if designed for catalytic applications. The resultant crystal morphology indicates a shrinking of the {101} plane and the contribution of the {100} and {111} planes in the overall crystal structure. Finally, it could be concluded that the addition of WO_3 species leads to dramatic changes in the equilibrium morphology of t-ZrO_2.

8.4.3 Effect of Temperature on Crystal Morphology

Since most of the catalytic reactions occur at temperatures above room temperatures, it is also important to look for any changes in the crystal morphology with the effect of increasing temperatures. In the case of pure t-ZrO_2, increase in temperatures didn't show any significant changes in the crystal morphology. However for WO_3-ZrO_2 system a significant morphological change was noted with the increase in temperatures.

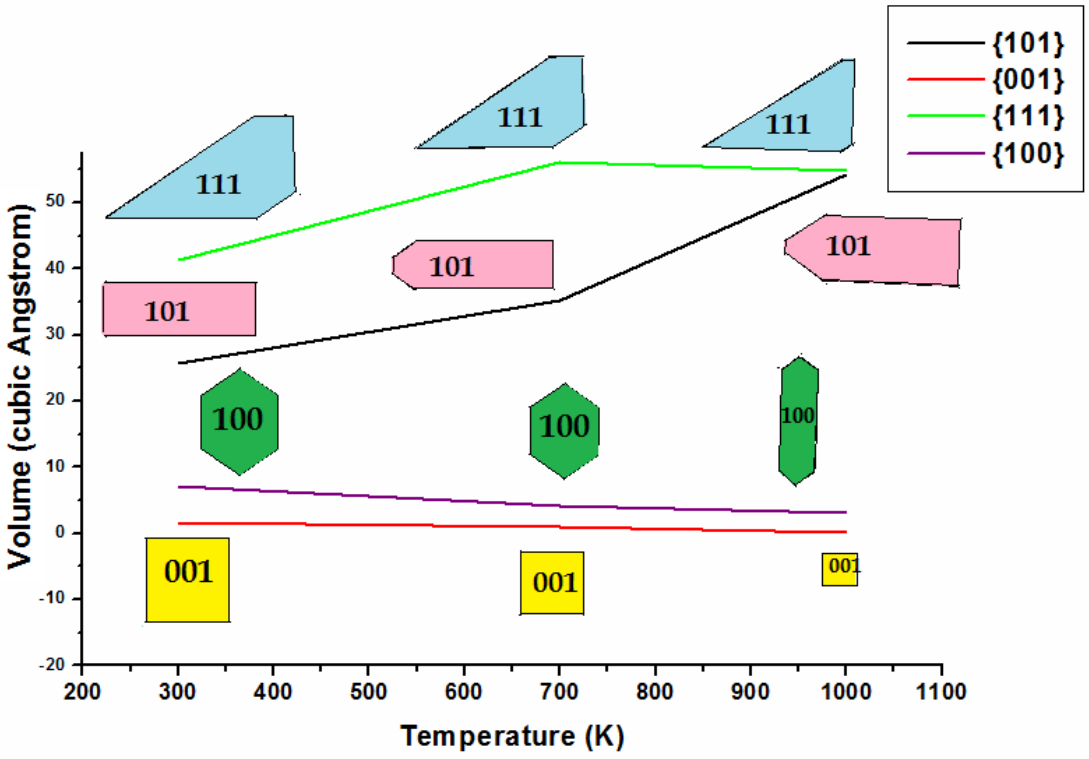

Figure 8.12 The changes in individual surface morphology in the presence of WO_3 groups at 50 % coverages with the increase in temperature.

This section looks in to the changes in crystal morphology with the increase in temperature for 50% coverages of WO_3 on t-ZrO_2. The changes on the individual surfaces were monitored by plotting their individual morphology on the change in volume to temperature graph as shown in Figure 8.12. Figure 8.13 indicates the changes occurring in the entire crystal before and after the addition of WO_3 with the effect of increase in temperature. A careful observation of the Figure 8.12 indicates that as the temperature is raised, the volume of both the predominant planes at this coverage; {101} and {111} increase following the same trend. At 1000 K both these surfaces achieve almost the same volume which accounts for 48 % of the entire crystal volume, and mutually compensates each other.

The increasing temperature transforms the shape of {101} surface from a rectangle to a convex elongated hexagon. A similar trend is also followed by the {001} and {100} plane. As temperature increases, there is a considerable decrease in {001} plane at 1000 K and this plane is almost negligible in comparison to other planes. At 1000 K both the {111} and {101} plane occupies equal predominance in the crystal morphology plane followed by with minor contribution from the {100} plane. The shrinking of the {100} plane at 1000 K has happened due to the 10 % increase in its surface energies at this temperature as reported in section 7.3.3 of Chapter 7. It could be concluded here that, the growth of the surfaces upon addition of WO_3 depends on the reaction temperature. A careful selection of temperature is needed to control the growth of catalytically favourable surfaces.

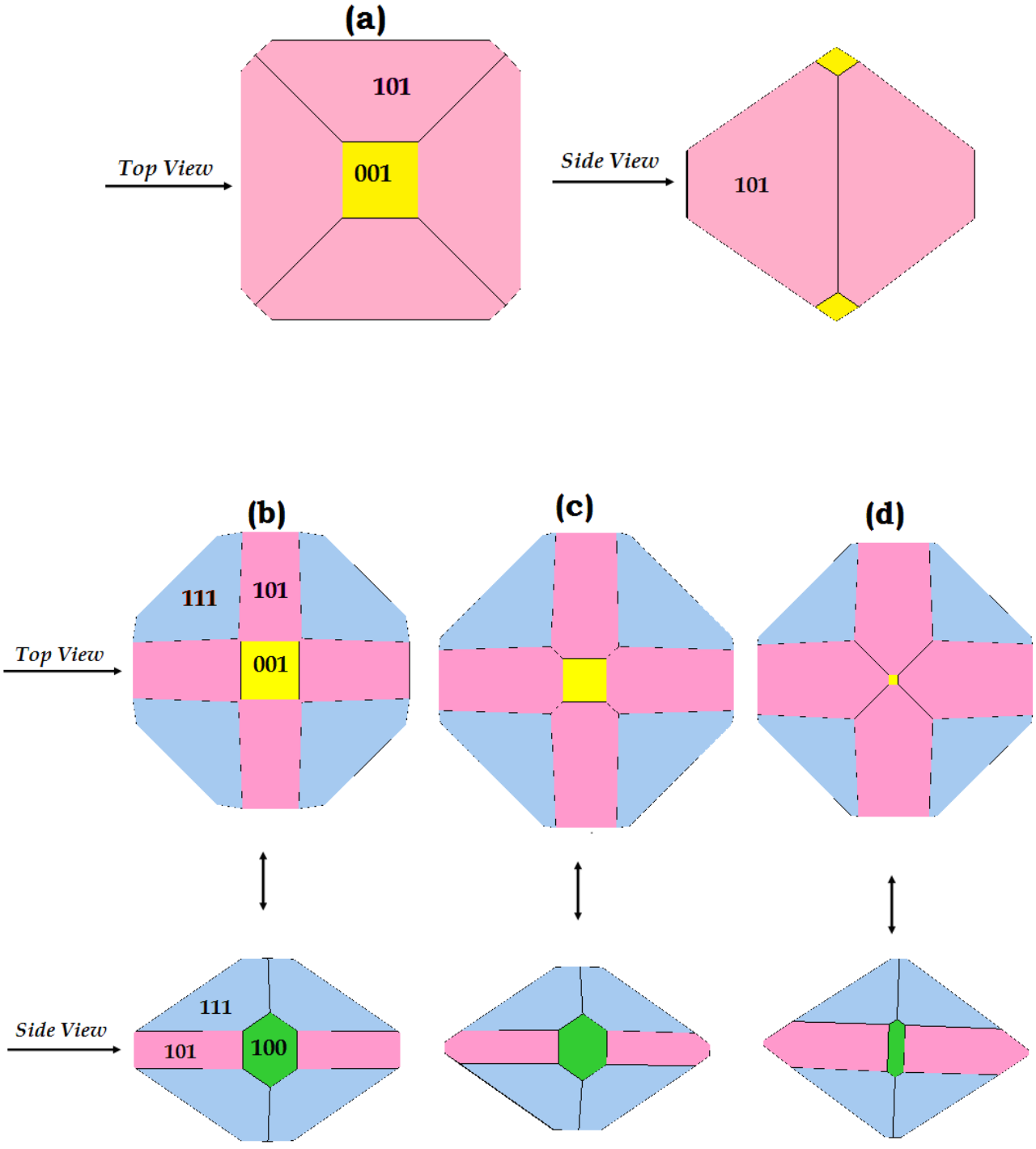

Figure 8.13 The changes in crystal morphology with addition of WO_3 groups to t-ZrO_2 with the increase in temperature (a) Pure t-ZrO_2 at 300 K (b) WO_3-ZrO_2 at 300 K (c) WO_3-ZrO_2 at 700 K (d) WO_3-ZrO_2 at 1000 K.

8.5 Conclusion

The present work helped us to detect a thermodynamically stable, high surface area catalyst with designed exposed faces. It was concluded that, the selection of right temperature and surface, along with the percentage of WO_3 coverages will determine the right ratio required for the growth of catalytically favourable surfaces. The study also emphasizes the fact that the requirement of polytungstate or cluster formation can also be fine tuned on a surface by controlling over the temperature along with the surface area of the chosen surface. The study of RDF analysis gave us an insight into the behaviour of the interactions between different atom pairs after WO_3 addition. The strength of interactions between WO_3 and zirconia matrix was the strongest on the {111} surface and the weakest on the {001} surface.

A mechanism of delocalization of electrons was proposed based on this RDF analysis. It is suggested that the most probable way for delocalization to occur on the {111} and {101} surfaces were via W-O-Zr network, while for other surfaces it was mainly through the W-O-W network. Quantitative ideas about the surface areas of parent zirconia matrix and the contribution to surface areas from the WO_3 network for each surfaces were established. This was found to depend on the type of the surface as well as the temperature. The surface area measurements predicted the quality of each surface with quantitative idea about the comparative growth of WO_3 network on the various surfaces. The study predicted that a careful selection of the high surface area matrix along with the

surface areas of WO_3 network is essential to fine tune the activity of the catalyst. The study promises to achieve a significant step forward in catalysis research by aiming to achieve precise control over the exposed faces. The computed results showed extremely good correlation with the experimental studies and were capable in providing more insight into the mechanism of WO_3 stabilized t-ZrO_2.

8.6 References

[1] J.G. Santiesteban, J.C. Vartuli, S. Han, R.D. Bastian, C.D. Chang, *J. Catal*. 168 (1997) 431.
[2] M. Scheithauer, T. K. Cheung, R. E. Jentoft, R. K. Grasselli, B.C. Gates, H. Knozinger, *J. Catal*. 180 (1998) 1.
[3] D. G. Barton, S. L. Soled, G. D. Meitzner, G. A. Fuentes, E. Iglesia, *J. Catal*. 181 (1999) 57.
[4] D. G. Barton, S. L. Soled, E. Iglesia, *Top. Catal*. 6 (1998) 87.
[5] D. G. Barton, M. Shtein, R. D. Wilson, S.L. Soled, E. Iglesia, *J. Phys. Chem. B* 103 (1999) 630.
[6] S. Kuba, P. Lukinskas, R. K. Grasselli, B. C. Gates, H. Knozinger, *J. Catal*. 216 (2003) 353.
[7] E. I. Ross-Medgaarden, W. V. Knowles, T. Kim, M. S. Wong, W. Zhou, C. J. Kiely, I. E. Wachs, *J. Catal*., 256 (2008) 108.
[8] M. Scheithauer, R.K. Grasselli, H. Knozinger, *Langmuir* ,14 (1998) 3019.
[9] C. D. Baertsch, S. L. Soled, E. Iglesia, *J. Phys. Chem. B*, 105 (2001) 1320.
[10] C. D. Baertsch, K.T. Komala, Y.H. Chua, E. Iglesia, *J. Catal*., 205 (2002) 44.
[11] J. C. Vartuli, J. G. Santiesteban, P. Traverso, N. Cardona-Martinez, C.D. Chang, S.A. Stevenson, *J. Catal*., 187 (1999) 131.
[12] D. C. Calabro, J.C. Vartuli, J.G. Santiesteban, *Top. Catal.,* 18 (2002) 231.
[13] P. Praserthdam, P. Wongmaneenil, B. Jongsomjit, *J Ind. Eng. Chem*, 16 (2010) 935.
[14] P. Wongmaneenil, B. Jongsomjit, P. Praserthdam, *Catal. Commun*. 10 (2009) 1079.
[15] M. Hino, K. Arata, *J. Chem. Soc*. *Chem. Commun*. 18 (1988) 1259.
[16] C. D. Chang, J.G. Santiesteban, D.S. Shihabi, S.A. Stevenson, U.S. Patent No. 5,401,478 (1995).
[17] C. D. Chang, J.G. Santiesteban, D.S. Shihabi, D.L. Stern, J.C. Vartuli, U.S. Patent No. 5,552,128 (1996).
[18] C. D. Chang, F.T. DiGuiseppi, S. Han, U.S. Patent No. 5,563,310 (1996).
[19] C. D. Chang, S. Han, J.G. Santiesteban, M.M. Wu, Y. Xiong, U.S. Patent No. 5,453,556 (1995).
[20] C. D. Chang, S. Han, D.J. Martenak, J.G. Santiesteban, D.E. Walsh, U.S. Patent No. 5,543,036 (1996).
[21] J. B. Moffat, Stud. *Surf. Sci. Catal.* 20 (1985) 157.
[22] M. Misono, *Catal. Rev. Sci. Eng*. 29 (1987) 269.
[23] E. Iglesia, D.G. Barton, S.L. Soled, S. Miseo, J.E. Baumgartner, W.E. Gates, G.A. Fuentes and G.D. Meitzner, *Stud. Surf. Sci. Catal*., 101 (1996) 533.
[24] D. Chandler, *Introduction to Modern Statistical Mechanics*. Oxford University Press, (1987).
[25] J. P. Hansen, I. R. McDonald, *Theory of Simple Liquids* (3rd edition), Academic Press, (2005).
[26] B. Widom, *Statistical Mechanics*: *A Concise Introduction for Chemists*, Cambridge University Press, (2002).
[27] D. A. McQuarrie, Statistical Mechanics, Harper Collins Publishers, (1976).

[28] D. Frenkel, *Understanding molecular simulation from algorithms to applications* (2nd ed. ed.). San Diego: Academic Press, (2002).
[29] P. Wochner, C. Gutt, T. Autenrieth, T. Demmer, V. Bugaev, A. D. Ortiz, A. Duri, F. Zontone, *Proc. Natl. Acad. Sci.* 106 (2009) 11511.
[30] X. Z. An, R. Y. Yang, R. P. Zou, A. B. Yu, *Powder Technol*., 188 (2008) 102.
[31] S. Kuba, P. C. Heydorn, R. K. Grasselli, B. C. Gates, M. Che, H. Knözinger, *Phys. Chem. Chem. Phys*., 3 (2001) 146.
[32] S. Wong, T. Li, S. Cheng, J. Lee, C. Mou, *Appl. Catal. A: General*, 296 (2005) 90.
[33] Z. Bao, M.-K. Song, S. C. Davis, Y. Cai, M. Liu, K. H. Sandhage, *Energy Environ. Sci.*, 4 (2011) 3980.
[34] S. Chao, M. S. Wrighton, *J. Am. Chem. Soc*., 109 (1987) 5886.
[35] T. Froeschl, U. Hoermann, P. Kubiak, G. Kucerova, M. Pfanzelt, C. K. Weiss, R. J. Behm, N. Huesing, U. Kaiser, K. Landfester, M. Wohlfahrt-Mehrens, *Chem. Soc. Rev.*, 41 (2012) 5313.
[36] M. J. Ledoux, C. Phamhuu, *Catal.Today*., 15 (1992) 263.
[37] S. K. Maity, M.S. Rana, S.K. Bej, J. Ancheyta, G.M. Dhar, T. Rao, *Appl. Catal. A: General*. 205 (2001) 215.
[38] R. G. Nuzzo, L. H. Dubois, J. Sanfillipo, *Abstracts of Papers of the American Chemical Society*. 193 (1987) 162.
[39] S. Ozkar, *Appl.Surf. Sci.* ,256 (2009) 1272.
[40] M. Ozawa, M. Kimura, *J. Mater. Sci. Lett.*, 9 (1990) 446.
[41] R. Srinivasan, D. Taulbee, B.H. Davis, *Catal. Lett.*, 9 (1991) 1.
[42] C.J. Norman, P.A. Goulding and I. McAlpine, *Catal, Today*, 20 (1994) 313.
[43] B. Fegley, Jr., P. White and H.K, Bowen, *Am. Ceram. Soc. Bull*., 64 (1985) I 115.
[44] P. D. L. Mercera, J. G. Van Ommen, E. B. M. Doesburg, A. J. Burggraaf, J. R. H. Ross, *Appl. Catal.*, 71 (1991) 363.
[45] G. Chuah, S. Jaenicke, S. Cheong, K. Chan, *Appl. Catal. A: Gen*. 145 (1996) 267.
[46] D. Kaucký, B. Wichterlová, J. Dedecek, Z. Sobalik, I. Jakubec, *Appl.Catal. A*: *Gen*., 397 (2011) 82.
[47] S. Fleming, A. Rohl, *Z.Kristallogr*, 220 (2005) 580.
[48] M. Occhiuzzi, D. Cordischi, S. De Rossi, G. Ferraris, D. Gazzoli, M. Valigi, *Appl. Catal. A:Gen.* 351 (2008) 29.
[49] W. Kossel Nachr Ges Wiss Gottingen, Math- Physik Klasse, *Band*, 135 (1927)
[50] I. Stranski, *Z.Phys.Chem*., 136 (1928) 259
[51] N. Tian, Z. Y. Zhou, S. G. Sun, Y. Ding, Z. L. Wang, *Science*, 316 (2007), 732.
[52] X. W. Xie, Y. Li, Z. Q. Liu, M. Haruta, W. J. Shen, *Nature*, 458 (2009) 746.
[53] X. W. Xie, W. J. Shen, *Nanoscale*, 1 (2009) 50.
[54] D. Yang, L. M. Qi, J. M. Ma, *Adv. Mater*., 14 (2002) 1543
[55] M. Benäıssa, J. G. Santiesteban, G. D´ıaz, C. D. Chang, M. Jos ´e-Yacaman, *J. Catal*,. 161 (1996) 694.
[56]G.W. Watson, E.T. Kelsey, N.H. De Leeuw, D.J. Harris, S.C. Parker, *J.Chem.Soc*. 1996, *92*, 433.
[57] F. Hasse, J. Sauer, *J. Am. Chem. Soc*., 120 (1998) 13503.
[58] A. Christensen, E. Carter, *Phys. Rev. B*, 58 (1998) 12.
[59] R. Anez, A. Sierraalta, G. Mortorell, P. Sautet, *Surf. Sci*., 603 (2009) 2526.

[60] I. M. Iksandrova, A. A. Knizhnik, E. A. Rykova, A. A.; Bagatur'yants, B. V. Potapkin, *Microelectron. Eng*., 69 (2003) 587.
[61] Internet site : http://www.cortona3d.com/Products/Viewer/Cortona-3D-Viewer.aspx
[62] T. Chraska, A. H. King, C. C. Berndt, *Mater. Sci. Eng*., A, 286 (2000) 169.

[63] W. Piskorz, J. Grybos, F. Zasada, P. Zapała, S. Cristol, J. Paul, Z. Sojka, *J. Phys. Chem. C*, 116 (2012) 19307.
[64] A. S. Barnard, R. R. Yeredla, H. Xu, *Nanotechnology*, 17 (2006) 3039.

Chapter 9 Summary and Conclusions

"The water in a vessel is sparkling; the water in the sea is dark. The small truth has words which are clear; the great truth has great silence".

— Rabindranath Tagore

The computational work in this thesis has investigated the technologically important catalytic material tungstated zirconia (WO_3-ZrO_2) system. Since the existing theories did not provide a clear idea of the mechanism of its catalytic activity and raised further questions, this thesis attempted to propose some useful insights. The method here utilised an interatomic potential approach to model bulk, surfaces and defect structures using both static energy minimisation techniques as well as molecular dynamics approach. The results were compared with available experimental data, and the agreements between them were found to be reasonable at every stage of evaluation.

Chapter 4 began with the validation of the pure tetragonal zirconia (t-ZrO_2) and its lattice parameters were compared with cubic zirconia. The two phases were compared to find out the variation of dz parameter in order to accurately predict the structure of t-ZrO_2. The potential models were directly used from the previous studies done on t-ZrO_2. Since tetragonal form of zirconia is a high temperature polymorph, adjustments in the lattice parameters within the unit cell dimensions were performed using constant pressure minimisation using the molecular dynamics program i.e. DL_POLY 2.14 Package. The

equilibrated values of lattice parameters were calculated from the MD run between the temperature range of 300 K and 2000 K, where the tetragonal phase was properly maintained. It was also concluded that, although the temperatures were increased; the dz parameter still remained at a constant value. This indicated the stability of the computed tetragonal structure. The analysis of the final optimized structure indicated good agreements with the earlier experimental and computational works. The phonon properties of t-ZrO_2 were also predicted using the lattice dynamic calculations incorporated in the GULP code. The phonon modes showed six important Raman active modes. Good agreements were noted when their values were compared with the previous computational and experimental studies. The phonon study concluded that majority of the DOS was dominated by the lighter oxygen atoms and zirconium atoms tended to bunch around the lower energy end. The measurements of thermodynamic properties of t-ZrO_2 were almost in alignment with the experimental results, where the Debye temperature computed by this study was also close to experimentally reported value.

Once the successful validation of the pure system was achieved, different types of surfaces were studied, which formed the basis of Chapter 5. Oxygen and zirconium terminated surfaces revealed the stability for oxygen terminated ones, and hence all further studies were carried out on the surfaces with oxygen terminations. Chapter 5 computed the surface energies of five most important surfaces of t-ZrO_2 at 300 K, i.e {101}, {001}, {100}, {110} and {111} surfaces. The analysis of surface energies by both static and molecular dynamic methods concluded that the {101} surface was the

most stable surface of t-ZrO_2. This was in agreement with the earlier works done by Grimes and co-workers. Finally, the trend for the stability of pure surfaces was predicted to be in the following order: {101} > {001} > {111} > {110} > {100}. Since the stability for bulk and different surfaces of t-ZrO_2 were established in Chapter 5, the next chapter proceeded with the effects of point defects within the bulk and surfaces of t-ZrO_2. The point defects on bulk t-ZrO_2 indicated the possibility for existence of an anion vacancy compared to a cation vacancy. It was also inferred that the decreasing size of cation dopants always favoured the substitutional defect energies. Among all the cations (Ca^{2+}, Y^{3+}, Ce^{4+}, Nb^{5+}, W^{6+}) studied tungsten (W^{6+}) was found to be the most preferred cation for substitution in bulk t-ZrO_2, due to the lower values of substitutional energies obtained with it. The Schottky and Frenkel mechanism in bulk t-ZrO_2 structure indicated a preference for a Schottky defect in bulk; however on surfaces of t-ZrO_2 the anion frenkel mechanisms were found to be more stable.

The study of oxygen mobility on the surfaces of t-ZrO_2 was to understand the catalytic applications. This was determined using the CHAOS program. The oxygen mobility in the presence of various dopants indicated that tungsten (W^{6+}) lowered the activation energy barrier much more than any other cation studied here. The results obtained with tungsten motivated us to look further in to the adsorption energy profiles of this cation on bulk and surfaces of t-ZrO_2. Different mechanisms of introducing WO_3 in to the bulk of t-ZrO_2 were discussed, of which three types of mechanisms were proposed here, Type I, Type II and Type III.

Each of them introduced tungsten (W^{6+}) cations by substituting the zirconium atoms in such a way that there was a charge balance in all three cases. This was achieved by either adding an interstitial or creating a vacancy or by creating substitutional defects. It was inferred that the type of defect Type I-NN which created oxygen vacancies to balance the charge for substituting zirconium with tungsten was the most favourable mechanism to dominate in the bulk. Earlier experimental studies support this ideology, where creation of oxygen vacancies were observed with dopant additions in t-ZrO_2. To check the relative preference of this defect on surfaces, the same defect Type I-NN was also placed on the surfaces of t-ZrO_2. The highest segregation energies for Type I-NN defect were found to occur on the {111} surface and the trend for segregation energies were as follows: {111} > {110} > {100} > {001} > {101}. The segregation energies obtained on all surfaces were negative, implying that the addition of WO_3 will result in its segregation to the surfaces. This fact was further strengthened by monitoring the segregation energies as we moved a single tungsten atom away from the surface in increasing depth on the {111} surface.

The negative values of segregation energies obtained on surfaces of t-ZrO_2 predicted their migration to the surfaces rather than staying within the bulk. However, the estimation of solution energies clearly indicated which surfaces were more capable of having this substitution. The computed values of solution energies indicate that the addition of WO_3 on the surfaces would turn out to be favourable only for the {110} and {111} surface, where an exothermic reaction is predicted. For all the other surfaces the positive values

of solution energies obtained indicated their instability to WO_3 substitution. Having established that WO_3 prefers to stay at the surface rather than the bulk of t-ZrO_2, the central idea of this thesis was evaluated in Chapter 7. The presence of various types of surface species existing on tungstated zirconia (WO_3-ZrO_2) was the primary goal of this thesis and hence efforts to check the effects of the WO_3 adsorption on the stabilization of t-ZrO_2 surfaces have been made. These results will also enable us to make a better comparison with the experimental observations done by Christopher Kiely (2009), and check if the presence of dimers, polytungstate or Zr- WO_3 species were formed on any surfaces studied here. To achieve this; molecular dynamic (DL_POLY 2.14 package) calculations were performed. The slabs of t-ZrO_2 were prepared with WO_3 loadings at two different coverages to check if the higher or lower coverages influenced the type of species formed on any surface. The study concluded that the effect of WO_3 addition played an important role in the stabilisation of t-ZrO_2 surfaces. The WO_3 groups resulted in stabilising the surfaces which were otherwise unstable in pure t-ZrO_2 and an opposite effect was noted for the previously stable surfaces. At low coverages of WO_3, the surface {101} still retained its higher stability compared to all the other surfaces. An 8 % increase in surface energies were noted for the {101} surface at lower coverages, however, this energy value was still lower in comparison to all the other surfaces. Thus despite being unfavourable to WO_3 addition, at lower coverages of WO_3 addition, the surface {101} was still the most stable surface in t-ZrO_2.

At higher coverages of WO_3, the instability of {101} surface to WO_3 addition was clearly indicated by a rise in 26 % of its initial surface energies. Under the same conditions, it

was also noted that the {111} surface indicated a decrease in surface energies by 22 % and this surface became the most stable among all the other surfaces after WO_3 addition. The nature of the species after the simulation revealed the formation of monomers, dimers, polytungstates, Zr-WO_3 as well as WO_3-bulk like species but their relative occurance depended on the type of the surface.

Although Chapter 7 provided some idea to the nature of WO_3 addition on the various surfaces of t-ZrO_2; it also became important to elucidate the nature of interactions between the surface species to provide some understanding to their catalytic behaviour. Chapter 7 saw that the nature of the WO_3 species were surface specific. The appearance of the monotungstate species on the {111}, while polytungstate on {101} and WO_3 bulk like species on {001} surface, raised questions about the factors that influenced the WO_3 nuclearity. This formed the general discussion for Chapter 8, where the evaluation of the strength of interaction between atoms were monitored using RDF analysis and the studies determining the nature of WO_3 nuclearity were performed using the surface area studies. The RDF analysis showed the highest strength of interaction between surface species (Zr, O) occurred on the {101} surface in pure t-ZrO_2. However, after WO_3 addition at both coverages, the highest strength of interaction for surface species (W, O, Zr) were found to occur on the {111} surface. The interaction within the bulk atoms after WO_3 addition was almost the same for all surfaces.

Depending on the nature of these interactions, a mechanism for delocalization of electrons was proposed on these surfaces. The surface {101} and {111} were concluded

to have the delocalization occurring mainly *via* –W-O-Zr-O-W- network, while for other surfaces it was mainly proposed to occur *via* -W-O-W- network at 300 K. However, since the {101} surface is not favourable to WO_3 addition at 300 K it could be thought the such an effect of delocalization will not occur on this surface and will be mainly confined to the {111}, {100} and {110} surface.

The reason behind the variation of WO_3 nuclearity was confirmed with the surface area studies. It was concluded that having a high surface area will lead to the formation of monotungstate species, while decreasing surface areas will favour polymeric to bulk type species. Towards the end of this thesis, the variation occurring in the crystal morphology from pure t-ZrO_2 to WO_3 added zirconia was monitored using the Wulff's construction plots. The appearances of the planes in the crystal morphology were in agreement with their corresponding values of surface energies. The morphology study predicted a truncated bipyramidal shape for pure t-ZrO_2. In the case of pure t-ZrO_2 at 300 K, the {101} plane dominated the crystal morphology, which still continued to dominate at lower coverages of WO_3 addition. At higher coverages, the {111} surface dominated the entire crystal morphology and appearance of the {100} plane was also noticed at 300 K. The effect of increase in temperature at higher coverages of WO_3 indicated shrinking of {001} and {100} planes. The majority of the crystal morphology at higher temperatures were dominated by the {101} and {111} surface. Although the {110} surface indicated stabilisation upon addition of WO_3 groups, this surface didn't show up in the crystal morphology.

Future work needs to look at the effect of defects on crystal morphology. It could be possible that the presence of defects like oxygen vacancies might also have role to play in the surface stabilisation. It would be also worthwhile to develop an understanding of the adsorption behaviour of OH radicals in the presence of WO_3 groups on t-ZrO_2 surfaces, which would be of considerable interest to achieve a wider catalytic importance. Finally, this work has established the importance of using computer modelling techniques to probe the effect of the adsorption of WO_3 on t-ZrO_2. A future to design a highly active WO_3-ZrO_2 catalyst could be achieved by artificially growing catalytically favourable surfaces. This study provided more insight in to the processes occurring at the atomic level, which will serve as a fundamental knowledge to help and guide the experimental work.